



Durham E-Theses

Electron traps in rutile

Duckworth, C. N.

How to cite:

Duckworth, C. N. (1986) *Electron traps in rutile*, Durham theses, Durham University. Available at Durham E-Theses Online: <http://etheses.dur.ac.uk/6894/>

Use policy

The full-text may be used and/or reproduced, and given to third parties in any format or medium, without prior permission or charge, for personal research or study, educational, or not-for-profit purposes provided that:

- a full bibliographic reference is made to the original source
- a [link](#) is made to the metadata record in Durham E-Theses
- the full-text is not changed in any way

The full-text must not be sold in any format or medium without the formal permission of the copyright holders.

Please consult the [full Durham E-Theses policy](#) for further details.

The copyright of this thesis rests with the author.
No quotation from it should be published without
his prior written consent and information derived
from it should be acknowledged.

ELECTRON TRAPS IN RUTILE

by

C.N. DUCKWORTH, MA (Cantab)

Thesis submitted to the University of Durham

for the degree of

Master of Science

September 1986



19. JUN. 1987

ABSTRACT

Undoped samples of single crystal rutile and rutile powder have been studied by the methods of photoluminescence, thermoluminescence and thermally stimulated conductivity. Crystal samples doped with chromium, iron, manganese, cobalt and nickel and powder samples doped with chromium and iron were also studied. Additionally capacitance-voltage, current-voltage and deep level transient spectroscopy measurements were made on Schottky diodes fabricated on rutile made semiconducting by reduction and niobium doping.

Undoped, chromium and nickel doped samples all showed one form of PL temperature dependence in which the luminescence was quenched above 190 K. Iron, cobalt and manganese doped samples showed a different dependence in which the intensity decreased from 80 K. The chromium doped powders showed an increase in photoluminescence intensity with chromium doping which supports the view of several workers that chromium provides the luminescence centre in rutile.

Evidence was found in thermoluminescence spectra for nine different trapping levels. Thermoluminescence measurements on powders indicated that the spectra were composed of the same peaks found in the crystal samples, although they were not distinct.

DLTS spectra from a niobium doped rutile crystal showed one dominant maximum. The variation of this maximum with the DLTS rate window gave an activation energy and a capture cross-section in excellent agreement with the values for the dominant TSL peak and suggests that the simple insulator model used for TSL analysis applies well to rutile. The DLTS result allows the results for trap depths derived from TSL measurements to be viewed with some confidence.

ACKNOWLEDGEMENTS

I would like to thank Professor G.G. Roberts for allowing me to use the facilities of the Department of Applied Physics and Electronics and Tioxide International, Stockton on Tees for financial support.

I am especially grateful to my supervisor, Dr. J. Woods, for his assistance and encouragement throughout my time in Durham and during the writing of this thesis. I would also like to thank Dr. A.W. Brinkman for his many helpful comments. Mr. F. Spence, Mr. W. Mounsey, Mr. T. Hargreaves and Mr. N. Thompson all deserve a mention for their technical assistance during the course of this work.

I would like to acknowledge the invaluable assistance of Dr. T. Egerton and other technical staff at the Central Laboratories of Tioxide International.

My thanks go to my colleagues, both at Durham and since, for their encouragement and finally to my wife, Julia, for her patience and understanding during the writing of this thesis and for help with the diagrams.

ELECTRON TRAPS IN RUTILE

C.N. DUCKWORTH

Declaration

No part of this thesis has previously been submitted by me for a degree in Durham or any other university. Except where reference has been made in the text to the work of others, the thesis is my own independent work.

To my parents

CONTENTS

CHAPTER 1	INTRODUCTION	1
1.1	Titanium dioxide pigments	2
1.2	Paint films	3
1.3	Outline of thesis	4
CHAPTER 2	PROPERTIES OF RUTILE	6
2.1	Introduction	7
2.2	Crystallography	7
2.3	Non-stoichiometry in rutile	10
2.4	Band structure of rutile	11
2.5	Carrier mobility in rutile	11
CHAPTER 3	THEORY	16
3.1	Introduction	17
3.2	Thermal equilibrium and steady-state phenomena	18
3.3	Thermally stimulated luminescence and conductivity	19
3.4	Metal-semiconductor contacts	29
3.5	Deep level transient spectroscopy	32
CHAPTER 4	EXPERIMENTAL TECHNIQUES	38
4.1	Sample preparation	39
4.2	Doping	40
4.3	Contacts and mounting	41
4.4	Liquid nitrogen cryostat	42
4.5	Optical apparatus	44
4.6	Photoluminescence measurements	44
4.7	Thermoluminescence measurements	46
4.8	Thermally stimulated conductivity measurements	46
4.9	Deep level transient spectroscopy	48

CHAPTER 5	UNDOPED RUTILE	50
5.1	Introduction	51
5.2	Material preparation	51
5.3	Photoluminescence	51
5.4	Thermally stimulated luminescence and conductivity	59
5.5	Reduced rutile	71
5.6	Summary	78
CHAPTER 6	CHROMIUM DOPED CRYSTALS	80
6.1	Introduction	81
6.2	Material preparation	81
6.3	Photoluminescence	81
6.4	Thermally stimulated luminescence and conductivity	82
6.5	Summary	99
CHAPTER 7	IRON DOPED CRYSTALS	100
7.1	Introduction	101
7.2	Material preparation	101
7.3	Photoluminescence	101
7.4	Thermally stimulated luminescence and conductivity	104
7.5	Summary	109
CHAPTER 8	MANGANESE DOPED CRYSTALS	111
8.1	Introduction	112
8.2	Photoluminescence	112
8.3	Thermally stimulated luminescence and conductivity	112
8.4	Summary	115
CHAPTER 9	COBALT DOPED CRYSTALS	116
9.1	Introduction	117
9.2	Photoluminescence	117
9.3	Thermally stimulated luminescence and conductivity	117
9.4	Summary	120

CHAPTER 10	NICKEL DOPED CRYSTALS	121
10.1	Introduction	122
10.2	Photoluminescence	122
10.3	Thermally stimulated luminescence and conductivity	122
10.4	Summary	125
CHAPTER 11	NIOBIUM DOPED CRYSTALS	126
11.1	Introduction	127
11.2	Material preparation	127
11.3	Capacitance-voltage measurements	128
11.4	Current-voltage measurements	128
11.5	Deep level transient spectroscopy	131
11.6	Summary	134
CHAPTER 12	POWDERS	136
12.1	Introduction	137
12.2	Material preparation	137
12.3	Photoluminescence	137
12.4	Thermoluminescence	145
12.5	Thermally stimulated conductivity	152
12.6	Summary	152
CHAPTER 13	CONCLUSIONS	163
13.1	Summary	164
13.2	Conclusions	169
REFERENCES		170

CHAPTER 1

INTRODUCTION

- 1.1 Titanium dioxide pigments
- 1.2 Paint films
- 1.3 Outline of thesis



1.1 TITANIUM DIOXIDE PIGMENTS

Rutile, a form of titanium dioxide, is the principal mineral of titanium. Titanium dioxide is the most widely used white pigment, principally in paint, paper, plastic and rubber applications. Thin layer TiO_2 electrodes, or aqueous suspensions, may be used in cells for the photolysis of water [1] and rutile ceramics have been used to make containers for spent nuclear fuels [2]. The predominance of titanium dioxide is due to its high refractive index, lack of colour and chemical inertness [3]. The high refractive index in the visible portion of the spectrum results in strong scattering of visible radiation by particles in the correct size range. This provides the opportunity to produce films with high opacity. Among those substances that are available in quantities sufficient to meet the requirements of industry, no other material has the high refractive index and other desirable pigmentary properties of titanium dioxide [4].

The manufacture of titanium dioxide pigments results in the production of either the anatase or rutile crystal structure. Rutile pigments have greater hiding power and improved durability in paints but are more expensive to produce and are slightly inferior in colour.

Titanium dioxide pigments can be made in two ways. The original basic process involved digesting the ore with sulphuric acid as completely as possible. This method is known as the sulphate process and exploits the mineral ilmenite, which is abundant. However, the waste dilute sulphuric acid and iron sulphates produced make this process environmentally pollution sensitive. The alternative, known as the chloride process, was developed by Dupont in the USA and exploits the mineral rutile. The refined ore is made to react with chlorine to form liquid titanium tetrachloride which, after distillation, is oxidised under carefully controlled conditions to produce titanium dioxide. This method produces only small quantities of waste product as the chlorine can be recycled.

The two processes represent alternative means of extracting essentially pure

titanium dioxide from titanium bearing ores and at the same time providing a base pigment within a very closely defined particle size range. This base pigment is normally processed further to provide products tailored to their end use.

A number of important properties are given to the pigment by this additional processing. For example, the individual particles may be coated by selective precipitation of small quantities of colourless, inert oxides such as silicon dioxide, aluminium oxide or titanium dioxide.

Titanium dioxide pigments are marketed according to certain physical characteristics such as hiding power, colour and stability, which confirms durability on a paint film. These characteristics can be affected by the presence of trace quantities of metallic oxides, as well as by particle size.

1.2 PAINT FILMS

A paint is made by mixing a pigment in a binder and special surface treatments are always necessary to make the pigment sufficiently durable for use in coatings [5,6]. The durability of a paint film will be influenced by the conditions under which the paint is applied, by the degradation of the binder and by the effects of the pigment on the binder. The use of silicone modified alkyds and polyesters, vinyl co-polymers and acrylic systems as binders has produced a remarkable increase in durability but, because of their high stability, the weak photocatalytic effect of the pigment has become a major factor in determining the durability of a paint film. The photo-degradation of commercial polymers by titanium dioxide is believed to be related to the formation of an oxygen radical by electron transfer from excited state TiO_2 to molecular oxygen [7]. The oxygen radical may then react with water to form reactive hydroxyl and perhydroxyl radicals which, in turn, may react with the binder and initiate degradation of the paint film [7]. In addition to initiating the photo-degradation, the pigment can also protect the film by absorbing ultra-violet light to such an extent that there is little radiation left to damage the binder directly.

Kaempf, Papenroth and Holm [8] have developed a model to describe the degradation processes involved in weathering. When a titanium dioxide pigmented paint film is exposed to ultra-violet light, degradation starts uniformly over the whole surface. The photo-activated process, however, only occurs where incident radiation strikes a titanium dioxide surface, particularly on the surface facing the radiation. The binder behind the pigment particle is effectively screened from the ultra-violet light by the absorption of the titanium dioxide. Eventually, the binder above and around the sides of the pigment particle is removed leaving the particle standing on a stalk of binder.

Clearly, the reaction caused by the excitation of the titanium dioxide can be modified by altering the recombination kinetics of the excited electrons and the reaction may be retarded by the presence of a strong electron acceptor. Torluachi et al [9] have suggested that transition metals such as chromium and iron may be suitable but these can give rise to discolouration. An understanding of the electronic properties of transition metal dopants in rutile is, therefore, of great value in improving the durability of paint films.

1.3 OUTLINE OF THESIS

The present research has been undertaken with the aid of financial and technical support from the Central Laboratories of Tioxide International Ltd., Stockton on Tees. It follows and expands on certain aspects of a previous thesis by R.W.A Hillhouse [10] which outlined work on the growth and characterisation of single crystal rutile. Some of the techniques employed by Hillhouse have been adopted in the present work; these include photoluminescence, thermoluminescence and thermally stimulated conductivity. Other techniques, such as deep level transient spectroscopy, have also been applied successfully to rutile. The study includes work on semiconducting rutile and doped powders as well as undoped and doped single crystals.

Chapters 2 and 3 give, respectively, reviews of the properties of rutile and the theory behind the experimental techniques employed. Chapter 4 gives a description of the experimental methods and instrumentation used in making the measurements. Undoped crystals and crystals doped with chromium, iron, manganese, cobalt, nickel and niobium were studied. The results obtained for these crystals are presented in the form of a separate chapter for each dopant. Chapter twelve discusses results from powders. The powders studied were undoped and doped with chromium or iron. Each results chapter contains a summary of the results in that chapter, while the final chapter gives a concluding discussion and summary.

CHAPTER 2**PROPERTIES OF RUTILE**

- 2.1 Introduction**
- 2.2 Crystallography**
- 2.3 Non-stoichiometry in rutile**
- 2.4 Band structure of rutile**
- 2.5 Carrier mobility in rutile**

2.1 INTRODUCTION

Rutile is the principal mineral of titanium, the second most abundant transition metal, and has been studied extensively by many workers. TiO_2 has a large band gap coupled with a very high value of the static dielectric constant. It has wide scientific and industrial applications as a pigment and in the photolysis of water.

2.2 CRYSTALLOGRAPHY

Titanium dioxide exists in three polymorphic forms; rutile, anatase and brookite. Rutile forms the last of a series of oxides of titanium with the composition $\text{Ti}_n\text{O}_{2n-1}$ (TiO , Ti_2O_3 , Ti_3O_5 , ...) and TiO_2 . Phases of $\text{Ti}_n\text{O}_{2n-1}$ with values of n up to 38 ($\text{TiO}_{1.974}$) have been reported [11]. These higher oxides of titanium may be considered to be made up from TiO_6 octahedra which share corners, edges or faces in different ways, depending on the oxide composition. The rutile form of TiO_2 is a tetragonal crystal of space group $4/mmm$ with unit cell dimensions, at 250°C , of 0.2959 nm and 0.4594 nm along the c and a directions, respectively. A projection of the unit cell for rutile perpendicular to the c -axis is shown in figure 2.2.1. It contains two non-equivalent Ti^{4+} ions, each of which is surrounded by a slightly distorted oxygen octahedron. The two non-equivalent titanium ions differ only in that the surrounding oxygen octahedra are rotated by 90° about the c -axis. This is illustrated in figure 2.2.2. This arrangement of TiO_6 octahedra allows open channels to exist along the c -axis and this explains some of the large anisotropies observed, such as the diffusion of lithium [12]. These channels may be considered as stacks of oxygen octahedra with no central titanium ion and are possible sites for interstitial impurity ions. There are four of these sites in the unit cell at locations $0\frac{1}{2}0$, $\frac{1}{2}00$, $0\frac{1}{2}\frac{1}{2}$ and $\frac{1}{2}0\frac{1}{2}$. Huntingdon and Sullivan [13] have suggested the possibility of a second class of interstitial site on $\frac{1}{2}0\frac{1}{4}$ positions which are surrounded by four oxygen atoms.

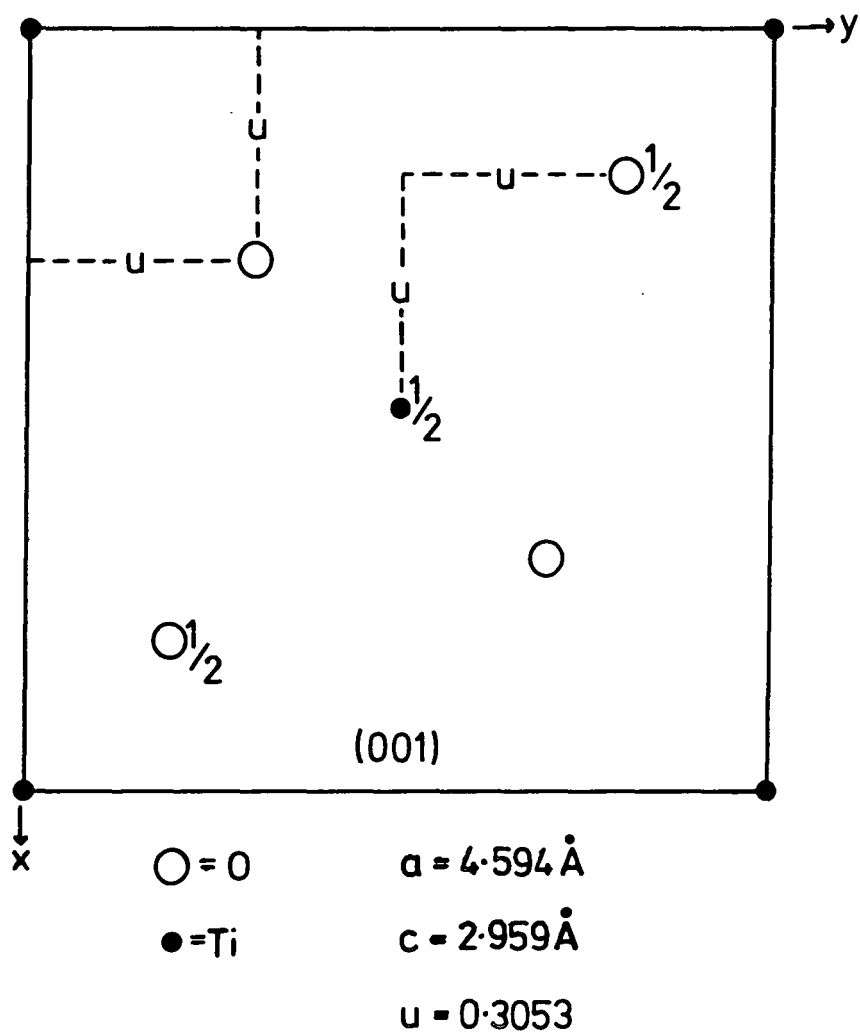


Figure 2.2.1 A projection of the rutile unit cell onto the (100) plane

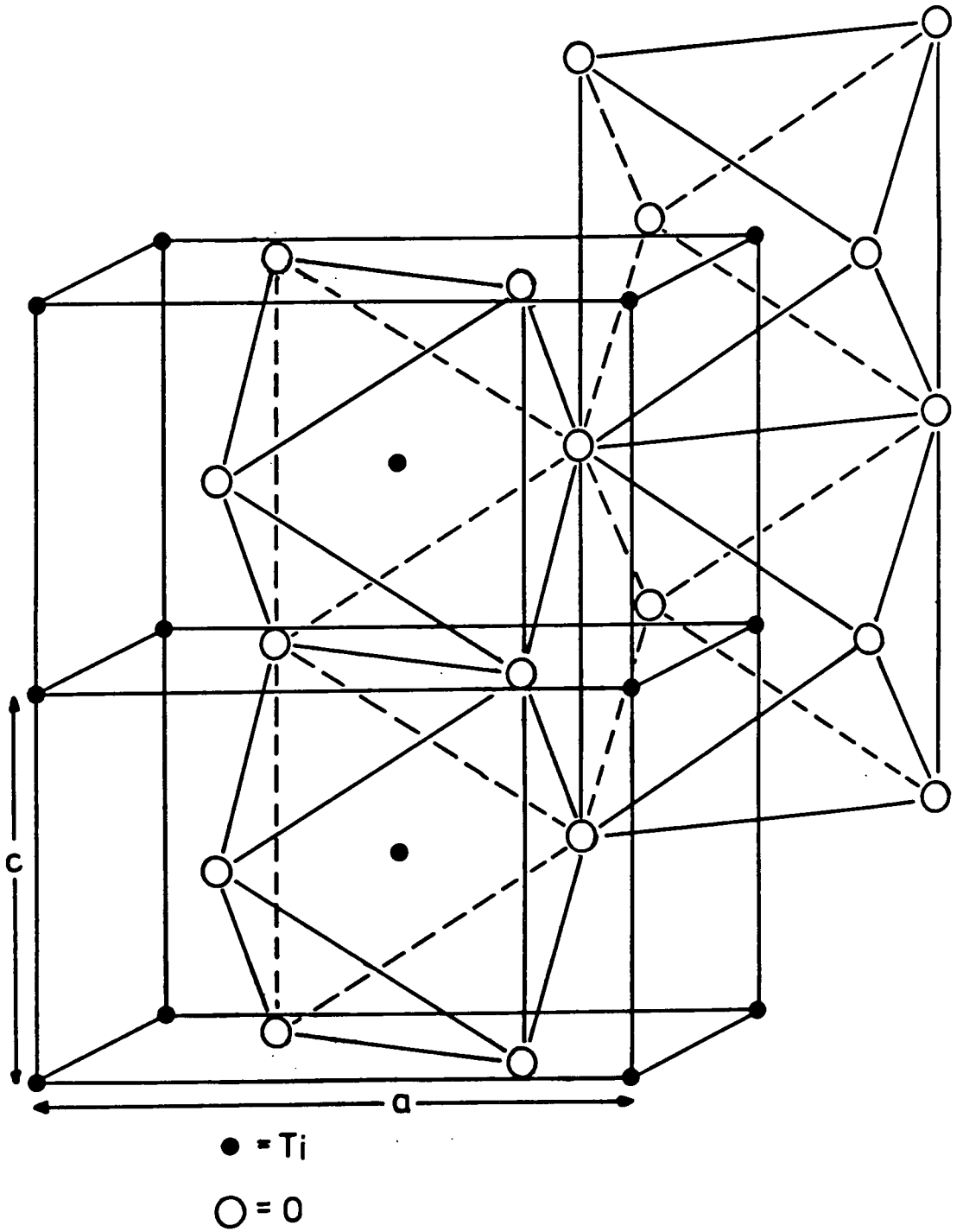


Figure 2.2.2 Unit cells of rutile showing the oxygen octahedra

2.3 NON-STOICHIOMETRY IN RUTILE

Non-stoichiometry in oxides may consist of two main types; either oxygen deficiency or metal deficiency with respect to the stoichiometric composition. Non-stoichiometry in a compound is equivalent to the presence of point defects. If a charged defect is formed in a stoichiometric crystal, a complementary point defect with the opposite effective charge must also exist to conserve the electrical neutrality of the crystal. Kroger and Vink [14] list several types of point defect which are possible in a near stoichiometric compound. The most important of these are Schottky defects which are vacancies of both cation and anion and Frenkel defects which are vacancies and interstitials of the same component.

Non-stoichiometric titanium dioxide has been studied extensively, particularly for use as a semiconducting electrode for the photoelectrolysis of water following the work of Fujishima and Honda [15]. Marucco et al [16] have performed measurements on quenching from a high temperature thermodynamic equilibrium to define the photochemical behaviour of TiO_{2-x} . Kofstad [17] and Forland [18] interpret the defects responsible for non-stoichiometry as oxygen vacancies. Pickard and Gerdanian [19] base the analysis of their results on a statistical thermodynamic model which leads to doubly ionised oxygen vacancies at low deviations from stoichiometry and to interstitial titanium, Ti^{3+} and Ti^{4+} , at higher deviations. Both Dirstine and Rosa [20] and Alcock [21] suggest the existence of Ti^{4+} interstitials. Marucco et al [22] conclude that the defects induced by reduction processes in rutile are both oxygen vacancies and titanium interstitials, their respective importance being governed mainly by temperature. Oxygen vacancies are prominent at lower temperatures while interstitial titanium becomes dominant at higher temperatures.

2.4 BAND STRUCTURE OF RUTILE

The work of Cronemeyer [23] on the electrical conductivity, optical absorption and photoconductivity of rutile shows that the band gap is about 3.0 eV wide. A difference in band gap measured by polarised radiation [24-26], electroabsorption [27] or electroreflectance [28] has been detected for $E_{\perp}c$ compared with $E_{\parallel}c$ of about 30 meV. The latter two methods yield spectra characteristic of band to band transitions and give convincing evidence for a 3.0 eV band gap. Most experimental data on electrical transport properties [29-32], optical absorption [33,34] and x-ray spectroscopy [35] indicate that the conduction states have a predominantly 3d character and are separated by about 3.0 eV from the oxygen 2p valence band edge.

An analysis of the band structure of rutile has been given by Adler [36] and a schematic diagram is shown in figure 2.4.1. This analysis was based on calculations for SrTiO_3 by Kahn and Leydendecker [37]. The result shows that TiO_2 is a semiconductor with a 3 eV gap separating the filled oxygen 2p band from the empty titanium 3d band.

Vos [38] has presented a semi-quantitative analysis of the band structure of rutile based on a linear combination of orthogonalised atomic orbitals (LCAO) calculation, using Ti-3d, O-2p and O-2s orbitals and retaining only nearest neighbour interactions. The energy bands of rutile along some high symmetry directions in the Brillouin zone are shown in figure 2.4.2. The top of the valence band is near $k=0$ and the bottom of the conduction band is near $k=(\pi/a, \pi/a, 0)$. The minimum near $k=(\pi/a, 0, \pi/c)$ is some 0.12 eV higher.

2.5 CARRIER MOBILITY IN RUTILE

Electron transport in rutile has been studied extensively in the past; at low temperatures by a combination of Hall effect and conductivity mechanisms, at high temperatures by doping with niobium or zirconium or by a combination of

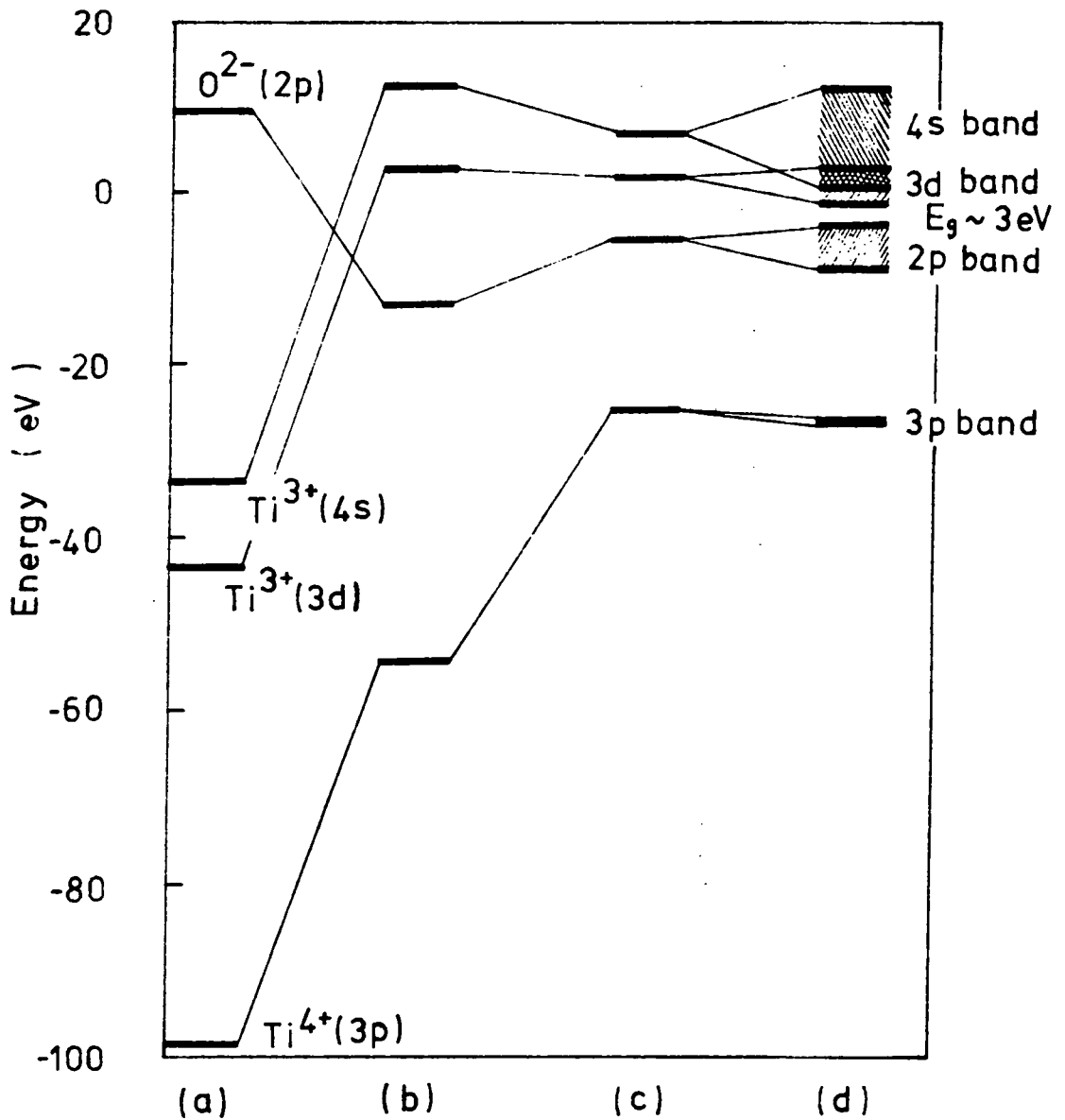
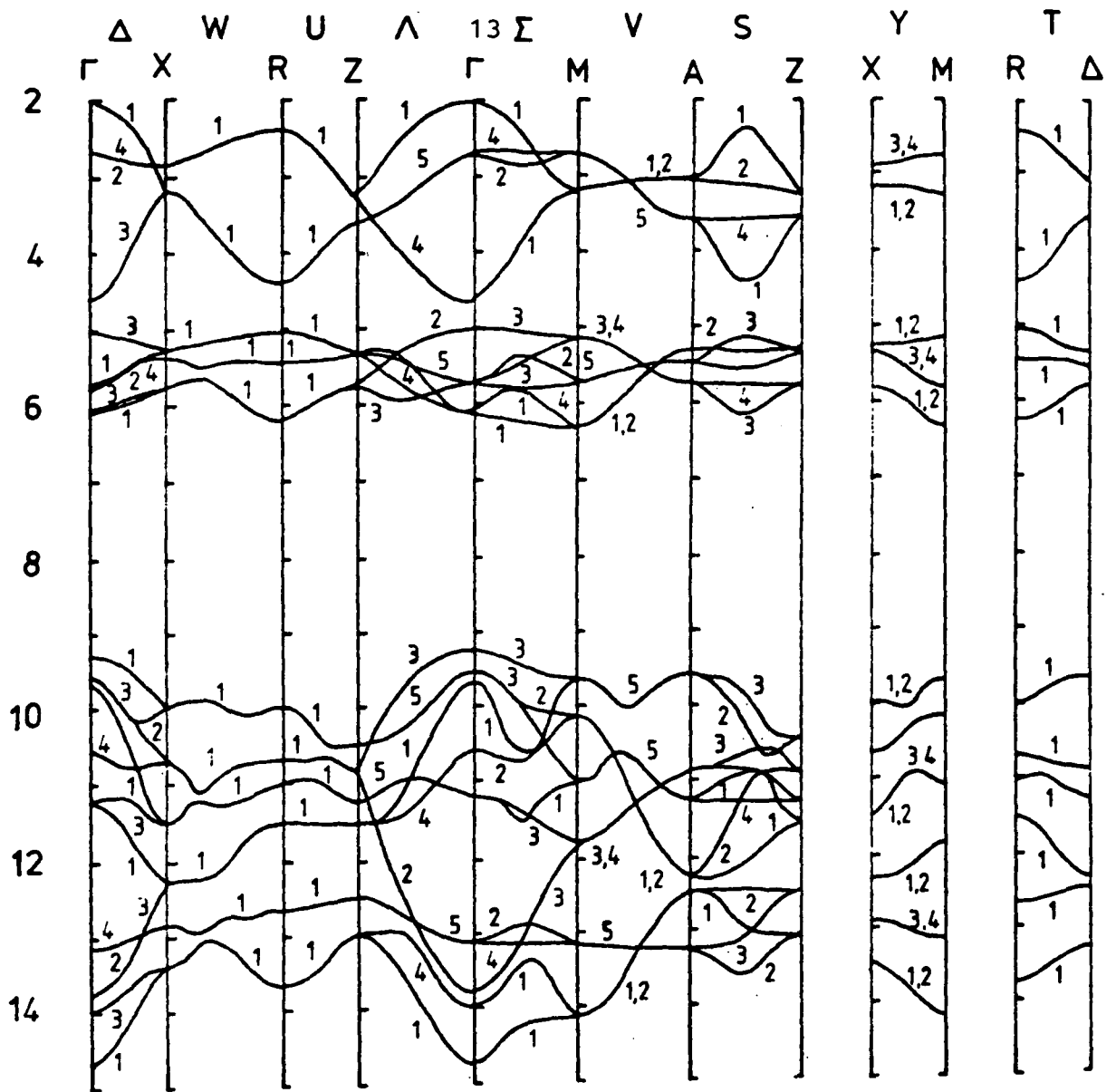


Figure 2.4.1 Sketch of the energy band structure of pure, stoichiometric TiO_2 , based on a tight binding approximation; (a) free ion energies, (b) effects of Madelung potential, (c) screening and covalency effects, (d) bandwidth effects. after Adler[36]



The eigenstates are labelled according to the symmetry of the corresponding eigenfunction

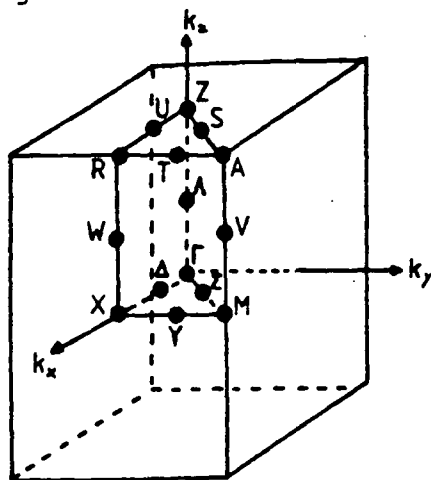


Figure 2.4.2 Energy bands of rutile along some high symmetry directions in the Brillouin zone

thermogravimetric and conductivity data.

The mobilities deduced from Hall effect measurements yield values of mobility parallel to the c-direction (μ_{\parallel}) of between 0.6 and 1.5 $\text{cm}^2\text{V}^{-1}\text{s}^{-1}$ and mobility perpendicular to the c-direction (μ_{\perp}) between 0.16 and 0.3 $\text{cm}^2\text{V}^{-1}\text{s}^{-1}$ at room temperature. The value of the anisotropy ($\mu_{\parallel}/\mu_{\perp}$) was found to be 4.5 ± 0.5 at room temperature by Acket and Volger [31] and about 3.5 by Bogoroditskii et al [39]. Bogomolov et al [40,41] found the anisotropy to be a decreasing function of temperature reaching 2.0 at 500K. At high temperatures μ_{\parallel} is still higher than μ_{\perp} but a comparison of the results of Blumenthal et al [42] and Marucco et al [22] yields a lower anisotropy: $\mu_{\parallel} \approx 0.12 \text{ cm}^2\text{V}^{-1}\text{s}^{-1}$ and $\mu_{\perp} \approx 0.08 \text{ cm}^2\text{V}^{-1}\text{s}^{-1}$. This has been confirmed by Greener et al [43]. By doping TiO_2 with niobium, Baumard and Tani [44] and Tani and Baumard [45] found a mobility of $0.1 \text{ cm}^2\text{V}^{-1}\text{s}^{-1}$ for polycrystalline samples at high temperature. Poumellec et al [46] have made a critical analysis of the previous works on mobility measurements in rutile. They suggest a mobility governed by acoustic phonon scattering over a large range of temperatures with optical phonon scattering possibly occurring at high temperatures.

When a free electron exists in an ionic lattice, the ions in that lattice are disturbed by the Coulomb forces and the crystal becomes polarised. If the electron moves through the crystal, the region of polarisation moves with it contributing an extra term to the inertia of the electron. The electron together with the polarisation that it creates is known as a polaron. If the coupling between the electron and the lattice is sufficiently large the electron may be trapped by the polarisation field surrounding it. For this to happen, the spatial extent of the of the polaron must be small (of the order of one lattice spacing or less). The trapped electron can still move through the lattice if the polarisation field can be overcome by thermal fluctuations. Under these conditions, however, the electron will be trapped at the next positive ion site. The motion of a small polaron in the 'hopping mode' then consists of a series of jumps from one positive ion site to the next.

There is a discrepancy between the values of Hall mobility and drift mobility in rutile which has been shown to be characteristic of small radius polarons [40,47]. Bogomolov et al [48] have found evidence for the existence of small polarons in rutile. They suggested an effective mass, m^* , of $150 m_0$ and a hopping energy of 0.13 eV for conduction perpendicular to the c-axis and 0.07 eV for conduction parallel to the c-axis. Several other workers have reported the effective mass of electrons in rutile. Early workers [28,48] reported values of m^* of between 10 and $30 m_0$ while more recent workers [32,50-54] have reported values between 7 and $13 m_0$.

CHAPTER 3**THEORY**

- 3.1 Introduction**
- 3.2 Thermal equilibrium and steady-state phenomena**
- 3.3 Thermally stimulated luminescence and conductivity**
- 3.4 Metal-semiconductor contacts**
- 3.5 Deep level transient spectroscopy**

3.1 INTRODUCTION

Defect levels determine the density of carriers in the transport bands of extrinsic semiconductors and wide band gap materials. Because of the strong temperature dependence of thermal emission rates and, frequently, also of non-radiative capture rates, the study of thermal transport properties over a range of temperatures provides a natural means to obtain information on these trapping parameters. Thermal transport properties in this connotation refer only to those related to charge carrier transport in a rather broad sense, but not to thermal conductivity, impurity diffusion, etc., which involve the transport of phonons or atomic species.

Thermal emission rates are not, in most cases, measured directly. A notable exception is the thermally stimulated capacitance technique (section 3.5). A plot versus temperature of some transport property that is influenced or dominated by thermal carrier release from traps permits the determination of thermal ionisation energies that are equal to or related to trap depths. Interpretation of measured data in terms of a physical model for the reaction kinetics will often lead to the determination of the trap density and capture cross-sections.

In general, various different types of trap and recombination centres may be present and their involvement in the reaction kinetics will greatly change with temperature. The temperature range in which a specific trap dominates must therefore be identified. This is most conveniently achieved with the aid of non-isothermal temperature scans during which thermally stimulated luminescence (TSL) and thermally stimulated conductivity (TSC) are monitored. In semiconductors such novel techniques such as deep level transient spectroscopy (DLTS) may be also used.

All trap-spectroscopic techniques which are based on thermal transport properties have in common that the interpretation of empirical data is often ambiguous because it requires knowledge of the underlying model of reaction

kinetics. Consequently, a large number of published trapping parameters are uncertain or not very accurate. Data obtained by TSC and TSL techniques, particularly when applied to insulators and photoconductors are no exception [55-59].

3.2 THERMAL EQUILIBRIUM AND STEADY-STATE PHENOMENA

The most direct and, in semiconductors, the easiest way to determine carrier densities and thermal activation energies is to measure ohmic conduction. The current density is given by:

$$J = qF (n\mu_n + p\mu_p) \quad (3.1)$$

The method requires ohmic contacts, a knowledge of the carrier mobilities, μ_n or μ_p , and the type of the majority carriers. F is the electric field strength and q the electronic charge. The thermal activation energy, obtained by a semilogarithmic plot of the ohmic current versus $1/T$, is usually interpreted as either half the bandgap in intrinsic semiconductors or the trap depth of the dominant trap in extrinsic semiconductors. In compensated materials such a simple interpretation is not necessarily possible. Particularly in wide gap materials which need be only weakly compensated, Schmidlin and Roberts [60] have shown that the empirical activation energy of ohmic conduction is the arithmetic average of the depths of the dominant electron trap and the dominant hole trap. Their analysis excludes, however, the case when the Fermi-level or quasi-Fermi level falls within a few times kT of a dominant trap level. Here again the activation energy is equal to the thermal ionisation energy of the trap. Precisely this situation is encountered in most TSC experiments that are performed under ohmic conditions.

Ohmic conduction is present only as long as the carrier density is not influenced by the electric field. At sufficiently high fields, usually with the voltage applied to a sample sandwiched between the contacts (one of which must be an ohmic or an injecting contact [60]), carriers are injected into the material and the current becomes space charge limited [61-63]. If only one type of carrier is injected, e.g.

electrons in an n-type material, the current density, J , increases with F^2 [60]:

$$J = 9 F^2 \epsilon \mu N_c \exp[-(E_c - E_t)/kT] / 8LN_t \quad (3.2)$$

Here ϵ is the dielectric constant, L the length of the sample, N_c the density of states in the conduction band and N_t the density of the dominant electron trap of depth $(E_c - E_t)$. Again, measuring J as a function of temperature permits the determination of the trap depth and, with the aid of a simple model, the trap density as well as the mobility [60].

3.3 THERMALLY STIMULATED LUMINESCENCE AND CONDUCTIVITY

3.3.1 Introduction

The occurrence of thermally stimulated luminescence (TSL) and thermally stimulated conductivity (TSC) during a thermal scan of a previously excited sample is probably the most direct evidence for the existence of electronic trap levels in these materials. A TSC or TSL spectrum (frequently referred to as a 'glow curve') usually consists of a number of more or less resolved peaks in plots of luminescence intensity or electrical conductivity versus temperature which, in most cases, may be attributed to the thermal excitation of carriers from traps. The appearance of a glow curve is a direct representation of the fact that the escape probability of trapped carriers is a sharply increasing function of temperature and the supply of trapped carriers is limited to start with, increases and then decreases with their continued thermal release from the trap.

Since the escape probability of carriers from trapping sites is proportional to $\exp(-E/kT)$ [64], the location of a glow peak on the temperature scale provides encoded information about the value of the thermal activation energy, E . Hence, a glow curve represents a spectrum of energies which are required to release carriers from the various species of traps in the material.

The procedures used to decode the glow spectrum and retrieve the desired

trap-spectroscopic data appear, at first sight, obvious and straightforward. A measured curve is analysed to obtain such characteristics as the location of the peak on the temperature scale, its width, rate of initial rise, etc. These data are then used to compute trapping parameters via an appropriate model for the reaction kinetic processes that occur during the temperature scan. However, exact knowledge of the proper kinetics is necessary for this analysis to yield quantitative values. The most simple model of reaction kinetics which actually yields TSL and TSC peaks is the single trap model [55,64-80] described in section 3.3.4.

The topics of TSC and TSL developed along two lines. The first one merely made use of the capability of deep levels in certain insulating materials to store charge carriers at or below room temperature for a long time, sometimes thousands of years, without being much concerned about the mechanism of this information storage and its eventual retrieval in a thermal scan in the form of thermoluminescence or, less frequently, thermally stimulated conductivity. Very successful applications of these phenomena in dosimetry, geology, archeology, etc., were the result. The other approach concentrated on quantitative trap level spectroscopy: e.g. employing curve fitting techniques on the basis of the single trap model [77,79] and attempting to understand completely the detailed features of TSC and TSL curves calculated within the framework of this model [74-76,78-80]. Any well resolved glow peak that may reasonably be expected to be due to a single type of trap can be fitted with a solution of the single trap model by appropriately adjusting several out of a set of many model parameters. Unfortunately, such a fit is not unique, since a number of different simple model descriptions are conceivable in addition to the single trap model.

The origin of this lack of uniqueness has to be traced to the fact that both TSL and TSC are only indirect trap-spectroscopic methods. In contrast to thermally stimulated capacitance techniques (section 3.5), the thermal release from traps or the capture of charge carriers by traps is not measured directly. Rather, the transient traffic of thermally released carriers towards available levels is monitored

at various points along the way. Even though radiative transitions that occur during the thermal scan are measured in TSL, the primary objects of investigation in both TSL and TSC experiments are non-radiative transitions between the ground level or excited level of the trap and the conduction or valence band.

3.3.2 Non-isothermal phenomena

The interaction of high energy radiation with a solid produces hot electrons which may multiply by impact ionisation and subsequently quickly thermalise so that free carriers and excitons remain. The excess free carriers do not represent stable excited states of the solid. A fraction of them recombine directly after thermalisation, either radiatively or by multiphonon emission. In most materials non-radiative transitions to defect states in the gap are the dominant mode of decay. The lifetime of free carriers, $\tau = 1/(f\langle v \rangle \sigma)$, is determined by their thermal velocity, $\langle v \rangle$, the density of recombination centres, f , and the capture cross-section, σ , and may span the range from 10 to 10^{-14} s [61]. Electrons captured above the demarcation level for electrons and holes captured by states below the hole demarcation level may be trapped. The condition for trapping is that the occupied electron trap has a very small cross-section for recombining with a free hole. After the decay of the excess free carriers due to recombination and trapping transitions, the solid is in an excited state. The concentration of the remaining free carriers is now determined by the balance between thermal emission of carriers from the traps, retrapping transitions and capture by recombination centres.

If the excitation takes place at a low temperature such that the thermal emission rate of carriers from the traps is very small, the perturbed equilibrium will exist for a long time and, upon an appropriate increase of the sample temperature, the relaxation process can proceed at a rate that permits observation by measuring the conductivity of the sample (TSC) or the luminescence (TSL) emitted by radiative recombination of the carriers thermally released from the traps.

3.3.3 Non-radiative transitions

A defect state can act either as a trap or a recombination centre, depending on its location with respect to the demarcation levels for electrons and holes.

Capture of carriers in traps or recombination centres can be non-radiative and thermal emission of carriers from traps is a non-radiative transition. Non-radiative recombination processes are difficult to identify because their occurrence can usually only be inferred from a low luminescence efficiency, η . η may be temperature dependent, decreasing with increasing temperature (thermal quenching) [81]. A number of simple models have been employed to explain this experimental observation. When radiative and non-radiative transitions compete within a luminescence centre, Mott and Gurney [82] and Seitz [83] found, using a configurational co-ordinate theory that:

$$\eta = [1 + c \exp(-E/kT)]^{-1} \quad (3.3)$$

where c is a constant and E an activation energy. A similar expression was obtained by Klassens [84] and Schön [85], although they postulated the existence of centres which thermally emitted holes into the valence band thus reducing the capture cross-section of these centres for radiative recombination with an electron from the conduction band.

The theory of non-radiative capture has been the subject of numerous papers and reviews [86-91]. Three plausible mechanisms for non-radiative capture have evolved; these are the Auger effect in which the energy lost by the captured carrier excites another nearby carrier in the crystal [91,92], cascade capture in which the electron loses energy by dropping down a ladder of closely spaced excited levels of the defect, emitting one phonon at each step [93-96] and multiphonon capture in which the energy of the electron is dissipated by multiphonon emission [86-90,97,98].

3.3.4 TSL and TSC kinetics

The thermally stimulated conductivity method was first introduced by Urbach [99], but did not come into extensive use until the first theoretical treatment was reported by Randall and Wilkins [64]. Since then many investigators have found this method useful for studying trap parameters in solids [56,78,100-105].

The simple model which is generally used to describe the TSL and TSC processes is shown in figure 3.3.1. We start with a solid that contains one single set of electron traps located at an energy level, E , below the conduction band. Electrons are thermally excited from the trap to the conduction band (transition 1) where they contribute to the conduction process. From this band they can either be retrapped (transition 2) or recombine with a hole trapped at a recombination centre (transition 3). The latter transition may be accompanied by the emission of light. The probability, P , that a trapped electron will escape from the trap to the conduction band at a temperature T is given by:

$$P = \nu \exp(-E/kT) \quad (3.4)$$

where ν is the attempt to escape frequency which is given by

$$\nu = N_c \langle \nu \sigma_n \rangle \quad (3.5)$$

To determine the TSC curve, the specimen is cooled to a temperature T_0 and excited so that the density of electrons trapped in the traps is n_{t0} which is assumed to be smaller than the total density of traps N_n . If the specimen is heated at a constant rate

$$w = dT/dt \quad (3.6)$$

then at some time t after the heating has begun, the rate of change of free electron density is

$$dn/dt = -n/\tau - dn_t/dt \quad (3.7)$$

where τ is the electron lifetime which is determined by recombination processes. The first term on the right represents the recombination rate of the free electrons, and the second term represents the rate of change of trapped electron density in the

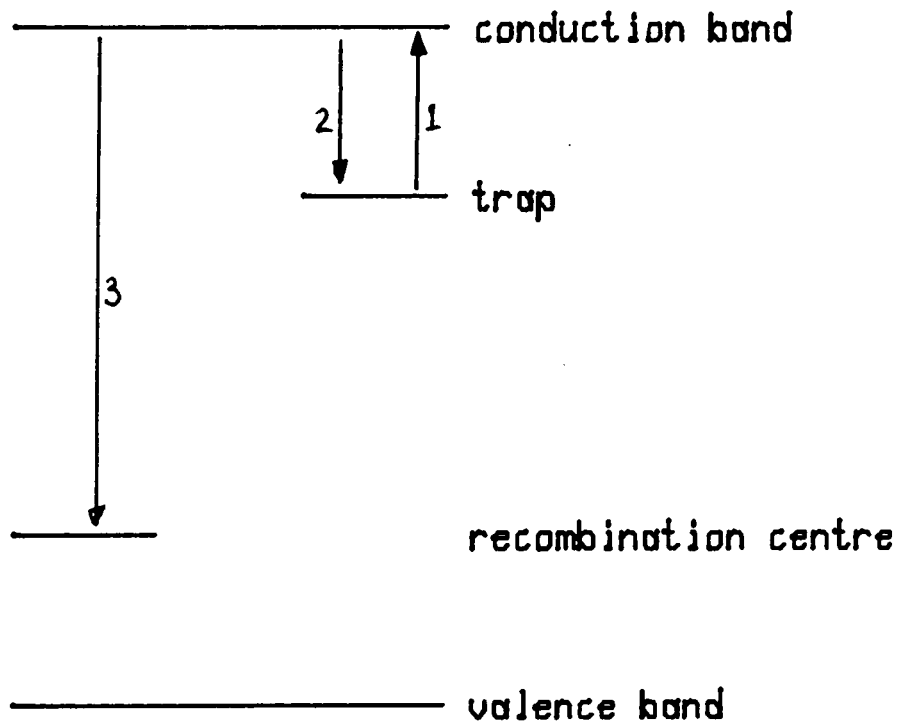


Figure 3.3.1 The simple model for TSC and TSL

traps, which is given by

$$dn_t/dt = -n_t v \exp(-E/kT) + n(N_n - n_t) \langle v\sigma_n \rangle \quad (3.8)$$

in which the first term on the right represents the rate of thermal release of trapped electrons, and the second term represents the rate of retrapping of free electrons.

Most theories are based on the assumption that τ is short so that $n/\tau > dn/dt$. With this assumption the general solution of equations (3.7) and (3.8) yields $n(t)$ and hence the thermally stimulated conductivity

$$\begin{aligned} \sigma(T) &= q\mu_n = -q\mu_n \tau \frac{dn_t}{dt} = -q\mu_n \tau w \frac{dn_t}{dT} \\ &= \frac{q\mu_n \tau N_c \langle v\sigma_n \rangle}{1 + \tau N_n \langle v\sigma_n \rangle} n_{t0} \exp \left[\frac{-E}{kT} - \frac{1}{w} \int_{T_0}^T \frac{N_c \langle v\sigma_n \rangle \exp(-E/kT)}{1 + \tau N_c \langle v\sigma_n \rangle} dT \right] \quad (3.9) \end{aligned}$$

where $T(t) = T_0 + wt$. Equation (3.9) is similar to that derived by Saunders and Jewitt [106]. To find the temperature at which σ is a maximum, we have to know the temperature dependence of μ_n , τ , N_c , v , and σ_n , which depend on energy band structure and carrier scattering and recombination processes, and thus vary from material to material. By assuming the following dependence of those parameters

$$\begin{aligned} N_c &= AT^{3/2}, \quad \mu_n = DT^{-b} \\ v &= BT^{1/2}, \quad \tau = \text{constant} \\ \sigma_n &= CT^{-a} \end{aligned}$$

and setting $d\sigma/dT = 0$ for the occurrence of the peak at $T = T_m$, we obtain

$$E/kT_m = \ln(T_m^2/w) + \ln(kN_c \langle v\sigma_n \rangle/E) - \ln(1 + \tau N_n \langle v\sigma_n \rangle) \quad (3.10)$$

for cases $E > kT_m$ [94]. Three special cases are considered as follows:

(A) Monomolecular recombination. For this case there is no retrapping or slow retrapping and so we can assume $\tau N_n \langle v\sigma_n \rangle \ll 1$. Thus, equations (3.8) and (3.10) reduce to those derived by Randall and Wilkins [64].

$$\sigma(T) = q\tau\mu_n N_c \langle v\sigma_n \rangle n_{t0} \exp \left[-E/kT - \frac{1}{w} \int_{T_0}^T N_c \langle v\sigma_n \rangle \exp(-E/kT) dT \right] \quad (3.11)$$

and

$$E/kT_m = \ln(kT_m^2 N_c \langle v\sigma_n \rangle / (wE)) \quad (3.12)$$

Since T_m depends on the heating rate w , Booth [107] and Bohun [108] have proposed using two heating rates to determine E from equation (3.12). Thus

$$E = kT_{m1} T_{m2} \ln(w_1 T_{m2} / w_2 T_{m1}) / (T_{m1} - T_{m2}) \quad (3.13)$$

Later, Hoogenstraaten [109] suggested using a number of heating rates so that $\ln(T_m^2/w)$ as a function of $1/T_m$ can be plotted; from this plot E and hence σ_n can be determined. Keating [110], following an argument similar to that of Randall and Wilkins, has derived the following formula for determining E :

$$kT_m/E = ((T'' - T')/T_m)(1.2\gamma - 0.54) + 5.5 \times 10^{-3} - ((\gamma - 0.75)/2)^2 \quad (3.14)$$

where $\gamma = (T'' - T_m)/(T_m - T')$, and T' and T'' are the temperatures at which $\sigma(T)$ attains the value $1/2 \sigma_m(T)$ on either side of T_m . Equation (3.14) is a good approximation when $10 < E/kT_m < 35$ and $0.75 < \gamma < 0.9$.

(B) Fast retrapping. For this case the recombination is mainly bimolecular and the free electrons can be assumed to be in thermal equilibrium with the trapped electrons in the traps and $\tau N_n \langle v \sigma_n \rangle \gg 1$. Thus equation (3.8) reduces to

$$\sigma(T) = (q \mu_n N_c / N_n) n_{t0} \exp\left[-E/kT - 1/(w \tau N_n) \int_{T_0}^T N_c \exp(-E/kT) dT\right] \quad (3.15)$$

This equation does not involve σ_n and it is not possible to determine σ_n from the measured glow curve. However, Böer et al [111] have shown that the magnitude of the recombination cross-section σ_R can be estimated by the following equation:

$$v \sigma_R = (E/(kT_m)) \cdot (w/(n_m T_m)) \quad (3.16)$$

where n_m is the density of free electrons at $T = T_m$. By setting $dn_t/dt = 0$ in equation (3.8) we obtain the condition for the occurrence of a peak in the glow curve and the following equation for determining E :

$$E/kT_m = \ln(N_c/n_m) + \ln(n_t/(N_n - n_t)) \quad (3.17)$$

By assuming that the peak occurs when the quasi-Fermi level coincides with the trapping energy level, the ratio $n_t/N_n = 1/2$ and equation (3.17) becomes [70]

$$E/kT_m = \ln(N_c/n_m) \quad (3.18)$$

Thus a plot of $\ln(n_m)$ as a function of $1/T$ should yield a straight line of slope E .

(C) Intermediate retrapping. Garlick and Gibson [73] have considered the case

in which a free electron has equal probability of recombining or being retrapped, and the TSC is given by

$$\sigma(T) = \frac{q\mu_n \tau N_c \langle v\sigma_n \rangle n_{t0}^2 \exp(-E/kT)}{N_n \left[1 + \frac{N_c \langle v\sigma_n \rangle}{N_n w} n_{t0} \int_{T_0}^T \exp(-E/kT) dT \right]^2} \quad (3.19)$$

Under this condition the recombination is mainly bimolecular. It is important to note that T_m depends on the ratio of n_{t0}/N_n (the fraction of traps occupied) for bimolecular recombination, but it is independent of n_{t0} for monomolecular recombination.

Equation (3.7) may be rewritten as

$$dn/dt = -dn_t/dt - \gamma n f \quad (3.20)$$

where γ is the capture coefficient for recombination and f is the density of empty recombination centres. The recombination coefficient, γ , is the sum of γ_r and γ_n , the coefficients for radiative and non-radiative recombination, respectively. The TSL intensity per unit volume is then

$$I(T) = \gamma_r n f \quad (3.21)$$

With the aid of the luminescence efficiency $\eta = \gamma_r / (\gamma_r + \gamma_n)$, we can write

$$I(T) = \eta \gamma n f \quad (3.22)$$

The analysis above has been for the case of a single trapping level; the analysis becomes complicated if two or more levels are involved. For these cases a computer solution may be necessary [78,94,112].

3.3.5 Analysis methods

Several expressions relating the trap depth to measurable quantities exist in the literature [58,64,70,73,74,107-111,113-128]. These can be used to calculate the trap depth from TSC and TSL curves. Most of the methods make use of the shift of the TSC and TSL maxima with different heating rates [58,70,107-109,111,113-119], while

others make use of geometrical approximations [120-124].

3.3.6 Reliability of trap depth determinations

In the derivation of the expressions on which these methods are based some more or less plausible assumptions or approximations are made. Whether these are allowed or not can easily be verified for the simple model when TSL and TSC curves are calculated without making simplifications. This can be done with the aid of a numerical procedure described by Hagebeuk and Kivits [80]. They applied most of the methods in the literature to these curves and subsequently compared the trap depth determined by analysis of the curve with that used in the numerical calculations to generate the curve.

In both the TSL and TSC cases, the methods of Hoogenstraaten [109], Bube [70], Haering and Adams [117] and Unger [58] produced the best value of trap depth. They concluded that, when the simple insulator model can be used, TSC and TSL measurements are a helpful tool in determining trapping parameters.

Kivits [129] has discussed extensions to the conventional simple insulator model. He showed that the values of trap depth determined after application of most of the methods described in the literature are unreliable if an extended model is used. These extensions include recombination via excited states, the presence of a trap distribution, donor-acceptor pair recombination, the presence of additional centres, temperature dependent rate parameters, thermal quenching of luminescence and scattering due to ionised defect centres. Only Hoogenstraaten's method [109] appeared to be rather insensitive for most of the extensions considered.

3.4 METAL-SEMICONDUCTOR CONTACTS

3.4.1 Introduction

Because of their importance in the electronic industry and as tools in the analysis of other fundamental physical parameters, metal-semiconductor contacts have been studied extensively. Recently, reproducible and near-ideal metal-semiconductor contacts have been fabricated with the help of modern transistor technology and improved vacuum technology.

3.4.2 Formation of barrier

The rectifying properties of a metal-semiconductor contact arise from the presence of an electrostatic barrier between the metal and the semiconductor [130]. This barrier is due to the difference in work function of the two materials. If the work function of the metal, ϕ_m , exceeds that of the semiconductor, ϕ_s , electrons pass from the semiconductor into the metal to equalise the Fermi levels, leaving behind a depletion region in the semiconductor in which the bands are bent upwards as shown in figure 3.4.1 for the case of an n-type semiconductor. Assuming that the region of the semiconductor where the bands are bent upwards is completely devoid of conduction electrons ('the depletion approximation'), the space charge is due entirely to the uncompensated donor ions. If these are uniformly distributed, there will be a uniform space charge in the depletion region and the electric field will increase linearly with distance from the edge of the depletion region. The magnitude of the electrostatic potential will increase quadratically and the resulting potential barrier will be parabolic in shape. This is known as a Schottky barrier [131]. It can be shown by a straightforward argument [132] that the amount by which the bands are bent upwards (the built-in potential V_{bi}) is given by

$$V_{bi} = \phi_m - \phi_s \quad (3.23)$$

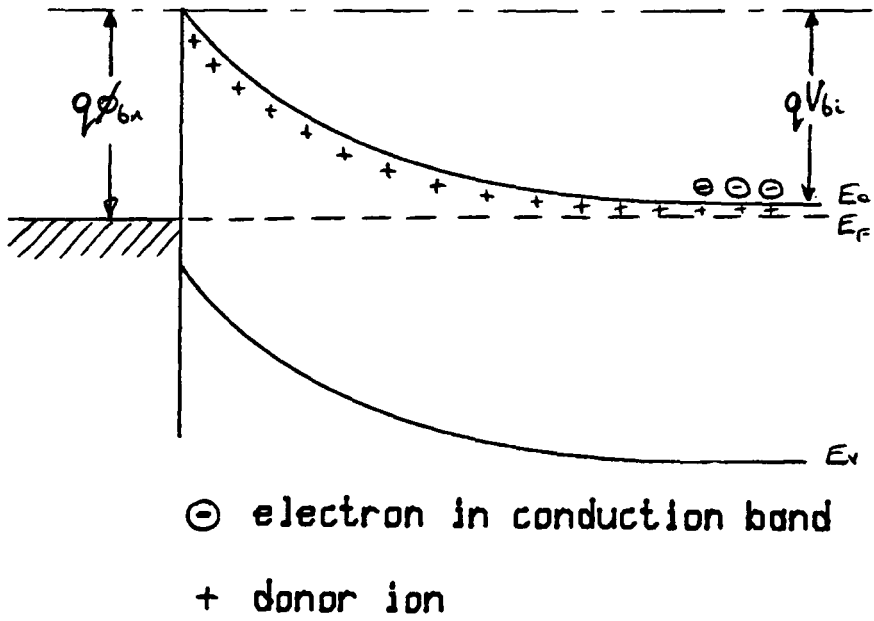


Figure 3.4.1 Band bending at a metal-semiconductor junction

If $\phi_m > \phi_s$, V_{bi} is positive and the bands are bent upwards; for the case of an n-type semiconductor this produces a barrier which the electrons have to surmount in order to pass from the semiconductor into the metal which leads to rectifying properties.

The barrier height as viewed from the metal, ϕ_b , is normally given, rather than the built-in potential. For an n-type semiconductor this is given by:

$$\begin{aligned}\phi_b &= V_{bi} + (E_C - E_F) \\ &= \phi_m - \chi_s\end{aligned}\quad (3.24)$$

where χ_s is the electron affinity of the semiconductor.

It is clear from the above discussion that when a metal is brought into intimate contact with a semiconductor, the conduction and valence bands of the semiconductor are brought into a definite energy relationship with the Fermi energy in the metal. Once this relationship is known, it serves as a boundary condition on the solution of Poisson's equation in the semiconductor.

Under the abrupt approximation that $\rho = qN_D$ for $x < W$ and $\rho = 0$, $dV/dx = 0$ for $x > W$, where N_D is the donor concentration, the depletion width, W , is given by:

$$W^2 = 2\epsilon(V_{bi} - V - kT/q) / (qN_D) \quad (3.25)$$

where the term kT/q arises from the contribution of the mobile carriers to the electric field. The electric field is given by:

$$|F(x)| = qN_D(W-x)/\epsilon \quad (3.26)$$

and the potential by:

$$V(x) = qN_D(Wx - x^2/2)/\epsilon \quad (3.27)$$

The space charge per unit area of the semiconductor, Q_{sc} , and the depletion layer capacitance per unit area, C , are given by:

$$Q_{sc} = qN_D W = [2q\epsilon N_D (V_{bi} - V - kT/q)]^{1/2} \quad (3.28)$$

$$C = \partial Q_{sc} / \partial V = [q\epsilon N_D / (2(V_{bi} - V - kT/q))]^{1/2} \quad (3.29)$$

Equation (3.29) can be rewritten in the form:

$$1/C^2 = 2(V_{bi} - V - kT/q) / (q\epsilon N_D)$$

$$-d(1/C^2)/dV = 2/(q\epsilon N_D)$$

$$\text{or } N_D = 2/(q\epsilon) \cdot (-dV/d(1/C^2)) \quad (3.30)$$

If N_D is constant throughout the depletion region, one should obtain a straight line by plotting $1/C^2$ versus V . The barrier height can be determined from the intercept on the voltage axis. If N_D is not constant, the differential capacitance method may be used to determine the doping profile.

3.5 DEEP LEVEL TRANSIENT SPECTROSCOPY

3.5.1 Capacitance detection of trap levels

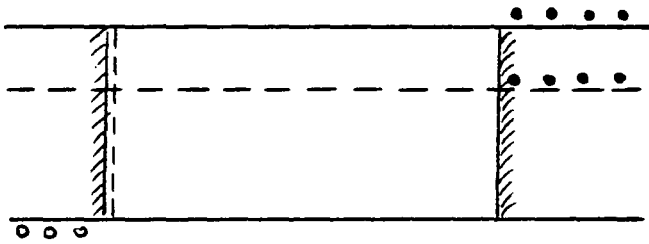
Trap levels in space charge layers may be detected by their effect on either the junction current or the capacitance. The current detection case is almost exactly analogous to the thermally stimulated currents which can be seen in a bulk insulator. The capacitance detection case, which yields the same basic information about traps as does current detection, is unique to semiconductor space-charge layers. A change in the charge density in the space charge layer will induce a corresponding change in the width, and hence in the capacitance, of the layer. Consequently, if the concentration of electrons trapped at deep levels is changed, either by thermal or optical capture or emission, this variation in trapped charge can be readily monitored by observing the corresponding change in the junction capacitance at constant bias voltage. All forms of capacitance spectroscopy are based on this fact. Thus, the focus in capacitance measurements is opposite to that of thermally stimulated conductivity thermoluminescence or photoconductivity. In these latter bulk phenomena one measures free carrier concentration and infers from this the properties of traps and recombination centres. In junction capacitance measurements, on the other hand, one measures the trapped carrier concentration directly. Thus the trap signals are more or less independent of one another and the analysis is considerably simplified. In the case of small trap concentrations where

the trap-induced capacitance change is much less than the overall junction capacitance, the thermal emission capacitance transients are simple exponential decays which are directly proportional to the electron occupation of the trap. For large trap concentrations, however, the situation is much more complex and the capacitance transients are non-exponential.

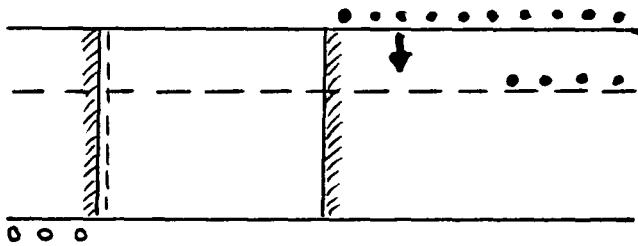
3.5.2 Bias voltage pulses

Voltage pulses superimposed on a steady-state reverse bias make it possible to almost totally decouple the measurements of capture and emission processes at deep levels. This is illustrated in figure 3.5.1 for a majority carrier pulse in a p^+n junction. Under steady-state conditions the traps in the upper half of the gap (majority carrier traps in n-type material) are empty. If the bias is momentarily reduced, part of the region which was formerly within the space charge layer is now in neutral material so that the traps are below the Fermi level. During the time that the bias is at this lower value, the deep levels may capture majority carriers and tend to become filled. Immediately after the pulse, the deep levels are again within the space charge layer where the capture rate is essentially zero. The capacitance will have changed due to the captured carriers and as these carriers are thermally excited a capacitance or current transient will be produced. The time constant of the transient will vary exponentially with the temperature of the sample. Thus a majority carrier pulse is essentially a means whereby the majority carrier concentration can be turned on and off in a small volume of the sample. Majority carrier capture dominates when the pulse is switched on, whereas majority carrier emission dominates when the pulse is turned off.

A spatial profile of the trap concentration may be obtained either by varying the steady-state bias voltage or by varying the amplitude of the majority carrier pulse. In either case the spatial region in which deep levels are observed is varied and the spatial profile may be obtained [133-137].



Quiescent reverse bias



Reduced reverse bias

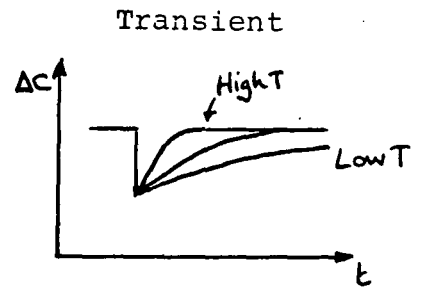
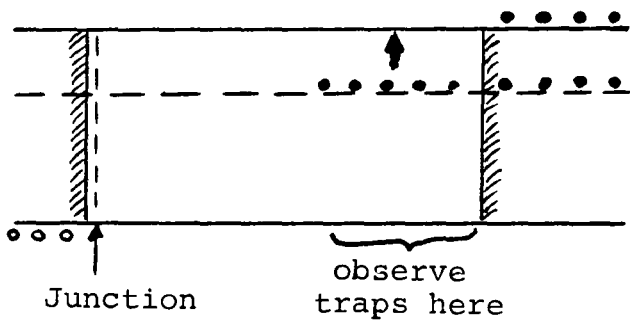


Figure 3.5.1 Effect of bias pulse on trap occupancy in a depletion layer

3.5.3 The rate window concept

The basic idea of the DLTS technique is the rate window concept. If we consider a train of repetitive bias pulses applied to the sample, we then have a signal which consists of a series of transients with a constant repetition rate. As the temperature is varied, the time constant of the transients varies exponentially with $1/T$. If the capacitance versus time information from a transient capacitance experiment is processed so that a selected decay rate produces a maximum output, then a signal whose decay time constant changes monotonically with time will produce a peak when the rate passes through the rate window. In consequence, on observing a repetitive capacitance transient from a p-n junction or Schottky barrier through such a rate window, and on slowly scanning the sample temperature (thereby changing the thermal emission rate and, therefore, the capacitance decay rate) a peak appears in the output versus temperature plot. Such a plot is called a DLTS spectrum.

There are a number of ways in which the DLTS rate window may be achieved in practice. The method proposed in the original DLTS experiments involved the use of a dual-gated integrator (double boxcar) [138]. In this method the transient amplitude is sampled at two times t_1 and t_2 after the pulse, as shown in figure 3.5.2. The DLTS signal is the difference between the transient amplitude at these two times. As can be seen from figure 3.5.2, there is no difference in the signal at these two gate times for either very slow or very fast transients, corresponding to low or high temperatures, respectively. However, when the transient time constant τ is of the order of the gate separation, a difference signal is generated and the boxcar output passes through a maximum as a function of temperature. This is a DLTS peak. For capacitance measurements the rate window can be expressed in terms of the transient time constant giving rise to the maximum double boxcar output [138,139],

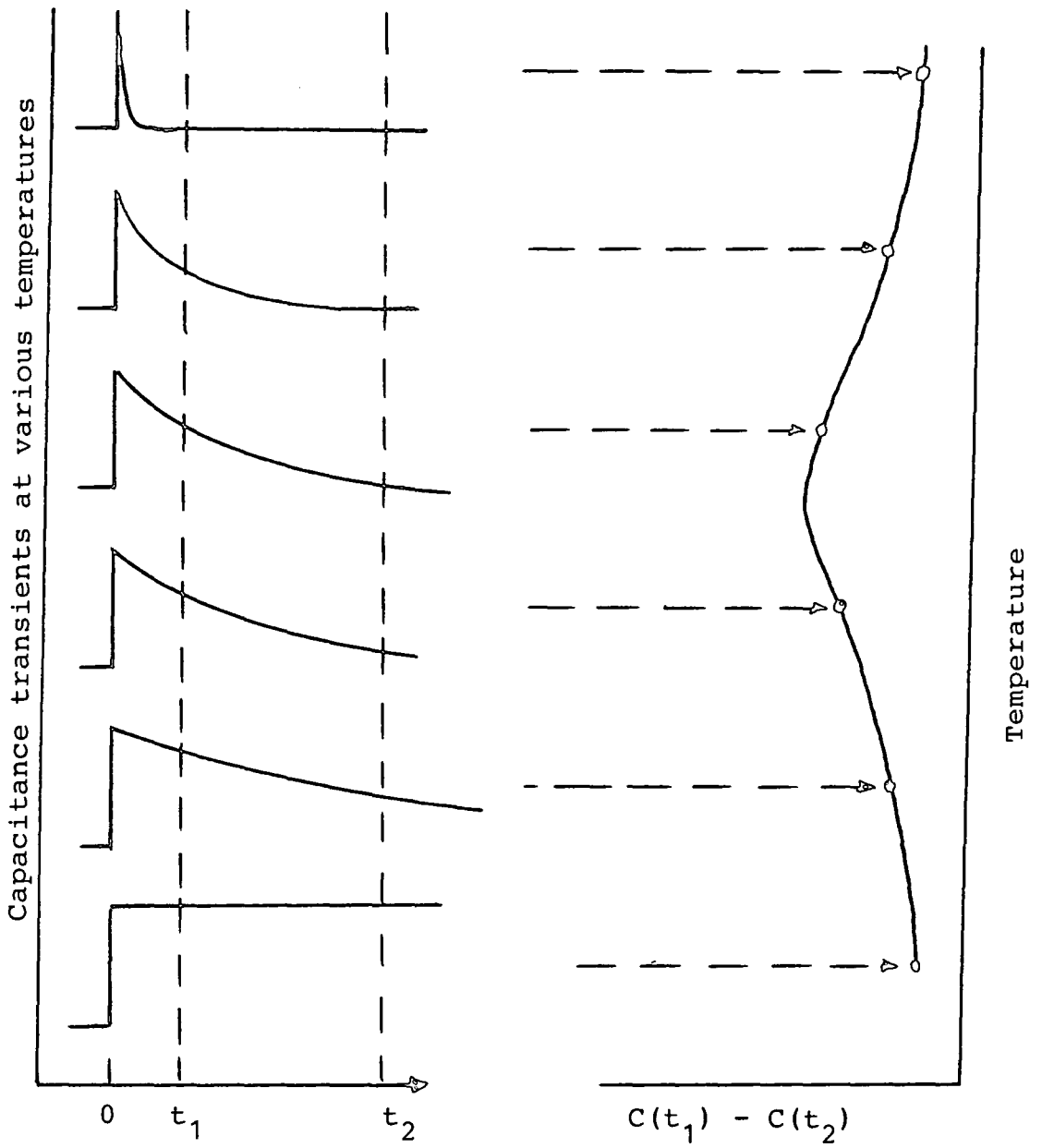


Figure 3.5.2 Sampling of capacitance transient

namely

$$\tau_{\max} = (t_1 - t_2) / \ln(t_1/t_2) \quad (3.31)$$

Equation (3.31) is also a very good approximation for the case of relatively wide boxcar gates, provided t_1 and t_2 are taken as the midpoint of each sampling gate. Indeed the best way to use a boxcar is with relatively wide gates.

3.5.4 Determination of trapping parameters

DLTS spectra are repeated with a number of different rate windows. Since, at the DLTS maximum, the rate window and the emission rate are equal

$$\tau_m = (N_c \sigma_n \langle v \rangle)^{-1} \exp(E/kT_m) \quad (3.32)$$

As $N_c \propto T^{3/2}$ and $\langle v \rangle \propto T^{1/2}$, a plot of $T_m^2 \tau$ versus $1/T_m$ should yield a straight line of slope E/k , provided that σ_n is not thermally activated. The intercept on the $T_m^2 \tau$ axis enables the capture cross-section σ_n to be calculated [138,140,141].

CHAPTER 4

EXPERIMENTAL TECHNIQUES

- 4.1 Sample preparation
- 4.2 Doping
- 4.3 Contacts and mounting
- 4.4 Liquid nitrogen cryostat
- 4.5 Optical apparatus
- 4.6 Photoluminescence measurements
- 4.7 Thermoluminescence measurements
- 4.8 Thermally stimulated conductivity measurements
- 4.9 Deep level transient spectroscopy

4.1 SAMPLE PREPARATION

4.1.1 Crystals

Crystal samples were cut using a diamond saw from boules aligned by Laue π -ray back reflection. Most samples were rectangular prisms with typical dimensions of $5 \times 3 \times 1 \text{ mm}^3$ and with their large faces perpendicular to the c-axis (to within $\pm 1^\circ$).

After cutting, the dice were mechanically polished on a lapping wheel with successively finer diamond paste down to a grit size of $1 \mu\text{m}$ and then further polished with $0.3 \mu\text{m}$ anatase powder. Great care was exercised during the polishing to maintain a slight bevel on the corners; this bevelling prevented flakes breaking off.

Surface damage remaining after polishing was removed by chemically etching in boiling concentrated sulphuric acid for thirty minutes. The samples were rinsed first in deionised water and then in methanol. Some minor surface scratches still remained after this chemical treatment.

Samples of niobium doped rutile and undoped rutile intended for reduction for use in DLTS experiments were cut thinner (typically 0.5 mm thick) and then hand polished to a final thickness of 0.25 mm .

4.1.2 Powders

Powder samples for photoluminescence and thermoluminescence measurements could be prepared quite simply. Some of the powder was mixed with a 5% solution of nitrocellulose in butyl acetate. This powder- binder mixture was painted onto a glass microscope cover slip which was then dried in a hot air cabinet.

An alternative, more complicated method, was also used for powder samples. A hydraulic press was used to compress 250 mg of powder in a 1 cm diameter circular

steel die with a force of 10^5 N. The resulting cylindrical pellet was fired in air in a horizontal furnace for 1 hour at 1000°C and allowed to cool slowly. This technique produced a sintered ceramic pellet with excellent mechanical strength.

4.2 DOPING

4.2.1 Crystals

Two boules were available that had been doped during growth. These were doped with niobium and iron, respectively. The plasma growth of rutile crystals and their doping during growth has been described by Hillhouse [10] and Hillhouse and Woods [142]. Other samples were doped by diffusion. The crystal and metal dopant were placed together in a quartz ampoule which was evacuated to a pressure of 10^{-7} torr and sealed. The ampoule was then heated in a furnace to a temperature sufficient to give a vapour pressure of the dopant metal of greater than 10^{-4} torr. This temperature was maintained for 24 hours and the sample was then cooled slowly to room temperature. An anneal in an oxygen flow for 24 hours at 1000°C was then performed to restore stoichiometry.

Reduced rutile crystals were produced by the method of Szydlo and Poirier [143]. The crystal was heated in an evacuated quartz ampoule at 800°C for 10 hours and then quenched by plunging the ampoule into cold water. The colour of the crystal changed from pale straw yellow to pale blue-black.

4.2.2 Powders

Powder samples were doped by an aqueous solution method. A soluble chloride of the dopant was made into an aqueous solution and a known quantity of rutile powder mixed in to form a slurry. The slurry was placed in an oven at 120°C and the water evaporated. The resulting powder was fired at 800°C in oxygen for an hour to

diffuse in the dopant and then broken up with a pestle and mortar.

By varying the concentration of the aqueous solution, the doping concentration of the powder could be varied. Powders doped with chromium and iron were produced by this method. Mass spectrographic analysis gave doping concentrations of 35, 70, 135 and 405 ppm for the iron doped powders and 48, 95, 275 and 315 ppm for the chromium doped powders.

4.3 CONTACTS AND MOUNTING

Vacuum deposited silver was used to form ohmic contacts on both single crystal and ceramic pellet samples. The silver was evaporated through a brass mask in a chamber evacuated to 10^{-5} torr. Crystal samples had contacts applied to the two smallest faces while pellets had a large 8 mm diameter contact on one circular face and a smaller 4 mm diameter contact on the opposite face.

To ease mounting in the cryostat and making electrical contact, the sample was first attached to a microscope cover slip using a silver loaded conducting epoxy. Crystal samples were mounted with one large face in contact with the slide and were stuck down by the small faces with the evaporated contacts. Contact wires, approximately 2 cm long, were embedded in the silver epoxy before it set. Pellet samples were mounted in a blob of silver epoxy by the face with the large contact. The epoxy was painted out to one side of the pellet to allow a wire to be attached to make contact to the back of the sample. A contact wire was bonded to the top contact with silver epoxy.

The glass slide was attached to the copper cold finger of the cryostat using a thin smear of silicone high vacuum grease which acted as an adhesive and also improved thermal contact between the glass slide and the cold finger. A clamp held the slide in place. The contact wires were soldered to leads in the cryostat which were connected to external BNC sockets via feed-throughs mounted in the cryostat wall. The temperature of the sample was measured by a copper-constantan

thermocouple, one junction of which was 'soldered' with indium metal to the glass slide close to the sample. Direct contact between the thermocouple and the sample introduced excessive electrical noise when small currents were to be measured.

For the reduced rutile and niobium doped rutile samples for DLTS studies the contact and mounting procedure was different. A rectifying contact was made by evaporating a 2 mm diameter gold dot onto one of the large area faces of the sample under high vacuum. A silver dot was evaporated onto the opposite face to provide an injecting contact and the sample was mounted by this face onto a 10 mm square of thin copper sheet using the silver epoxy. The copper sheet was, in turn, mounted onto the cold finger of the cryostat. A phosphor-bronze wire clamp was used to hold the copper sheet in place and to provide an electrical connection to the back contact. Another phosphor-bronze wire with thin gold wire wrapped around the end was used to make contact to the gold dot. A thermocouple was pressed against the side of the sample and a 'thermal compound' paste was used to give this a good thermal contact whilst maintaining electrical isolation.

4.4 LIQUID NITROGEN CRYOSTAT

For optical and electrical measurements the samples were mounted in the metal cryostat illustrated in figure 4.4.1.

The upper part of the cryostat was made from German-silver which reduced the heat losses from the copper cold finger and formed a Dewar. The two quartz windows were removable and were held in position with the cryostat under vacuum by O-ring seals. The vacuum in the cryostat was provided by a rotary pump.

The sample could be cooled by pouring liquid nitrogen into the central tube of the cryostat to which the cold finger was attached. Subsequent heating of the sample was achieved by inserting a Kanthal wire heater coil, wound inside a silica tube, into the central tube and passing a current of up to 2.3 amps from a 24 Volt d.c. supply. Temperatures between 77 and 400 K were attainable in this system with heating rates

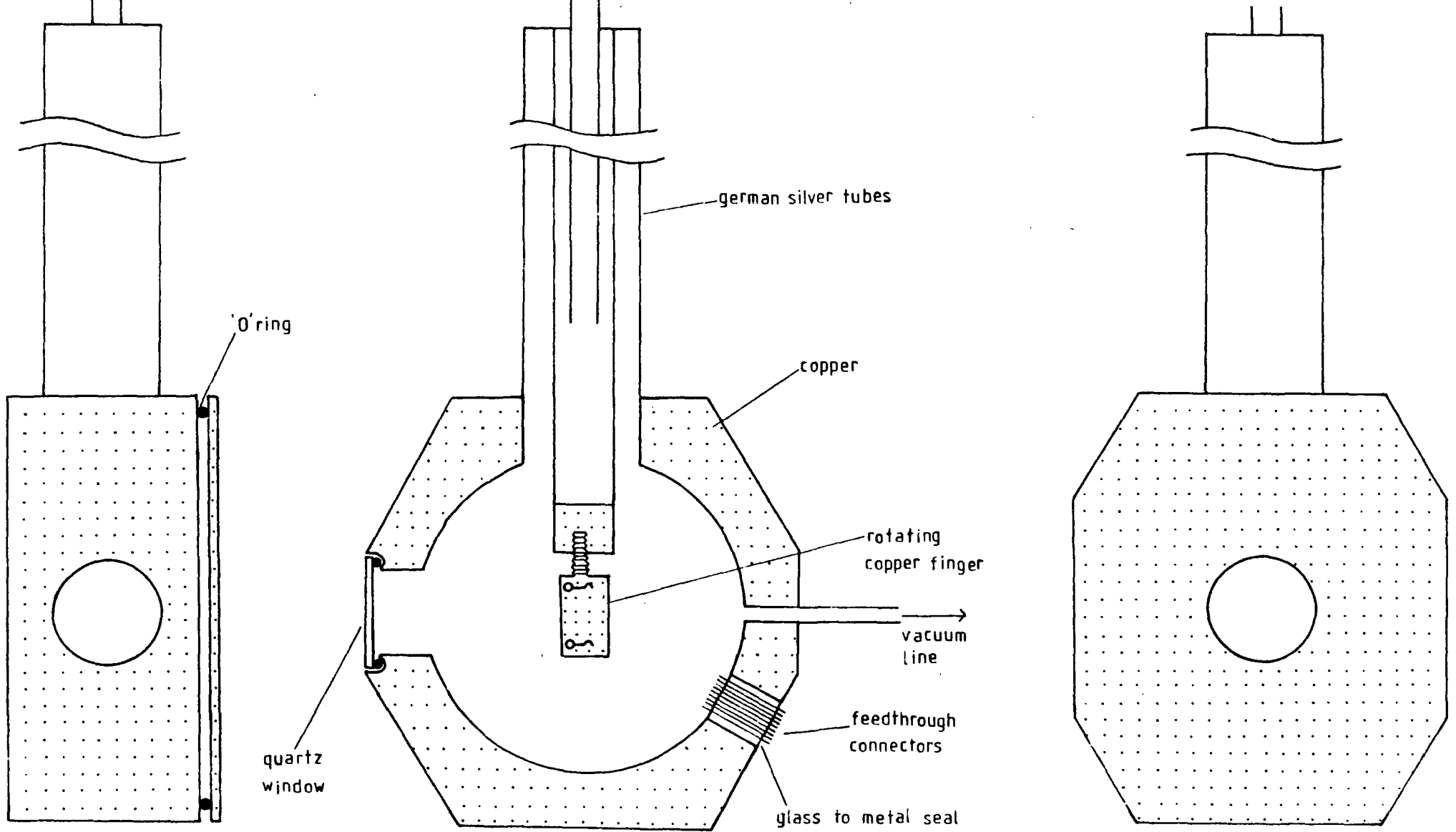


Figure 4.4.1 Liquid nitrogen cryostat

between 0.08 and 0.6 Ks⁻¹.

4.5 OPTICAL APPARATUS

Since the luminescence from rutile peaks in the vicinity of 850 nm, the detector was required to have an adequate response in this region. For this reason an RCA developmental type C3-1034, 2 inch diameter, head-on 11 stage Quantacon photomultiplier with a caesium doped gallium arsenide chip as the photocathode was used. No other photomultiplier operated further into the infra-red without requiring a liquid nitrogen operating temperature.

The photomultiplier bias was supplied by a Brandenburg type 475R power supply. Biases up to 2000 V could be applied to the photomultiplier.

A 1 M Ω load resistor was connected across the output of the photomultiplier and the voltage generated across this resistor was monitored by a Keithley model 610C electrometer. During an experiment, a permanent record was obtained by connecting the analogue output from the electrometer to a chart recorder to obtain a continuous trace of luminescence intensity against time. A micro switch on the input to the recorder, when operated, produced a blip on the trace which could be used, for example, to mark the temperature every five or ten degrees.

A Hilger and Watts D330 Mk II diffraction grating monochromator was used for measuring the spectral distribution of the photoluminescence emission.

Excitation was provided by a light from a 250 W compact mercury vapour lamp which was passed through a Chance OX1 glass filter to isolate the 365 nm mercury line and a bath of copper sulphate solution to remove near infra-red radiation [144].

4.6 PHOTOLUMINESCENCE MEASUREMENTS

Figure 4.6.1 shows the experimental arrangement for the observation of photoluminescence emission spectra. An Oriel G-772-7800 long pass filter was used

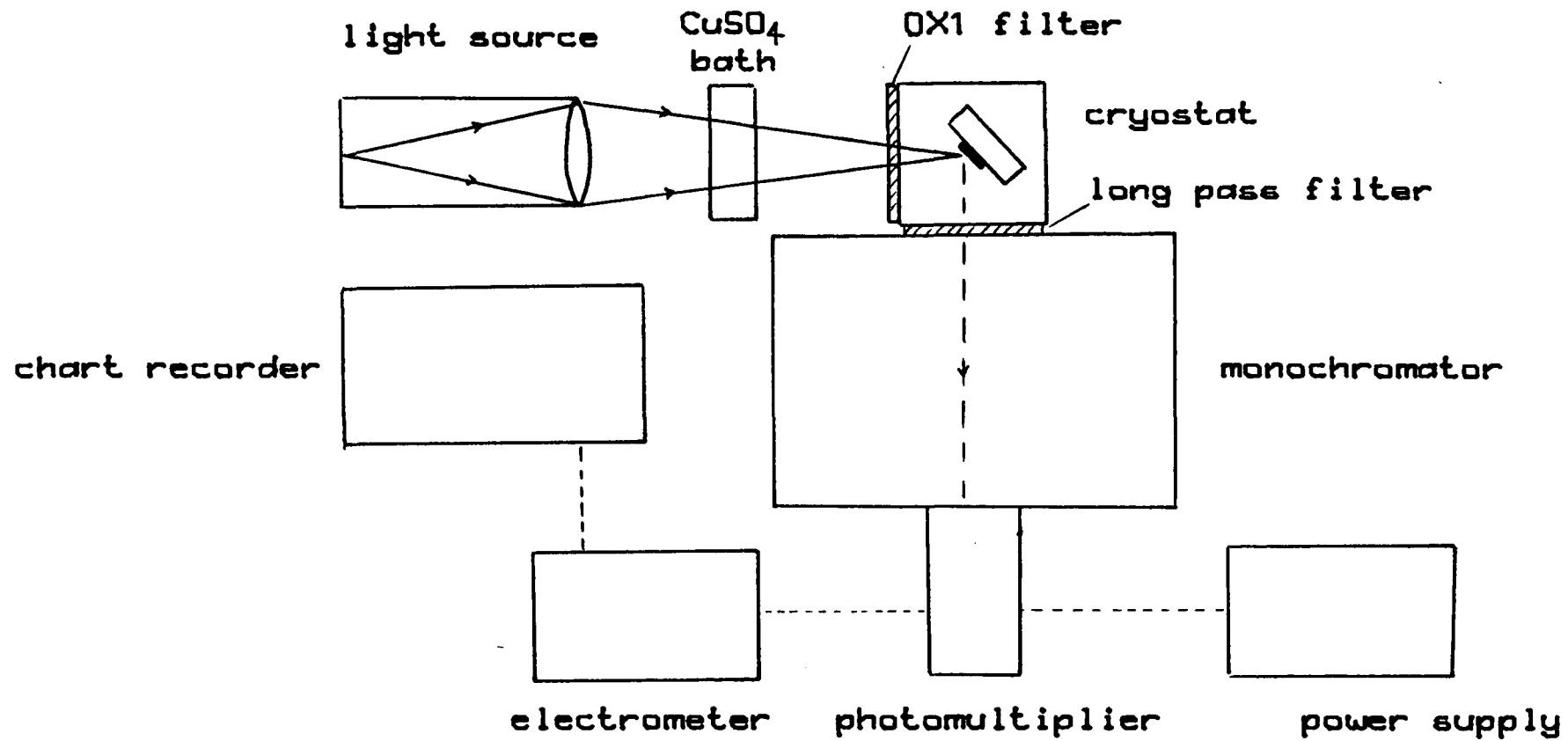


Figure 4.6.1 Experimental arrangement for observing photoluminescence emission spectra

to isolate the emission from higher orders of the excitation. The spectrum was recorded by monitoring the output from the photomultiplier as the monochromator was scanned through the wavelengths.

Photoluminescence emission intensity as a function of temperature was measured using the arrangement shown in figure 4.6.2. The output from the photomultiplier was monitored as the sample was heated from 80 to 400K and recorded on the chart recorder. Blips were made on the trace at intervals of 10K to correlate the position on the trace with the sample temperature.

4.7 THERMOLUMINESCENCE MEASUREMENTS

The experimental apparatus for obtaining thermoluminescence spectra is essentially the same as that shown in figure 4.6.2.

Prior to measuring thermoluminescence spectra, the sample was heated to 400 K in the dark and then cooled to 77 K. This procedure put the sample into a known, reproducible condition. The sample was then illuminated with light of wavelength 365 nm filtered from the mercury lamp through the Chance OX1 glass filter and the copper sulphate bath. After 10 minutes a shutter on the cryostat input window was closed to cut off the illumination and the cryostat was covered in a black cloth to eliminate any stray light. The sample was then heated and the luminescence monitored. Spectra were repeated at heating rates between 0.08 and 0.6 Ks⁻¹ to enable the peaks to be analysed.

4.8 THERMALLY STIMULATED CURRENT MEASUREMENTS

Thermally stimulated current measurements were initiated in a similar manner to thermoluminescence, as described above. After excitation a d.c. bias of up to 25 V was applied across the sample and the current flowing through the sample was monitored as the temperature was raised. A Farnell stabilised power supply was used

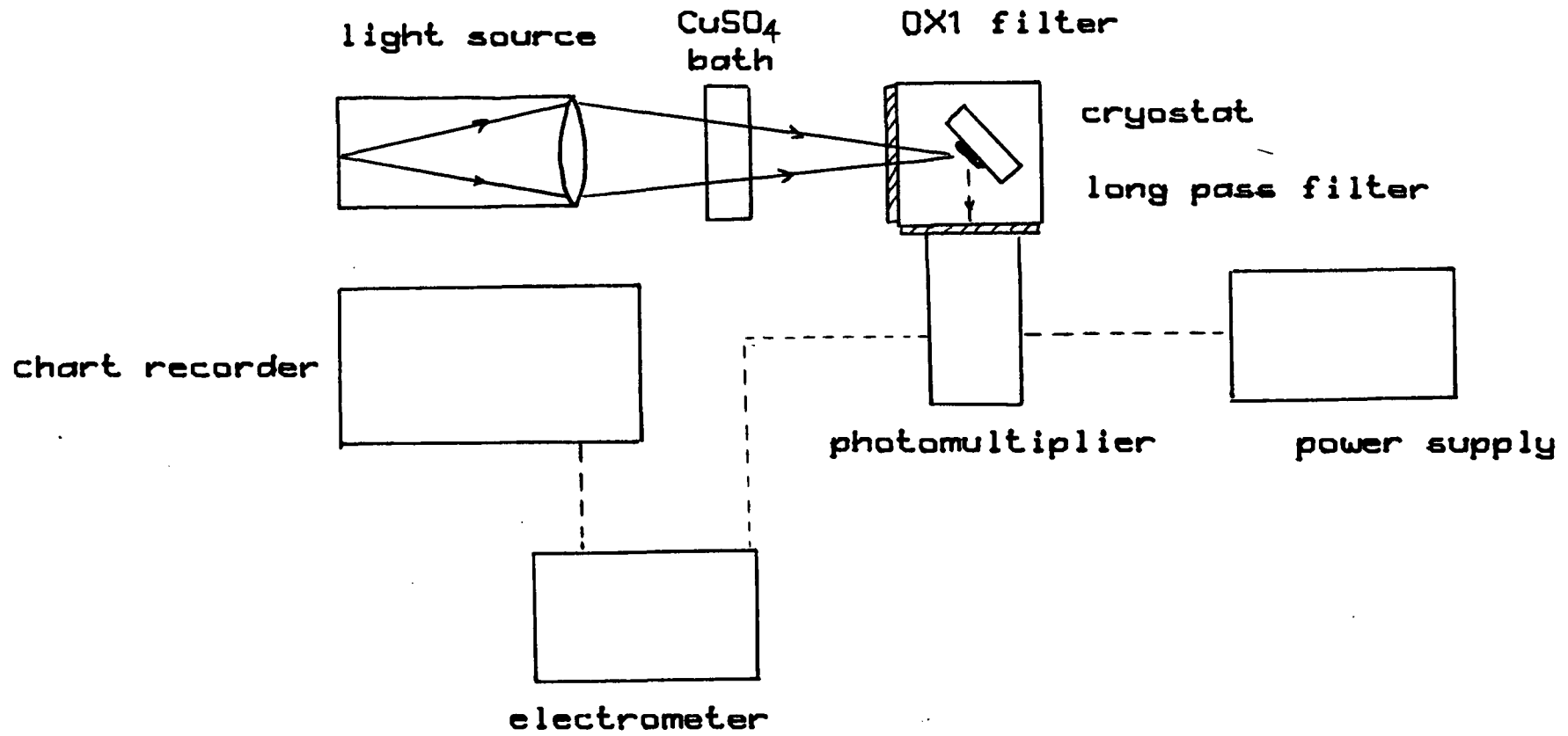


Figure 4.6.2 Experimental arrangement for observing photoluminescence intensity

as the voltage source. The Keithley model 610C electrometer could measure currents as low as 10^{-14} A. The analogue output from the Keithley was recorded on the chart recorder.

4.9 DEEP LEVEL TRANSIENT SPECTROSCOPY

A block diagram of the experimental apparatus for DLTS measurements is shown in figure 4.9.1. A Boonton model 72B capacitance meter was used to monitor the junction capacitance of the Schottky barrier devices.

The rate window was realised by the double boxcar technique. A single boxcar integrator can be formed by using a scan delay generator (Brookdeal 9425) to drive a linear gate (Brookdeal 9415). In response to a trigger pulse the scan delay generator produces a gating pulse of a chosen width after a chosen delay time. This gating pulse is fed into the linear gate as is the transient signal to be sampled. For the duration of the gating pulse the linear gate measures the value of the input signal and averages it.

Using two sets of such instruments, a double boxcar was available for the realisation of the DLTS rate window. The two boxcars were set to give averaged values of the capacitance at times t_1 and t_2 after the bias pulse. The two signals were input to a difference amplifier which gave an output proportional to $C(t_1) - C(t_2)$. This signal was recorded on the Y-axis of an X-Y chart recorder, the X-axis being driven by the thermocouple attached to the sample.

A steady state reverse bias of 3 V was applied to the sample, with a bias pulse to reduce this to 0 V for 1 ms. The DLTS spectrum against temperature was obtained simply by allowing the sample to warm up slowly from liquid nitrogen temperatures.

Spectra were recorded for a number of rate windows between 6 and 182 s^{-1} . Taking $t_2 = 3t_1$ was found to be the optimum setting for the rate window.

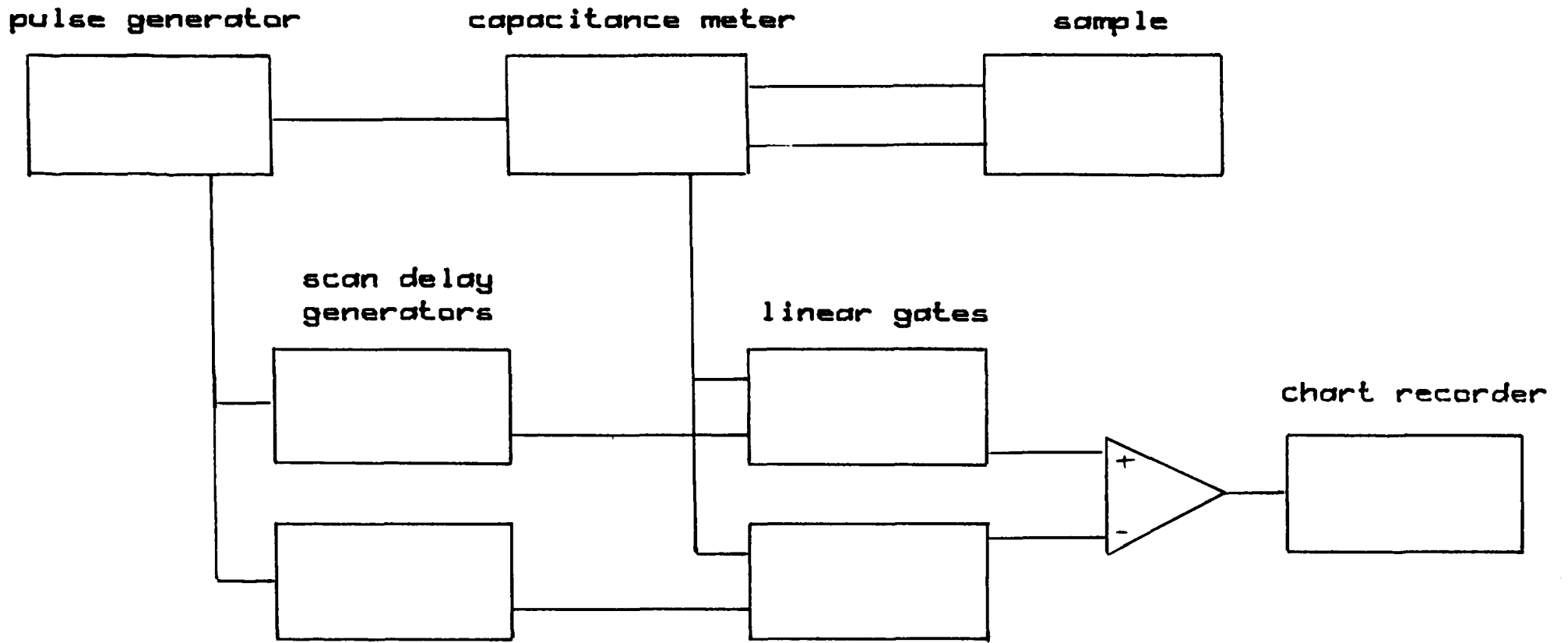


Figure 4.9.1 Schematic of DLTS experimental arrangement

CHAPTER 5

UNDOPED RUTILE

- 5.1 Introduction**
- 5.2 Material Preparation**
- 5.3 Photoluminescence**
- 5.4 Thermally stimulated luminescence and conductivity**
- 5.5 Reduced rutile**
- 5.6 Summary**

5.1 INTRODUCTION

In order to gain insight into the effects of adding dopants to a material, it is first necessary to study samples of the undoped material. This chapter describes the results of investigations into nominally undoped samples of single crystal rutile from two sources. The first set of samples came from boules grown at the Central Laboratories, Tioxide International Ltd., Stockton on Tees, by R. Hillhouse using the plasma fusion technique [10,142]. These are referred to as TI samples. The second set came from a boule from the National Lead Company, USA, which had been grown by a Verneuil flame fusion method [145]. These are referred to as NL samples.

A brief description of the material preparation is followed by sections describing results from photoluminescence, thermally stimulated luminescence and conductivity and from measurements on undoped but reduced rutile. The experimental techniques employed have been described in chapter 4.

5.2 MATERIAL PREPARATION

As the material under investigation was nominally undoped, no special preparation was needed in addition to the cutting, polishing, etching, and mounting of the samples as described in chapter 4. The exception to this was for the reduced rutile samples which were heated in a vacuum to make them semiconducting. A rectifying contact on one of the faces was also necessary for these samples.

5.3 PHOTOLUMINESCENCE

5.3.1 Photoluminescence emission spectra

Figure 5.3.1 shows a photoluminescence emission spectrum obtained at 77 K from a sample of undoped rutile cut from a TI boule. The spectrum is also shown

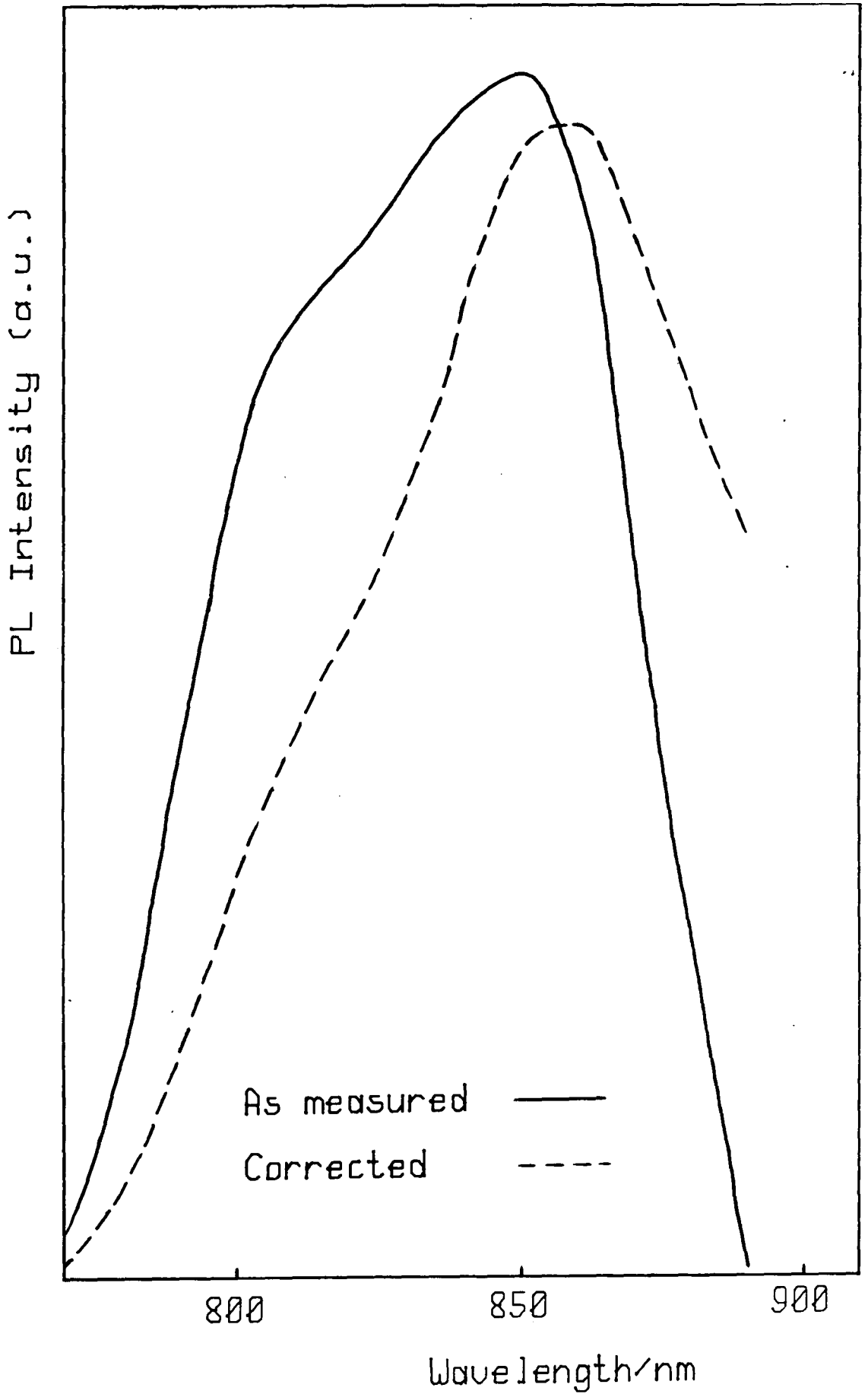


Figure 5.3.1 Photoluminescence emission intensity

after correction for the spectral response of the measurement system.

Emission occurs over a broad band centred on about 860 nm with a noticeable shoulder on the low wavelength side. The same broad band emission spectrum was observed from samples from the NL boule. The NL samples had a higher intensity than the TI samples by a factor of about 2.

This result is in good agreement with the luminescence observed by Hillhouse [10]], Ghosh et al [146] and Grabner et al [147]. Ghosh et al attributed the emission to an interstitial titanium (Ti^{3+}) ion. Grabner et al observed considerable structure in the band by measuring the emission under high resolution at 4.2 K and attributed the emission to substitutional chromium (Cr^{3+}) ions present as unintentional impurities in the lattice.

5.3.2 Temperature dependence of the photoluminescence

The temperature dependence of the luminescence intensity for an undoped TI sample is shown in figure 5.3.2 and that for an undoped NL sample in figure 5.3.3. Both results show the same structure; the intensity increases slightly with increasing temperature up to a maximum at about 190 K and then decreases rapidly with temperature. The intensity of the luminescence from the NL sample was higher than that from the TI sample by the same factor of about 2 that was observed in the measurement of the emission spectra.

Since the stimulating radiation remained constant throughout the heating of the sample, the reduction in intensity corresponds to a reduction in luminescence efficiency for some reason. The reduction in efficiency at high temperatures may be explained by thermal quenching of the luminescence, as described in chapter 3 and summarised here. An electron in an excited state of the luminescence centre can undergo a transition to the ground state which results in luminescence emission, or it may be thermally excited into the conduction band. At low temperatures there is insufficient energy for the latter process and all electrons in the excited state of the

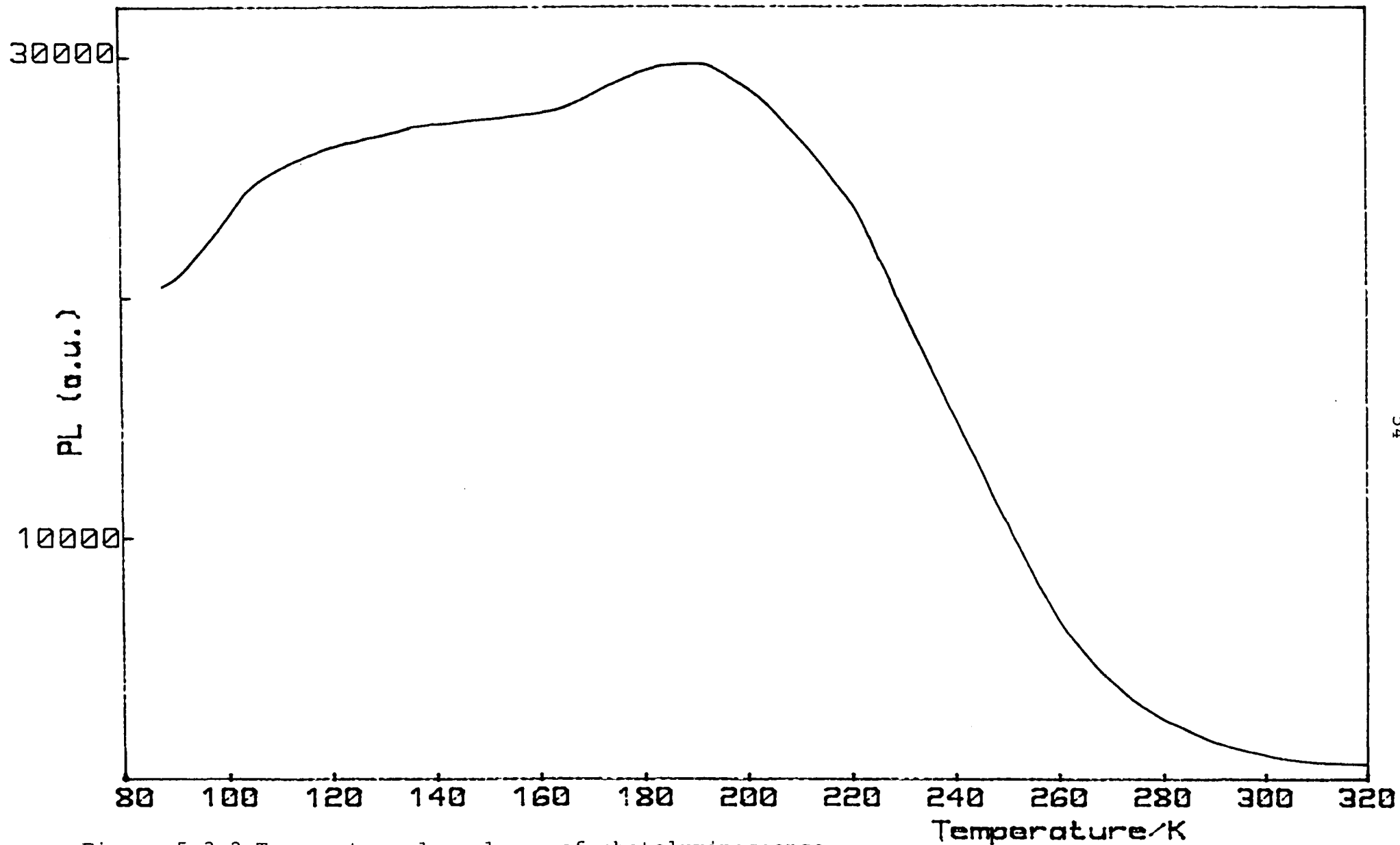


Figure 5.3.2 Temperature dependence of photoluminescence
for $T\bar{I}$ sample

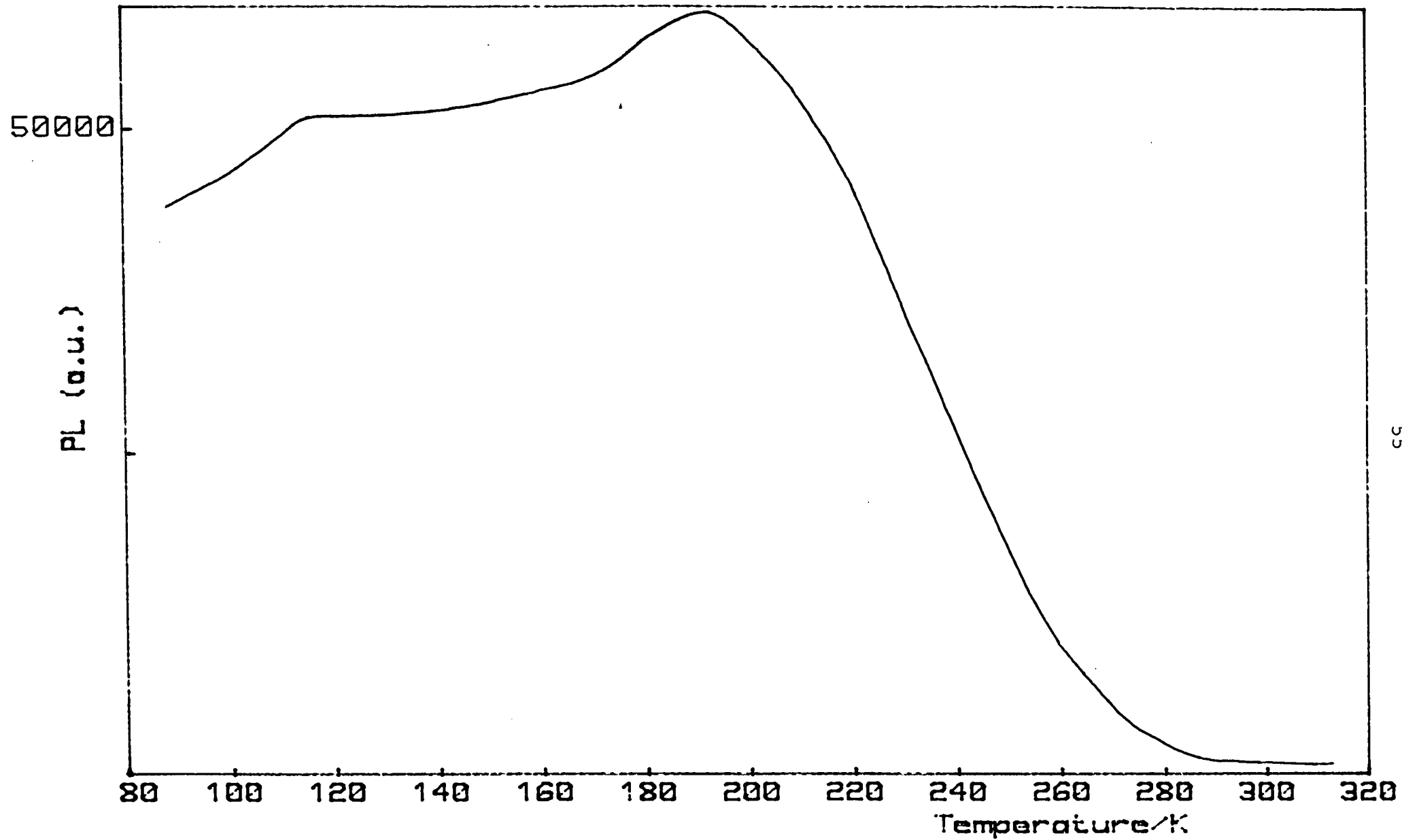


Figure 5.3.3 Temperature dependence of photoluminescence for NL sample

luminescence centre undergo the luminescent transition. At higher temperatures some of the excited state electrons are thermally excited to the conduction band rather than undergoing a luminescent transition and the luminescence efficiency is reduced. The expression for the efficiency, η , in these circumstances is (section 3.3.6):

$$\eta = [1 + c \exp(-E/kT)]^{-1}$$

where E is the activation energy for excitation to the conduction band. Rearranging gives:

$$c \exp(-E/kT) = (1-\eta)/\eta$$

so that a plot of $\ln[(1-\eta)/\eta]$ against reciprocal temperature should yield a straight line of slope $-E/k$.

Such plots for the results shown in figure 5.3.2 and 5.3.3 are shown in figures 5.3.4 and 5.3.5, respectively. The maximum luminescence intensity at 190 K was taken as having an efficiency of unity. Both plots give a good fit over a range of more than 100 K implying that the assumption of $\eta=1$ at the maximum was reasonable. The activation energy determined from the plots is 0.35 ± 0.01 eV in both cases.

Ghosh et al [148] show that the luminescence decay time of the radiative transition in undoped rutile is constant with temperature until 150 K and then decreases as the temperature is raised further. They attribute this reduction in decay time to thermal excitation of the excited state of the luminescence centre competing with the luminescent transition, thus reducing the effective lifetime of the excited state. They calculate a value of 0.18 ± 0.02 eV for the activation energy which is considerably different from the 0.35 eV determined from the thermal quenching of the luminescence described above. It should be noted that the maximum luminescence intensity occurs at 190 K whereas the reduction in decay time reported by Ghosh et al started at 150 K. The higher transition temperature is consistent with a higher activation energy since the quenching process is thermally activated, although this does not account for the difference since the same mechanism is

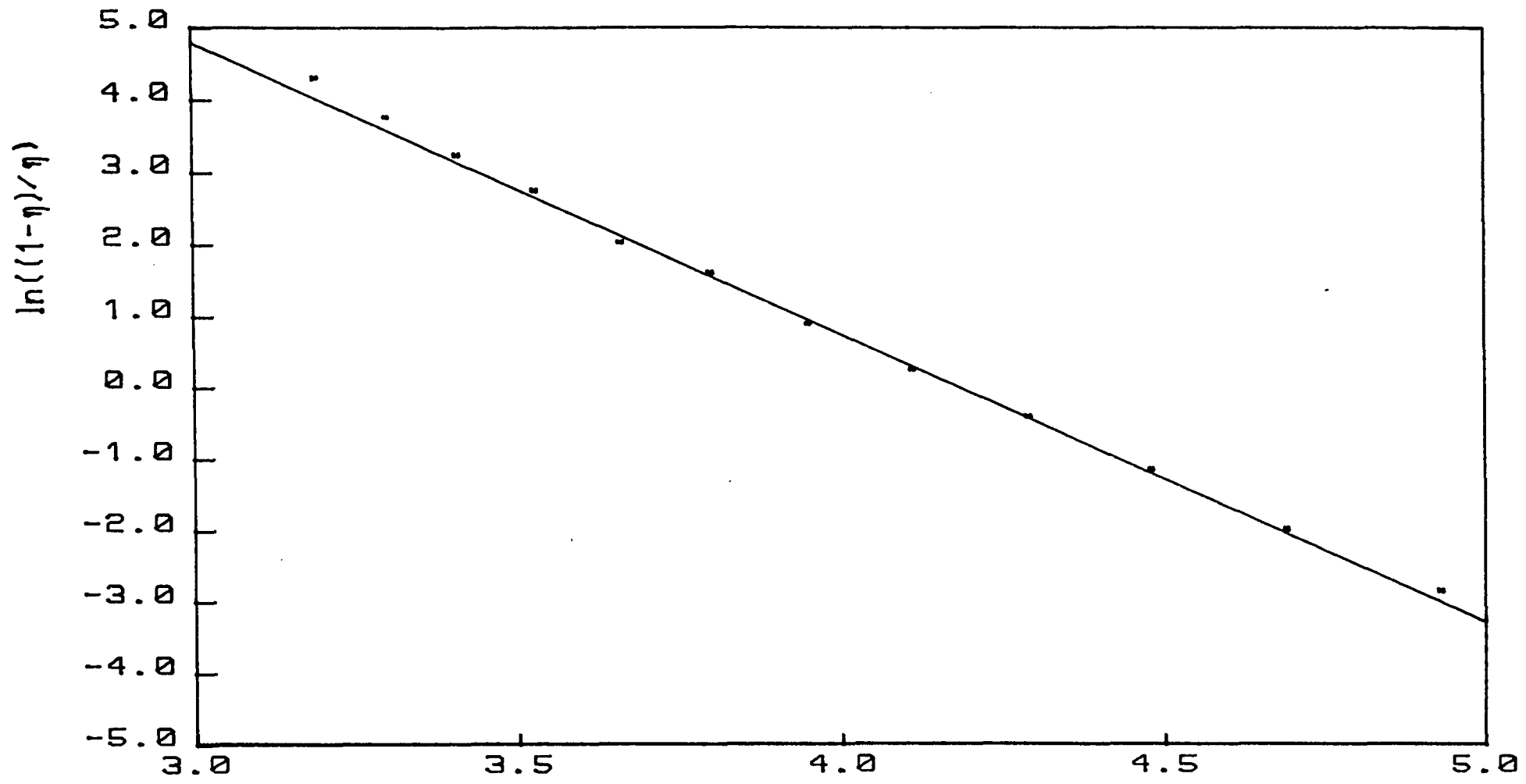


Figure 5.3.4 Activation energy plot for thermal quenching of photoluminescence $1000K/T$
 TI sample

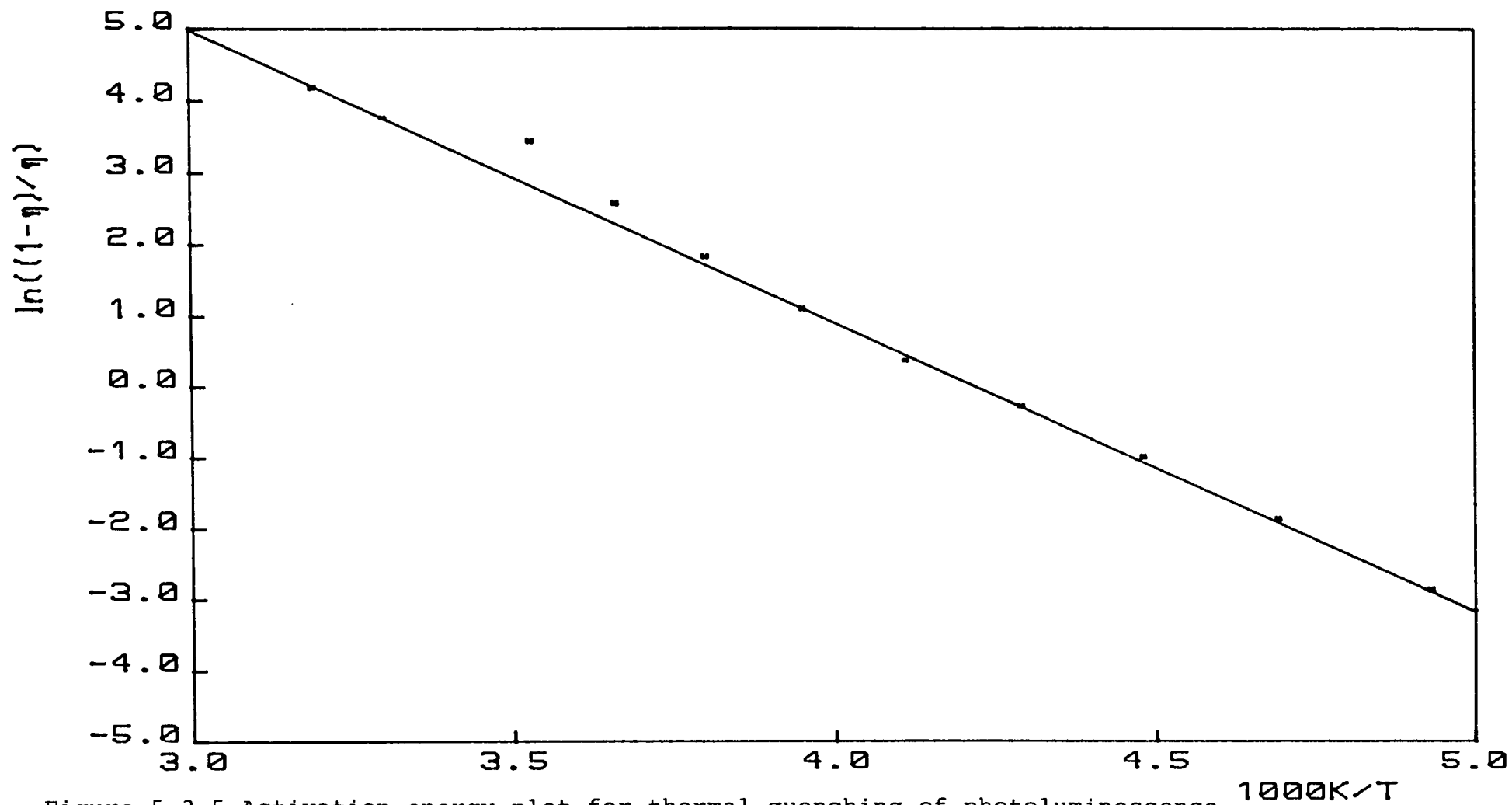


Figure 5.3.5 Activation energy plot for thermal quenching of photoluminescence
 NL sample

proposed for the two effects.

If the lifetime of the radiative transition is constant at temperatures less than 150 K, implying that there is insufficient energy for thermal excitation from the excited state of the luminescence centre, it may be expected that the luminescence intensity would also be constant for these temperatures. However, as may be seen from figures 5.3.1 and 5.3.2 the luminescence intensity increases to a maximum at 190 K. This implies that there is another competitive process involved.

One competitor of radiative transitions is the Auger effect in which a second electron absorbs the energy given up by the first electron as it recombines. A possible explanation for the reduction in luminescence efficiency at low temperatures is that the energy released by the recombination transition is used to excite an electron from a shallow trap to the conduction band. As the temperature increases the population of shallow traps decreases, as the electrons are thermally excited, and this method becomes less competitive.

5.4 THERMALLY STIMULATED LUMINESCENCE AND CONDUCTIVITY

Thermally stimulated luminescence (TSL) experiments were carried out on the TI and NL single crystal samples that were used for the photoluminescence experiments described above.

In a typical set of experiments on a sample the TSL was measured for six or more heater currents between 0.5 and 2.3 A. These heater currents gave heating rates of 0.1 to 0.6 Ks⁻¹. The heater current was not varied during a heating cycle, but the non-linearity in heating rate that this caused was small over the temperature spread of a TSL peak. The variation in heating rate caused the peaks in the TSL spectrum to occur at different temperatures and with different heights. These changes could be used to determine an activation energy for the trap associated with each peak.

A typical TSL spectrum from an undoped TI sample is shown in figure 5.4.1.

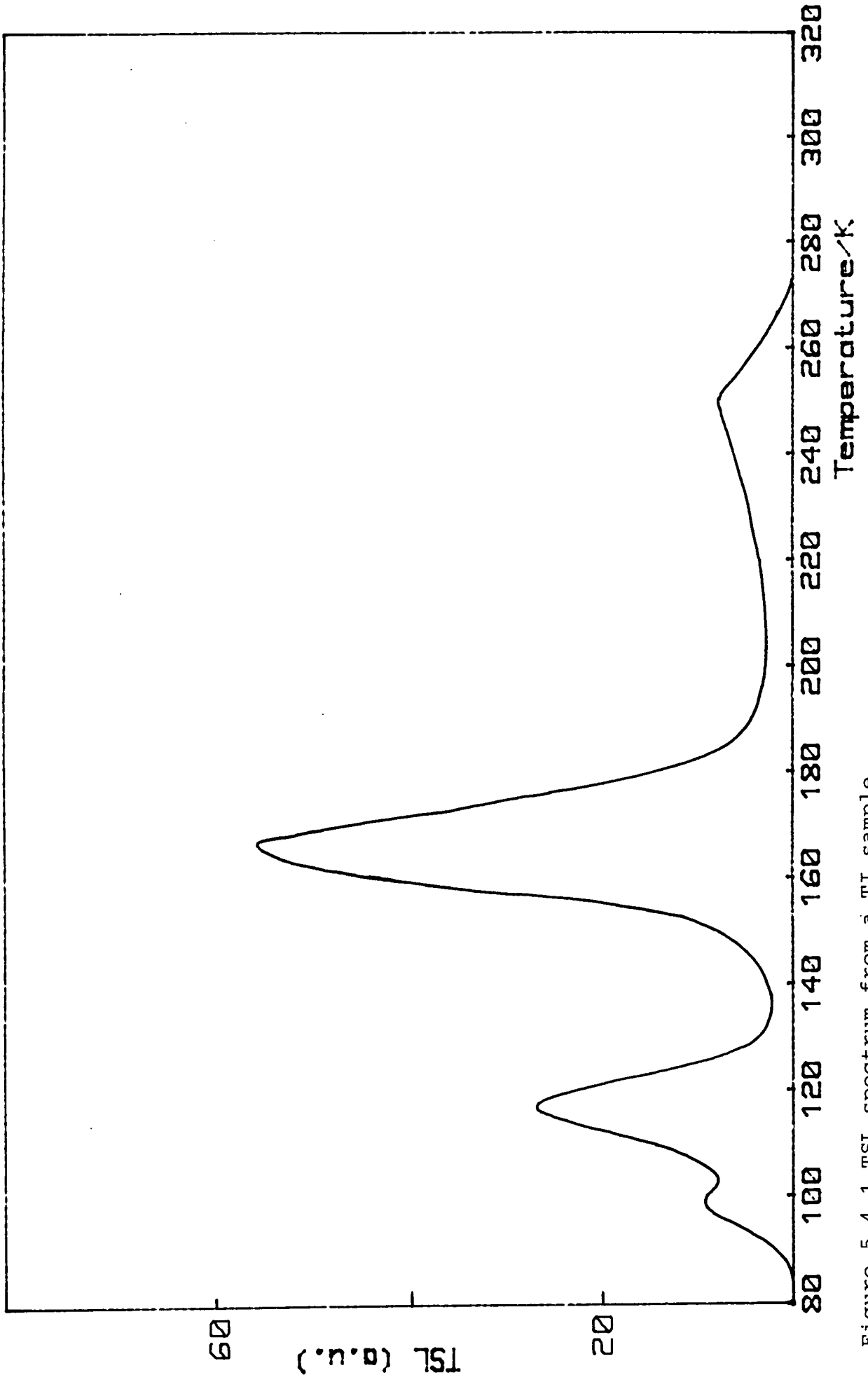


Figure 5.4.1 TSL spectrum from a TI sample

Since the peak position is dependent on heating rate, the results shown in this and subsequent chapters were all obtained with the same heater current to aid comparisons between different samples. Four peaks are apparent in the TSL spectrum, occurring at 100, 116, 166 and 248 K. The thermoluminescence intensity does not drop to zero between the the peaks at 166 and 248 K so there may be some other peak or peaks in that region that are unresolved. A TSL spectrum from a NL sample is shown in figure 5.4.2 (note the changes in vertical scale at 135 and 220 K). This spectrum has peaks at 102, 120, 166, 243, and 284 K. It can be seen that there is good agreement between the temperatures of the first four peaks between the samples from the two sources, but the relative intensities are different. This suggests that the same traps are present in the two samples but in different concentrations. Such a variation in concentration could be caused by differing amounts of unintentional impurities or of defects created during the different growth methods of the samples. The spectrum from the NL sample shows a peak at 284 K that is not seen in the spectrum from the TI sample. Again, as for the TI sample, the TSL intensity does not drop to zero between the 166 and 243 K peaks.

Hillhouse and Woods [149] have shown that the simple trap model applies particularly well to rutile and that the analysis methods of Hoogenstraaten [109], Haering and Adams [117], Chen and Winer [116], Unger [58] and Garlick and Gibson [73] gave consistent values for trap depth. Of these methods, those of Hoogenstraaten, Haering and Adams and Unger are commended by Kivits and Hagebeuk [75] in their review of the many analysis methods. The method of Chen and Winer is only accurate for slow retrapping and the method of Garlick and Gibson has to be applied in the first part of the initial rise of the peak which can make it difficult to apply in practice. The methods of Hoogenstraaten, Haering and Adams and Unger have, therefore, been adopted to analyse the peaks in the spectra. Hoogenstraaten's method uses the variation in peak temperature with heating rate, whereas the methods of Haering and Adams and Unger use the variation in peak height with heating rate.

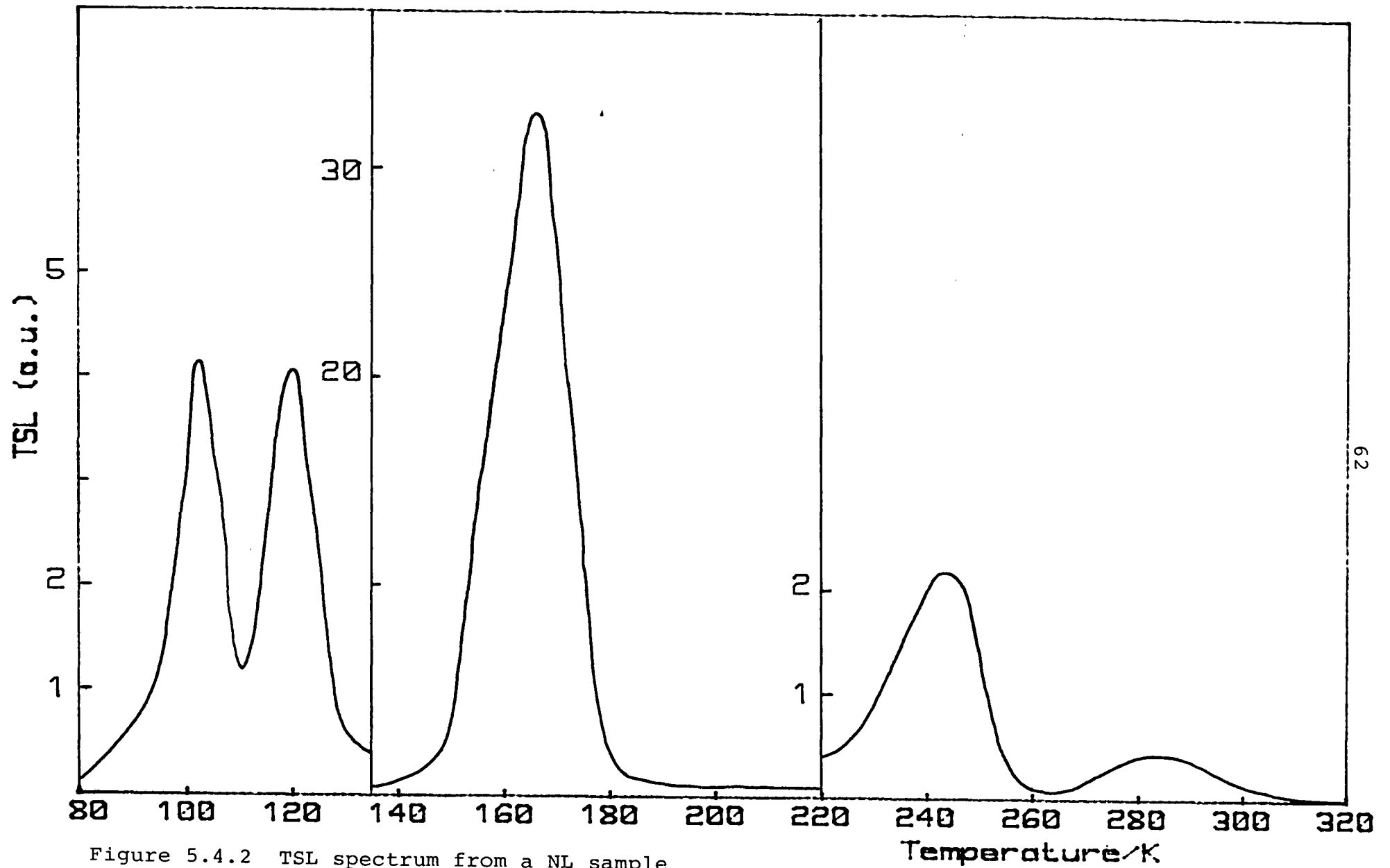


Figure 5.4.2 TSL spectrum from a NL sample

The trap depths determined from the analysis of the TSL curves are shown in table 5.4.1. It is quite evident that the three methods give consistent values for the trap depths. It was not possible to determine a trap depth for the 248 K peak because at lower heating rates the peak could not be resolved adequately. The same values of trap depth were obtained from both the the TI and NL samples for the four peaks that were seen in the spectra from both samples. Hoogenstraaten's method also allows capture cross sections to be determined. The values obtained are also given in table 5.4.1.

Thermally stimulated conductivity measurements were also carried out on these samples by applying a bias across the sample and monitoring the current passing as the sample was heated rather than recording the luminescence. A similar spread of heating rates was used to give variations of peak temperature and amplitude.

A typical TSC curve for a TI sample is shown in figure 5.4.3 (note the change in vertical scale at 140 K). Five peaks are apparent in the TSC spectrum, which also shows an appreciable dark current above 200 K. Three of the peaks are distinct and occur at 97, 116 and 176 K; the two remaining peaks occur at about 240 and 270 K but are partly obscured by the dark current. The four lowest temperature peaks correspond to those seen in the TSL spectra, although the peak temperatures are not identical. Fields and Moran [150] have shown that, in general, the peaks of TSC and TSL spectra do not occur at the same temperature.

Repeating the TSC experiment without exciting the sample yielded the dark conductivity alone. In general, above a certain temperature the TSC spectrum and the dark conductivity coincided but for lower temperatures the TSC was greater. An Arrhenius plot of the dark conductivity is shown in figure 5.4.4, as is the full TSC curve. The slope of the straight line can be interpreted as the Fermi energy or other dominant level. In this case the slope yields a value of 0.71 eV. In this instance the dark conductivity and the TSC spectrum coincided above 400 K. The conductivity of the sample appears, therefore, to be the sum of a contribution from trap emptying and a separate contribution from the dark conductivity. Subtracting the dark

Activation energies and capture
cross-sections for undoped rutile

	Peak Temperature			
	103	120	166	242
Hoogenstraaten	0.14	0.23	0.36	0.68
Haering and Adams	0.14	0.24	0.37	0.68
Unger	0.13	0.24	0.37	0.67
Cross-section	10^{-20}	10^{-18}	10^{-17}	10^{-18}

Trap depths in eV Error ± 0.02 eV
Cross-sections in cm^2

Table 5.4.1

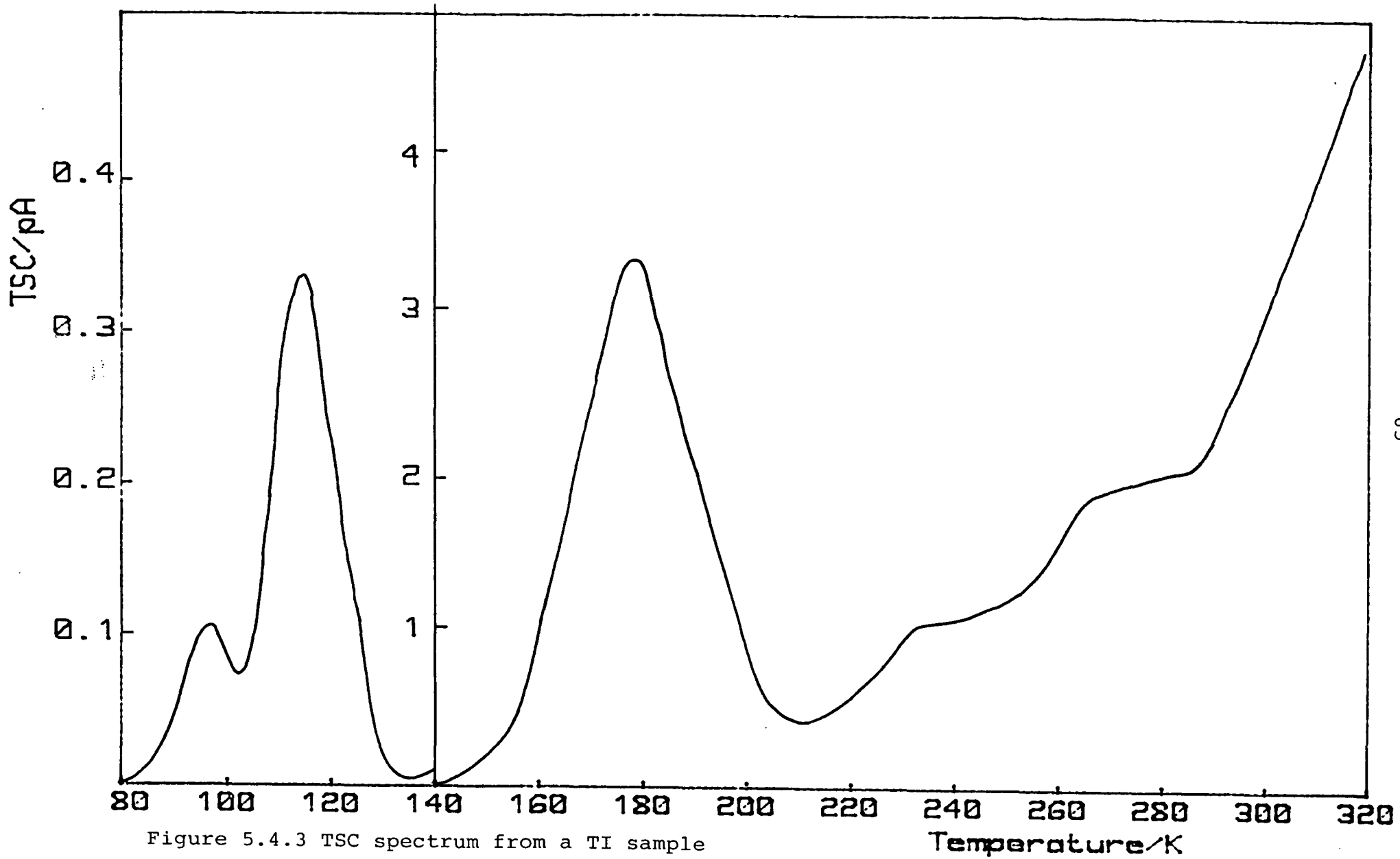


Figure 5.4.3 TSC spectrum from a TI sample

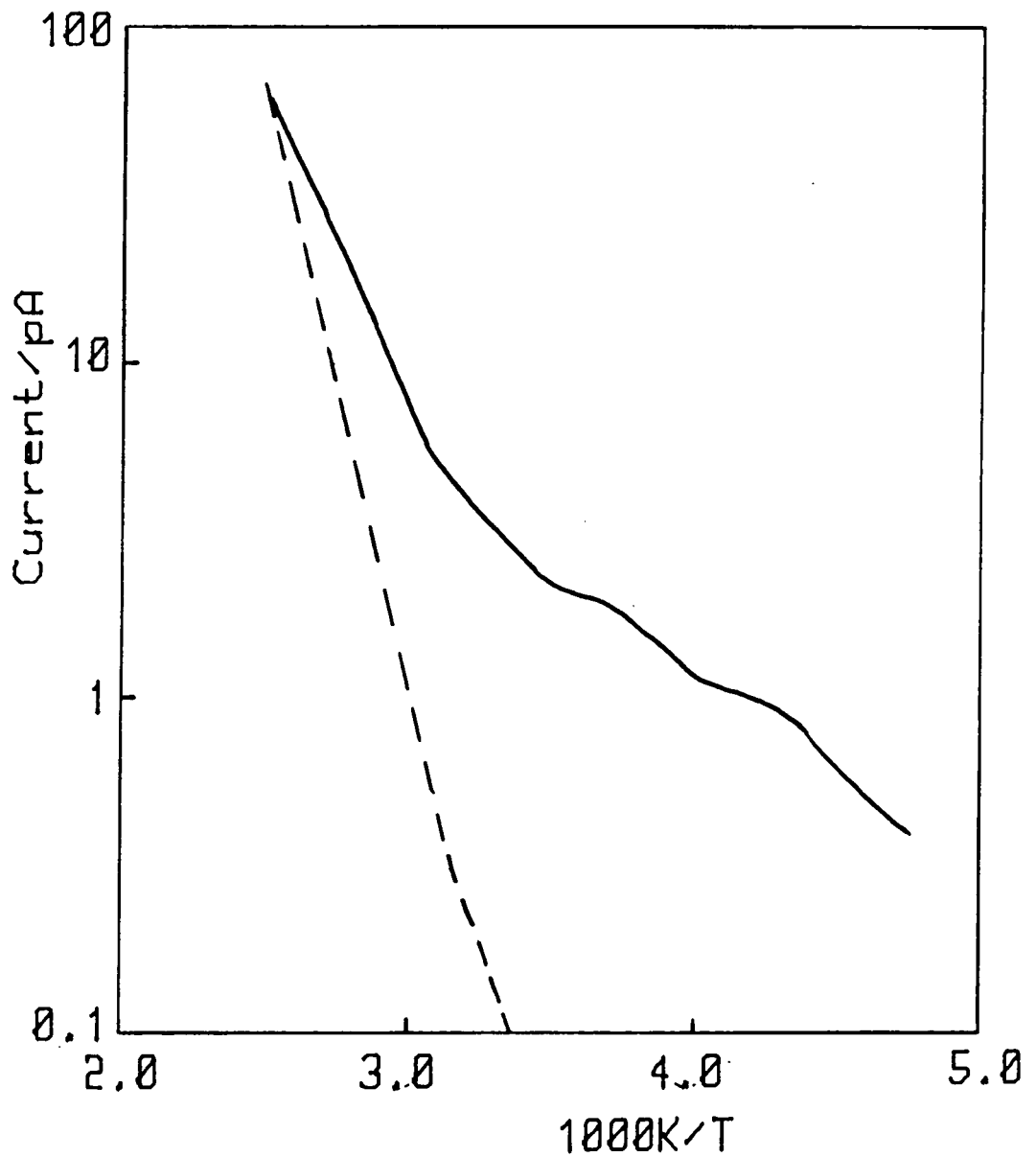


Figure 5.4.4 Arrhenius plot of TSC spectrum and dark current for TI sample

conductivity from the total TSC spectrum yields a curve such as that shown in figure 5.4.5. It can be seen that there is a peak at about 380 K with a shoulder at about 310 K.

Figure 5.4.6 shows the TSC trace obtained from a NL sample. The dark conductivity dominates and the conductivity has been plotted on a logarithmic scale. Peaks in the conductivity can be seen at about 120, 160, 222 and 260 K. The dark conductivity grows rapidly above 260 K. In this case the dark conductivity accounts for all the conductivity above 270 K. Figure 5.4.6 also shows the trace corrected to allow for the dark conductivity. An Arrhenius plot for the dark conductivity is shown in figure 5.4.7. This yields a value of 0.58 eV for the dominant level. The difference in activation energy of the dark current between the TI and NL samples could be related to the absence of TSC peaks above 270 K for the NL sample.

It is interesting to note that there seems to be no increase in TSL corresponding to the increase in dark conductivity. The simple model for TSL and TSC involves transitions from the trap to the recombination centre via the conduction band. While in the conduction band electrons can contribute to the conductivity and correlation between TSL and TSC peaks would be expected. It seems that the electrons giving rise to the dark conductivity do not make luminescent transitions. One possible explanation comes from the thermal quenching of the luminescence observed in section 5.3.2. It may be that, at the temperatures where the dark conductivity is becoming dominant, the luminescence efficiency is too low for luminescence to be observed. Alternatively, Becker and Hosler [31] have suggested multiple band conduction as an explanation for anisotropic Hall coefficient data in n-type rutile. In their model, at temperatures below 40 K, conduction takes place mainly in the lower band. At higher temperatures excitation of electrons takes place from the lower band to an upper band about 0.06 eV higher. If the transition from this upper band to the luminescence centre is unlikely, then the increased population in the upper band would not lead to an increase in luminescence. An increase in dark conductivity would not then be accompanied by an increase in luminescence.

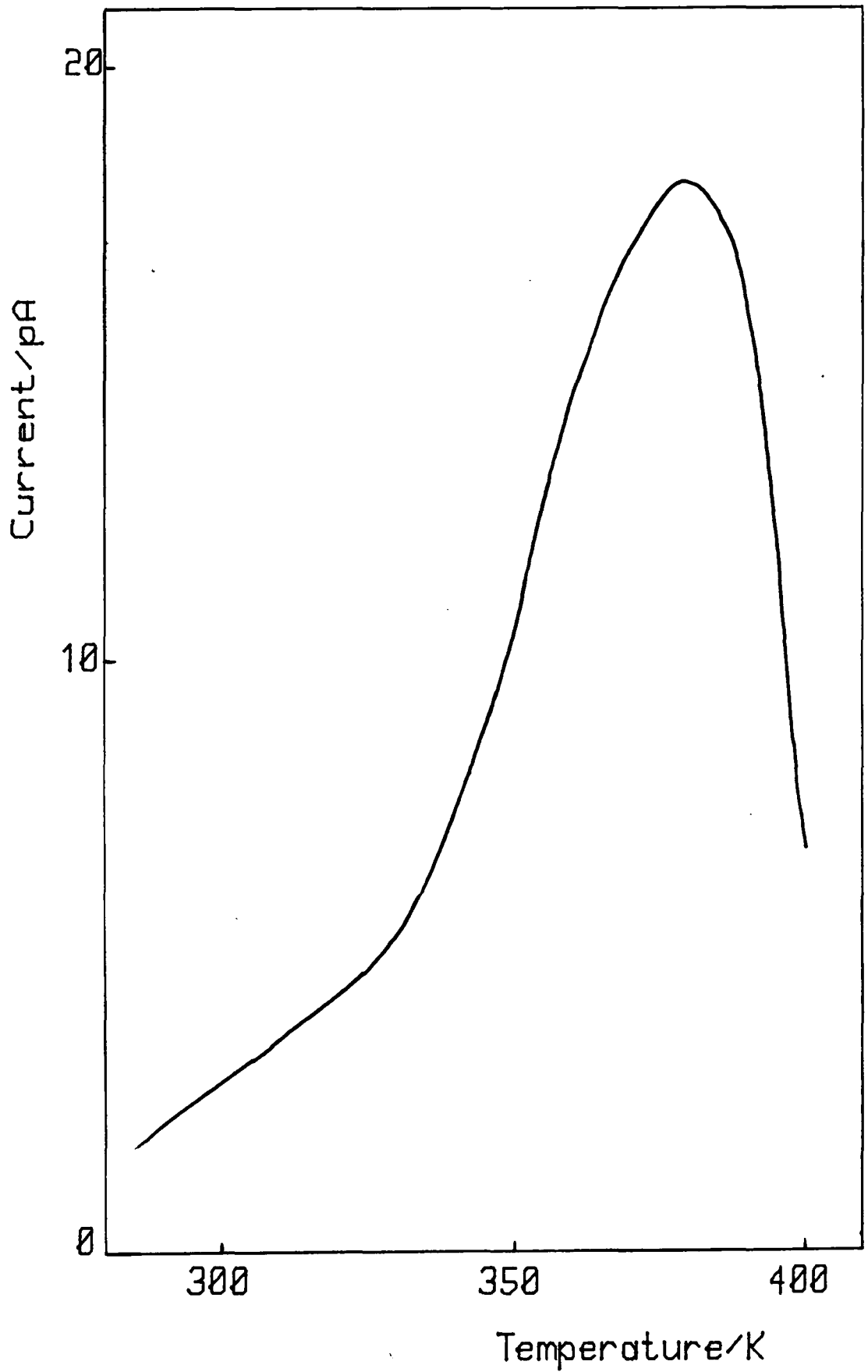


Figure 5.4.5 Excess TSC over dark current for TI sample

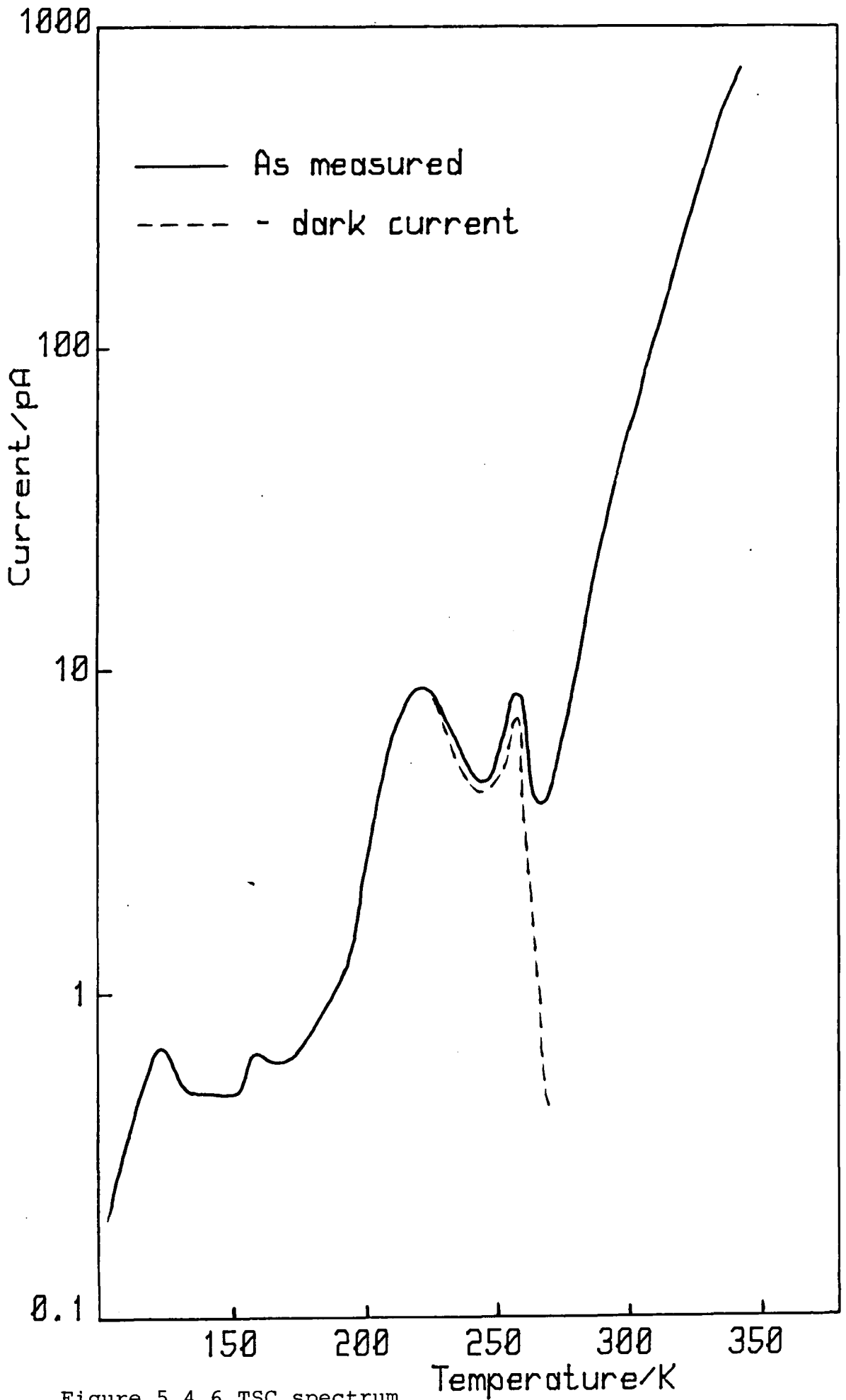


Figure 5.4.6 TSC spectrum
from NL sample

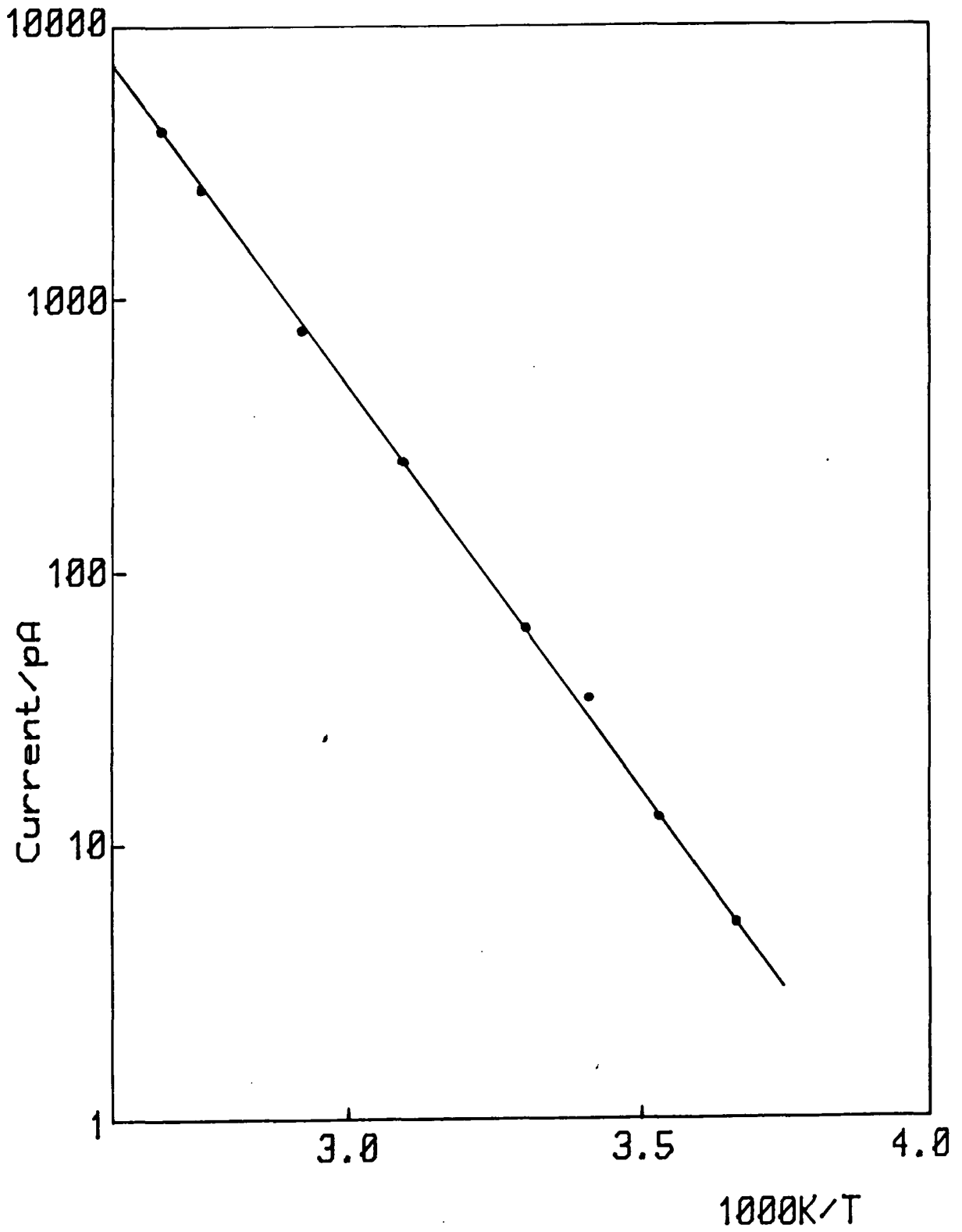


Figure 5.4.7 Arrhenius plot of dark current for NL sample

TSL and TSC spectra for undoped single crystal rutile have been reported by Hillhouse [10], Hillhouse and Woods [142,149] and Ghosh et al [146]. A comparison between the results described above and those from the other workers is shown in table 5.4.2. It can be seen that there is very close agreement in both peak temperature and activation energy between the results from the present work and those reported by Hillhouse, apart from the peak at about 240 K. However, the capture cross-sections are all between 10 and 100 times larger than those determined by Hillhouse. The peak temperatures agree with those found by Ghosh et al but the activation energies are different. Ghosh et al used the quasi Fermi level method advocated by Bube [70] to determine the activation energies. This method is only valid under conditions of fast retrapping but Hillhouse and Woods have shown that the recombination kinetics for rutile are intermediate between slow and fast. Both Ghosh et al [146] and Lauer et al [151] have reported TSC spectra from a trap at 310 K which is the temperature where a shoulder is seen on the excess of TSC over dark conductivity trace shown in figure 5.4.5.

5.5 REDUCED RUTILE

5.5.1 Introduction

Past studies of electronic levels deep in the band gap of rutile have been limited to the methods of thermally stimulated luminescence and conductivity etc., because of the large band gap. Normally rutile is too resistive for techniques such as DLTS to be considered.

However rutile is changed from an insulator to an n-type semiconductor by reduction, because point defects due to the reduction act as donor centres [152,153]. Iguchi and Yajima [154] concluded that it is reasonable to consider oxygen vacancies as the dominant point defects in reduced rutile. Szydlo and Poirier [143] have recently reported I-V and C-V characteristics of gold / n-type rutile Schottky diodes

Comparison of trap parameters

This work			Hillhouse			Ghosh et al	
Peak	E_T	σ	Peak	E_T	σ	Peak	E_T
						93	0.27
103	0.14	10^{-20}	100	0.14	10^{-21}	103	0.28
120	0.23	10^{-18}	118	0.24	10^{-19}	123	0.32
166	0.37	10^{-17}	169	0.37	10^{-19}	168	0.48
						198	0.56
242	0.68	10^{-18}	239	0.51	10^{-19}	243	0.62
284	✓		296	0.61	10^{-19}	298	0.76
			328	0.69	10^{-19}	313	0.87

Trap depths (E_T) in eV

Cross-sections (σ) in cm^2

Table 5.4.2

using reduced rutile crystals. Bogoroditskii et al [39] have shown that niobium doping also makes rutile semiconducting.

The DLTS technique described in chapter 3 requires a voltage dependent depletion region. Reduced rutile and niobium doped single crystals with gold Schottky barriers were investigated in an attempt to obtain DLTS spectra. The experimental technique has been described in chapter 4. Results from experiments on reduced but otherwise undoped single crystal rutile are given below; results from niobium doped crystals are given in chapter 11.

5.5.2 Capacitance-voltage measurements

The capacitance of the gold / reduced rutile Schottky diode was measured as a function of reverse bias and the result is shown in figure 5.5.1 as a plot of C^{-2} versus V . The slope of the line enables the ionised donor density to be calculated and this yields a value of $1.3 \times 10^{15} \text{ cm}^{-3}$. Taking a value of $1.0 \text{ cm}^2 \text{ V}^{-1} \text{ s}^{-1}$ for the mobility parallel to the c-axis this indicates a resistivity of about $4.8 \times 10^3 \text{ } \Omega \text{ cm}$. The intercept of the line on the V -axis yields a value of 0.3 V for the built-in voltage of the diode.

5.5.3 Current-voltage measurements

Szydlo and Poirier [143] have described diodes with high ideality factors. Figure 5.5.2 shows a typical current versus voltage curve for a sample from the present work. It can be seen that the observed characteristics are far from ideal. The current-voltage curves are shown plotted on logarithmic axes in figure 5.5.3. From this it can be seen that when the diode is reversed biased the current is ohmic up to an applied bias of 1 V after which the current increases rapidly. When forward biased the current is ohmic up to an applied bias of 0.5 V when the current increases rapidly with applied voltage. Such current-voltage characteristics are typical of

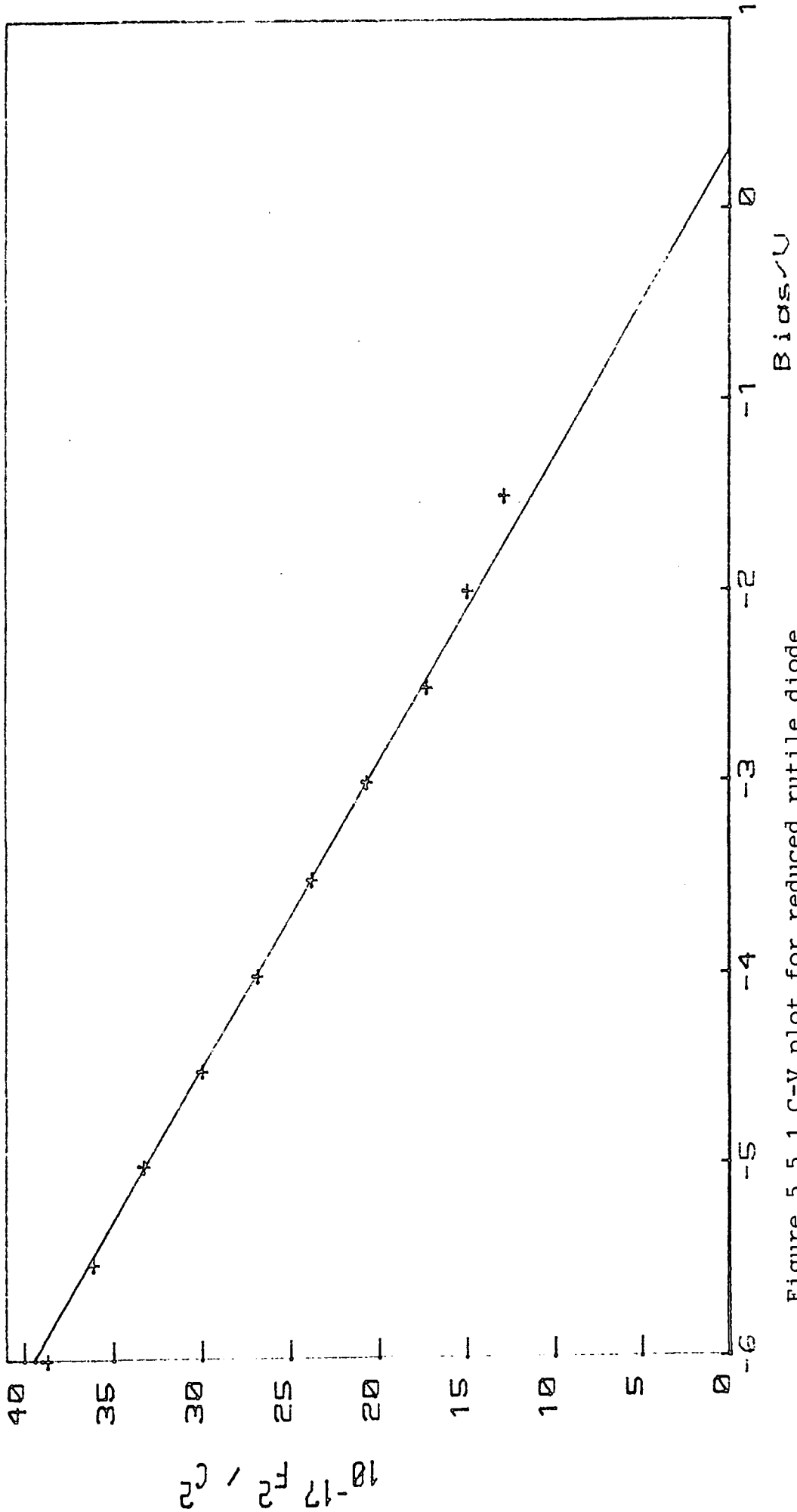


Figure 5.5.1 C-V plot for reduced rutile diode

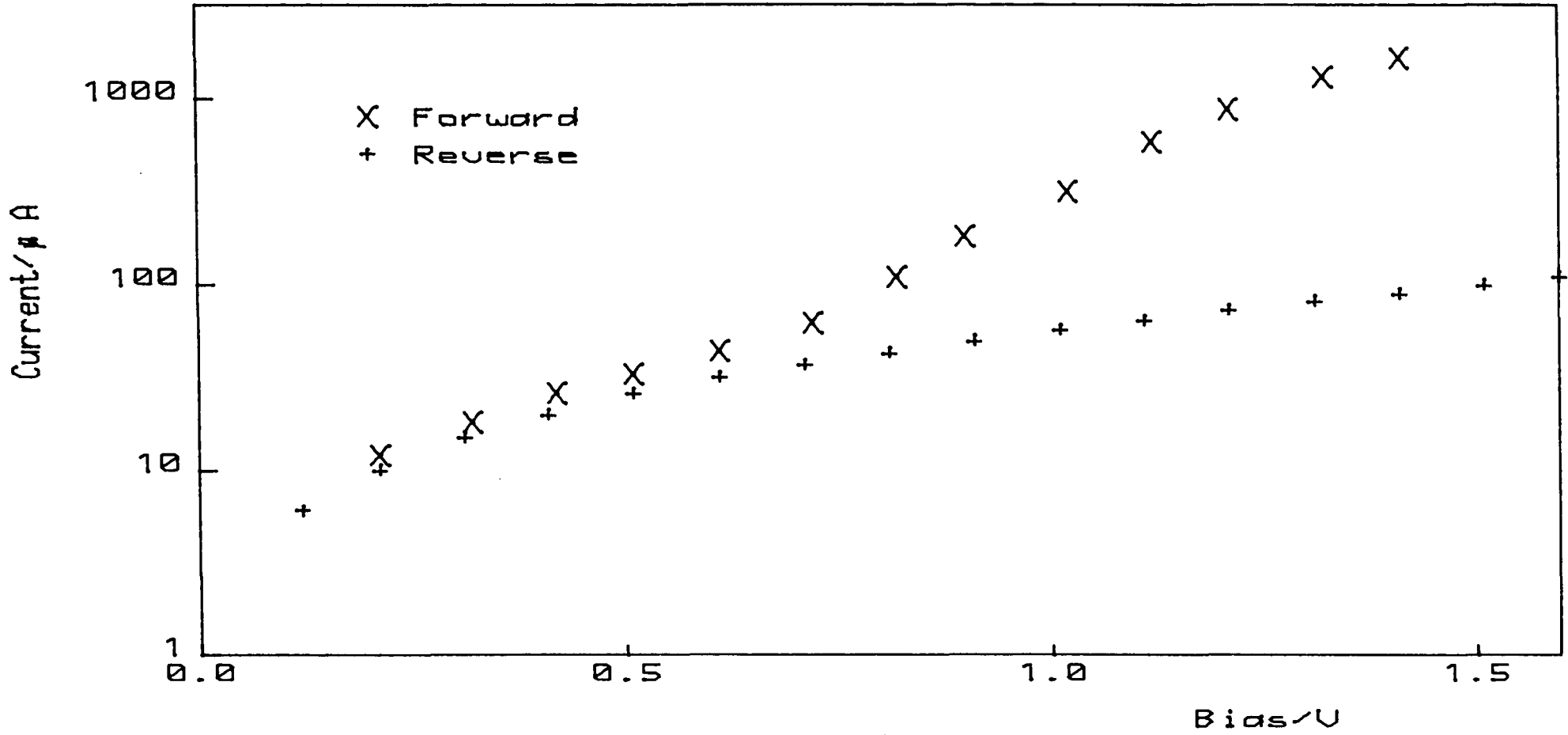


Figure 5.5.2 I-V characteristics for reduced rutile diode

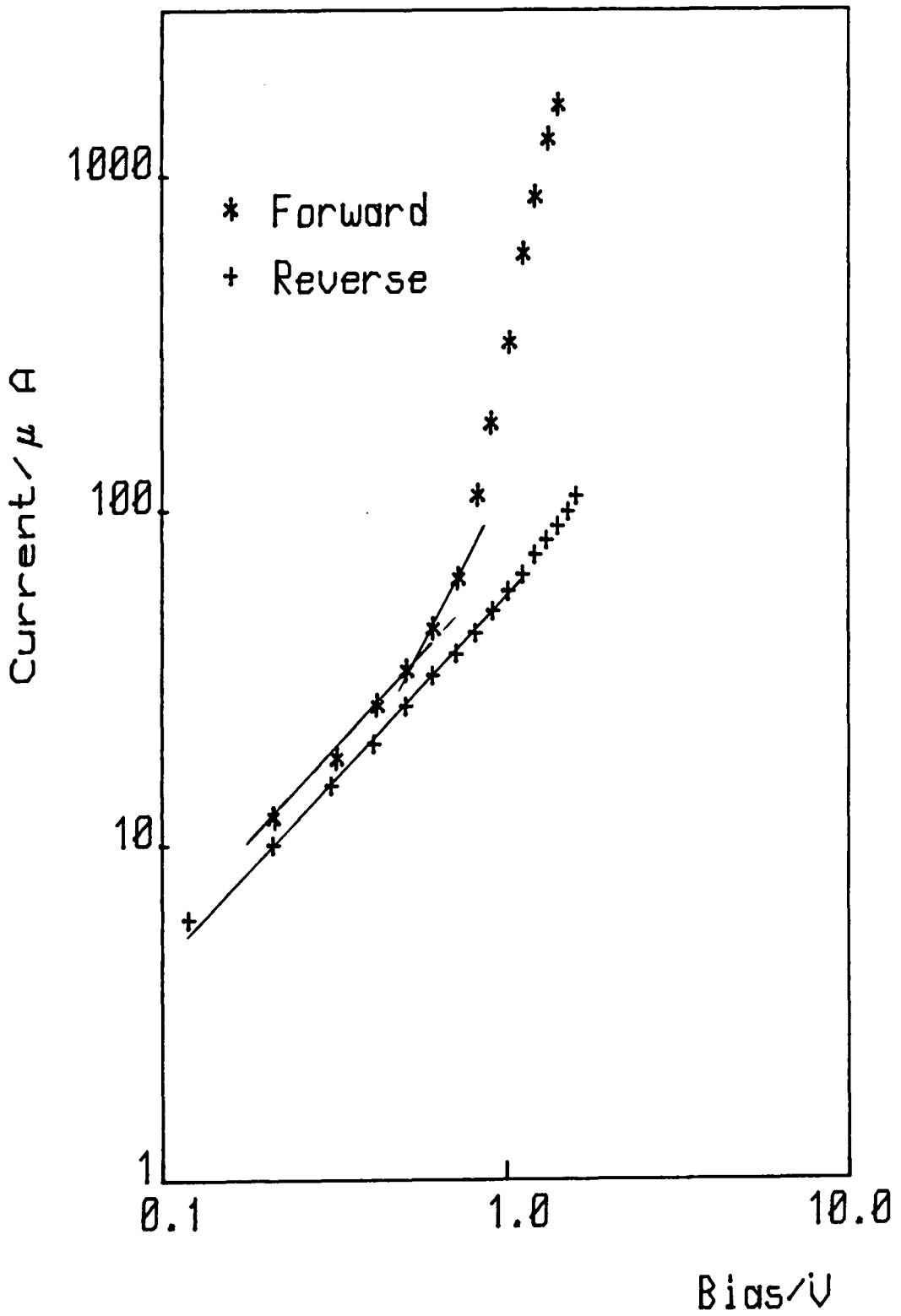


Figure 5.5.3 I-V characteristics for reduced rutile diode

space charge limited currents (SCLC) and have been observed in many materials [155]. However, most SCLC data from solids previously reported have been obtained from films with thicknesses typically less than 10 μm . In the present work the inter electrode spacing was 250 μm .

It may not always be clear whether a superlinear I-V characteristic can be attributed to a bulk SCLC mechanism. Abkowitz and Scharfe [156], for example, interpret superlinear I-V characteristics in gold - a-As₂Se₃ sandwich cells for fields greater than 10⁴ Vcm⁻¹ as being limited by the emission kinetics of the contact rather than trapped space charge.

Greener and Whitmore [157] have observed superlinear I-V characteristics in high temperature measurements on near-stoichiometric rutile. Mott and Gurney [82] provided an approximate expression relating the current, voltage and thickness in a trap free insulator; other more refined treatments are available [62,158]. A slight modification to the Mott and Gurney treatment by Roberts et al [159] results in the following relationship between current density, voltage and thickness for a SCL current:

$$J = 9\theta\epsilon_r\epsilon_0\mu V^2/(8W^3) \quad (5.1)$$

In this equation μ is the mobility, ϵ_r is relative permittivity, W is the thickness and θ is the fraction of total carriers (all electrons above the Fermi level) that are free. The introduction of deep trapping centres in the crystal can result in a higher power dependence of current than the square law relation shown above [159]. As more and more electrons are injected into the solid, the traps gradually fill up and eventually no further charge can be trapped. Such square law and higher power relationships can be seen for the forward biased curves in figure 5.5.3. Inputting values from this curve to equation (5.1) yields a value for the $\mu\theta\epsilon_r$ product of $6 \times 10^5 \text{ cm}^2 \text{V}^{-1} \text{s}^{-1}$. Taking a value of 170 for the room temperature dielectric constant [160] would lead to a minimum value of $3.5 \times 10^3 \text{ cm}^2 \text{V}^{-1} \text{s}^{-1}$ for the mobility which is considerably higher than is usually found for rutile (section 2.5). Greener and Whitmore [157] who measured

superlinear I-V characteristics at high temperatures found that even higher mobility values would be needed. One explanation that they propose is that conduction may occur in high energy bands where higher mobilities may be possible. This mechanism has also been suggested to account for the lack of increased luminescence accompanying increased dark conductivity.

5.5.4 Deep level transient spectroscopy

DLTS measurements were made on the gold - reduced rutile Schottky diodes for temperatures between 77 and 300 K. No structure was seen in the DLTS spectra, although the undoped rutile crystals had shown, before reduction, the existence of traps which were thermally activated in this temperature range.

5.6 SUMMARY

Samples of undoped rutile have been studied by the methods of photoluminescence, thermoluminescence and thermally stimulated conductivity. Schottky barriers made on undoped, but reduced, samples have been also been studied.

Photoluminescence experiments showed that the luminescence from rutile was a broad band centered on 850 nm as observed by previous workers. The temperature dependence of the luminescence showed a sharp drop above 190 K which was explained by thermal quenching. An activation energy of 0.35 eV for this quenching transition was determined which was different from the 0.18 eV obtained by Ghosh et al from lifetime measurements. An Auger mechanism has been proposed to account for a reduction in luminescence efficiency at low temperatures.

Thermoluminescence and thermally stimulated conductivity experiments showed the presence of up to six traps appearing in the range of temperatures studied from 80 to 400 K. A technique of subtracting the dark conductivity from the total conductivity trace was used to isolate higher temperature traps. Activation energies

determined for the lower temperature traps agreed with those reported by Hillhouse but were different from those reported by Ghosh et al. Capture cross-sections were larger than those reported by Hillhouse.

DLTS experiments on reduced undoped samples proved unsuccessful but current-voltage measurements on these samples showed space charge limited conduction characteristics implying a high mobility. Multiple band conduction was suggested as a possible explanation.

CHAPTER 6

CHROMIUM DOPED CRYSTALS

- 6.1 Introduction**
- 6.2 Material preparation**
- 6.3 Photoluminescence**
- 6.4 Thermally stimulated luminescence and conductivity**
- 6.5 Summary**

6.1 INTRODUCTION

The studies of the properties of undoped rutile crystals described in the previous chapter were extended to cover some of the dopants usually found in nominally undoped crystals and as impurities in rutile pigments. In particular, chromium and iron are known to affect the durability of rutile based paint films [5]. The effects of doping with the transition metals manganese, cobalt and nickel were also studied. The results of experiments on chromium doped samples are discussed in this chapter; the results from the other dopants are in subsequent chapters.

Grabner et al [147] attributed the emission in rutile at 850 nm to substitutional chromium (Cr^{3+}) ions present as unintentional impurities in the lattice. As discussed later in this chapter, chromium doping led to an increase in both photoluminescence and thermoluminescence intensity. The techniques for analysing thermoluminescence spectra have, therefore, been illustrated in this chapter.

6.2 MATERIAL PREPARATION

The dopant was diffused into the rutile crystal by heating the crystal and some chromium wire together in an evacuated quartz ampoule. After evacuation the ampoule was sealed and heated in a furnace for 24 hours at 1050°C. Following this treatment the rutile was doped but also reduced. Stoichiometry was restored by annealing in an oxygen flow for 24 hours at 1000°C.

The sample was then cleaned and mounted in the manner described in chapter 4.

6.3 PHOTOLUMINESCENCE

Emission spectra from chromium doped samples showed the same structure, with a broad band centred on about 860 nm and a shoulder at about 820 nm as was observed from undoped samples. The photoluminescence intensity from chromium

doped samples was higher by a factor of about 10 than from undoped samples which supports the conclusion of Grabner et al [147] that Cr^{3+} is the radiative centre in rutile.

The temperature dependence of the photoluminescence emission intensity under constant illumination was measured and the result is shown in figure 6.3.1. This shows the same behaviour as was observed from undoped samples with the luminescence intensity increasing slightly up to 190 K and then decreasing rapidly with a further increase in temperature. A plot of $\ln[(1-\eta)/\eta]$ against reciprocal temperature is shown in figure 6.3.2. The slope gives an activation energy of 0.35 eV, in agreement with that found for undoped crystals. Hillhouse [10] reports a change in slope of such a plot with an activation energy of 0.22 eV below 200 K and 0.34 eV above that temperature. In the present case, the decrease in luminescence begins at 190 K and thus no evidence for a different activation energy below 200 K was seen. There is, however, close agreement between the activation energies obtained above 200 K.

6.4 THERMALLY STIMULATED LUMINESCENCE AND CONDUCTIVITY

TSL and TSC experiments were carried out on the chromium doped samples studied in the photoluminescence experiments described above.

A typical TSL spectrum from a chromium doped crystal is shown in figure 6.4.1. Four peaks are apparent in the spectrum, occurring at 118, 165, 197 and 220 K. The peak at 118 K is separate from the higher temperature peaks and is, therefore, 'thermally disconnected', but the other peaks overlap. The technique of thermal cleaning [56] was used to remove the lower temperature peaks in succession so that the higher temperature peaks could be analysed. The main peak was removed by heating the sample to 165 K and then cooling quickly. The trace obtained during subsequent heating is shown in figure 6.4.2. The next peak was removed by heating to 200 K and then cooling. The trace showing the last peak is shown in figure 6.4.3.

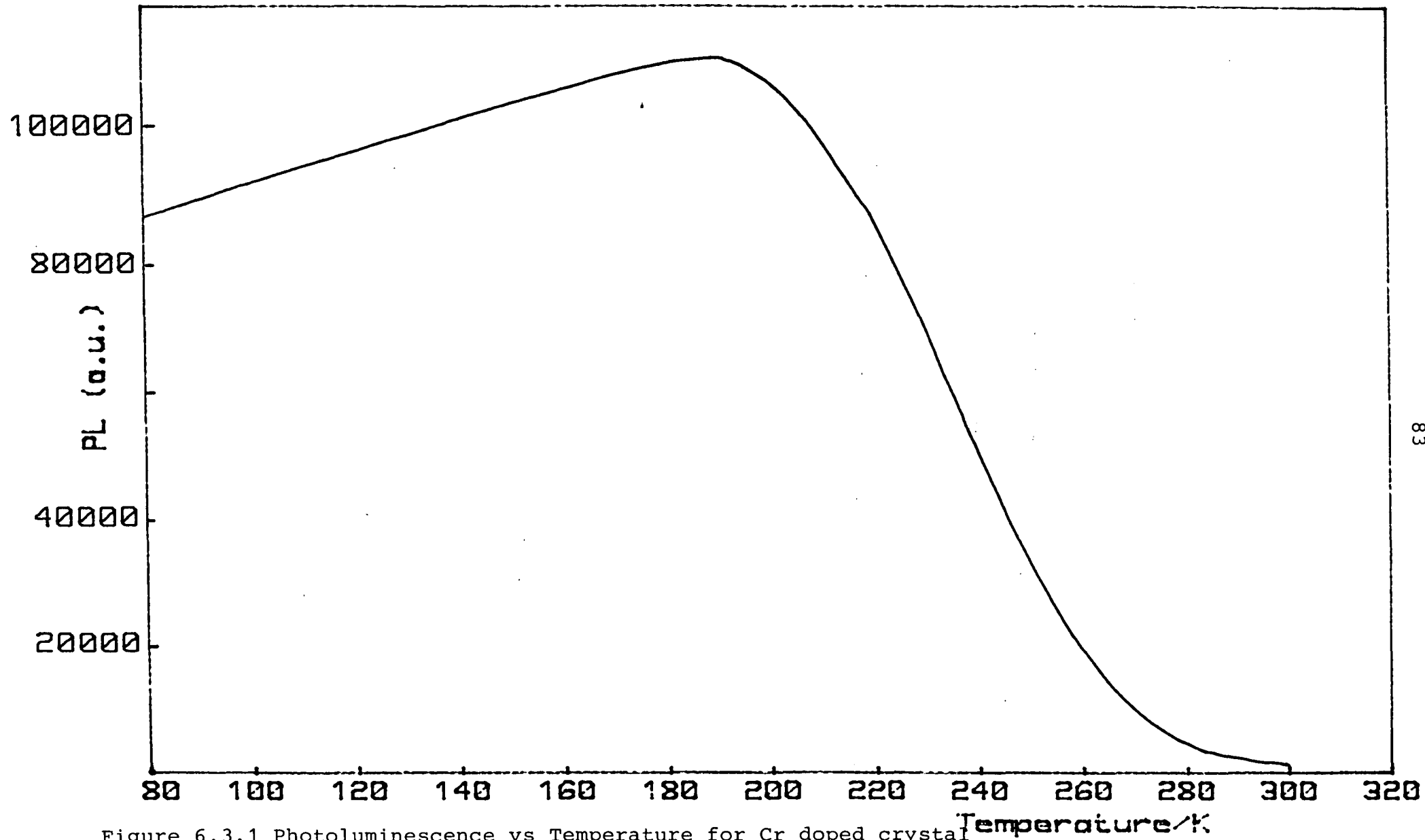


Figure 6.3.1 Photoluminescence vs Temperature for Cr doped crystal

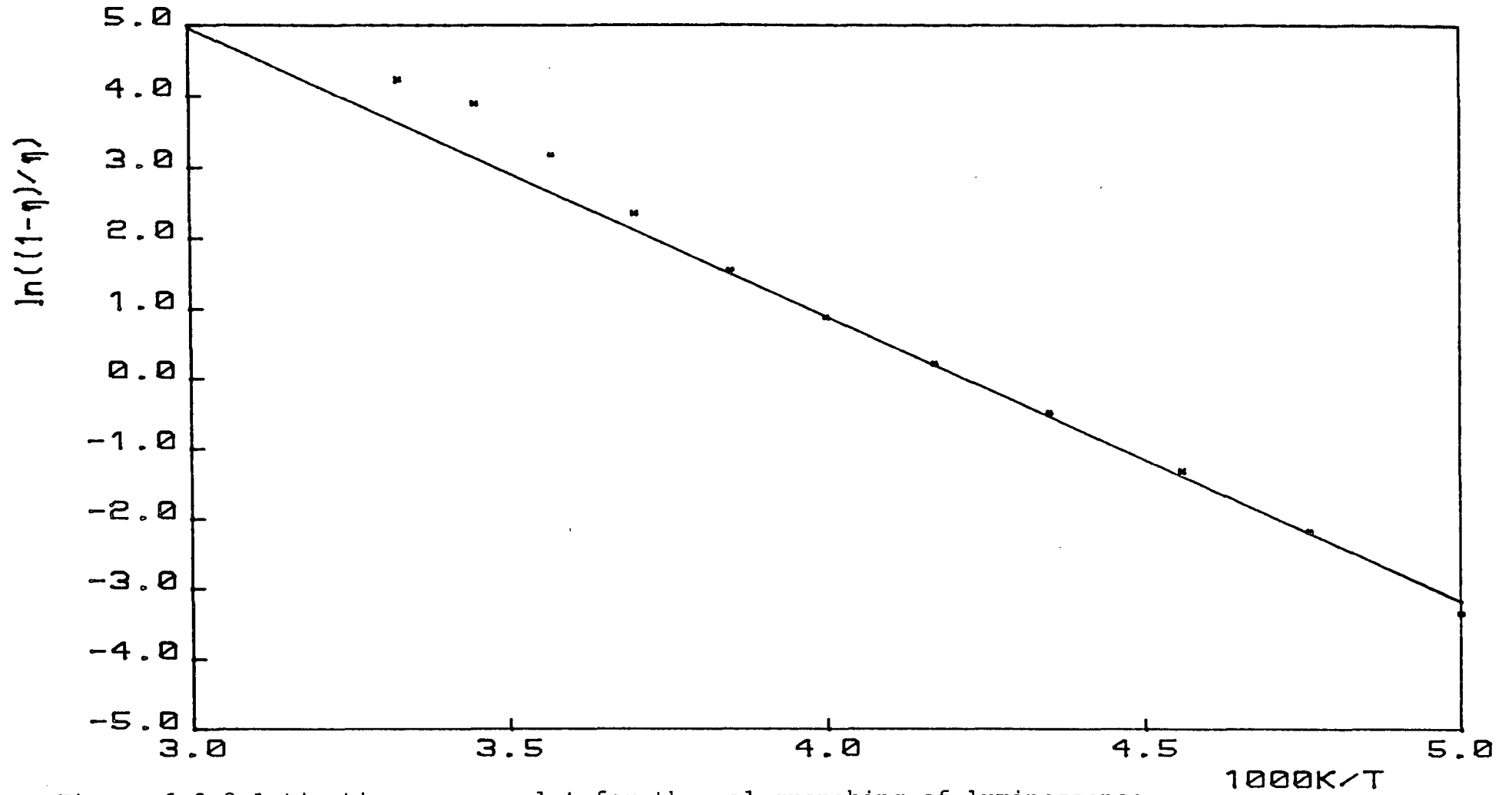


Figure 6.3.2 Activation energy plot for thermal quenching of luminescence
 $\text{TiO}_2:\text{Cr}$

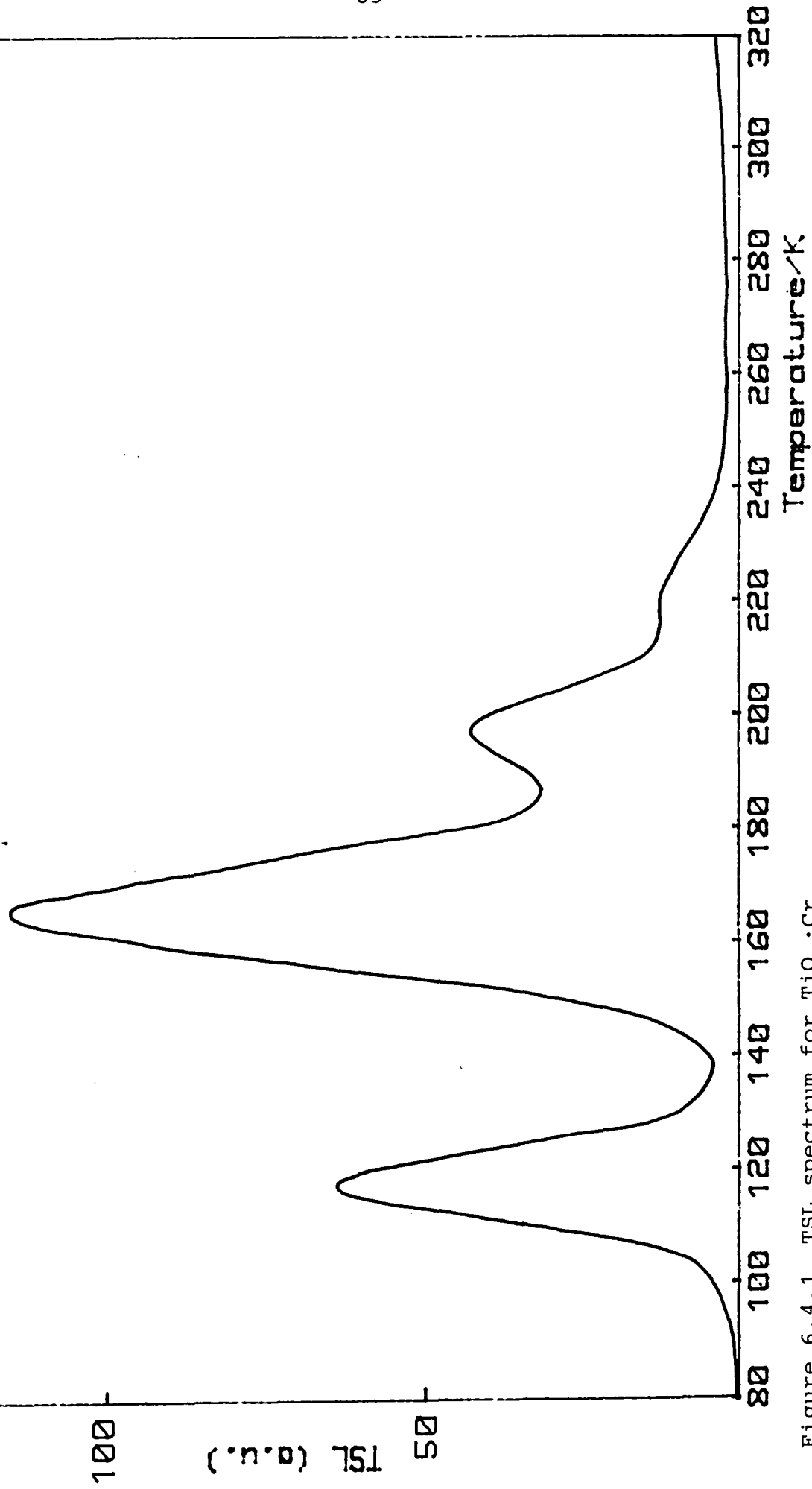


Figure 6.4.1 TSL spectrum for TiO₂:Cr

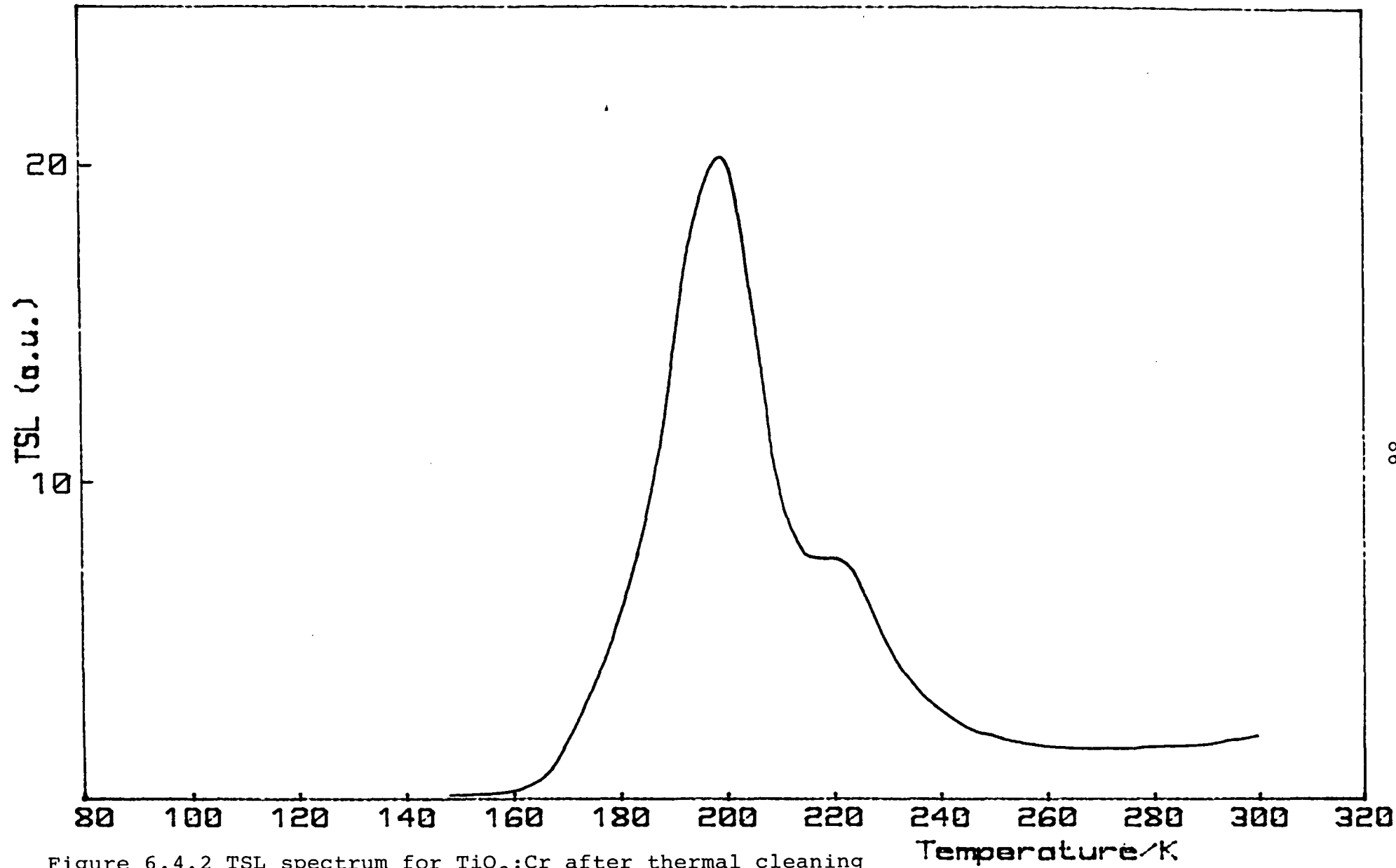


Figure 6.4.2 TSL spectrum for $\text{TiO}_2:\text{Cr}$ after thermal cleaning

165K

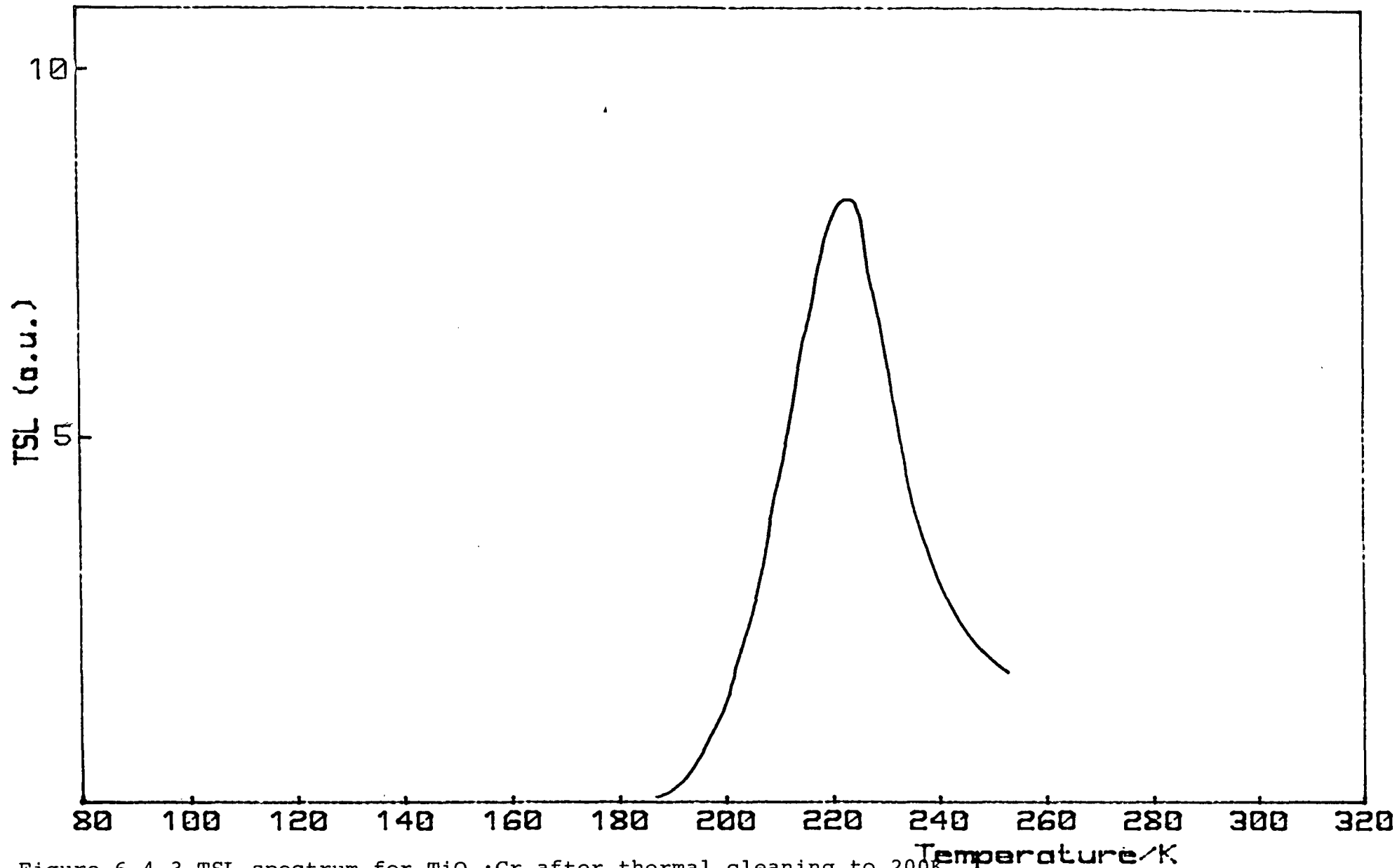


Figure 6.4.3 TSL spectrum for $\text{TiO}_2:\text{Cr}$ after thermal cleaning to 200K

This procedure was repeated at different heating rates to permit analysis of the peaks. The technique of thermal cleaning works best on overlapping peaks that decrease in intensity with increasing temperature, because only the lower temperature peaks can be removed. It was thus ideally suited to this sample.

During thermal cleaning, the higher temperature trap may be partially emptied. This emptying cannot be repeated reproducibly and this renders the analysis methods that rely on variations in peak height unreliable. Hoogenstraaten's analysis method [109], which only uses the peak temperature and heating rate was, therefore, employed in the analysis of the spectra. This method was applied to each of the four peaks after appropriate thermal cleaning to isolate the smaller peaks. The resulting plots of $\ln(T_m^2/w)$ against $1/T_m$, where T_m is the peak temperature and w is the heating rate, are shown in figures 6.4.4-7. It can be seen that good straight lines may be fitted through the points. The slopes of the lines yield the activation energies of the traps and the intercepts of the lines on the $\ln(T_m^2/w)$ axis enable the capture cross-sections of the traps to be calculated. A summary of the activation energies and cross-sections is given in table 6.4.1.

As described in section 5.4, undoped samples showed TSL peaks at 101, 118, 166, 245 and 284 K. The TSL peaks observed in the spectra from the chromium doped samples at 115 and 165 K clearly correspond to those seen in the undoped samples at the same temperatures and with the same activation energies. The other two peaks occurred in a temperature range where the undoped crystals showed some thermoluminescence but no resolved peaks. The intensities of the TSL peaks in the traces from the chromium doped samples were higher than the corresponding peaks from the undoped samples. This is consistent with the observation of increased photoluminescence intensity from the chromium doped samples and with the attribution of Cr^{3+} as the radiative centre in rutile.

TSC experiments were also carried out on these samples. The production of good spectra proved impossible because of significant noise below 180 K and a large dark conductivity above that temperature. A typical TSC spectrum is shown in

**Activation energies and capture
cross-sections for Cr doped rutile**

	Peak Temperature			
	115	165	200	220
Hoogenstraaten	0.22	0.38	0.55	0.58
Cross-section	10^{-18}	10^{-17}	10^{-14}	5×10^{-16}

Trap depths in eV Error \pm 0.02 eV
Cross-sections in cm^2

Table 6.4.1

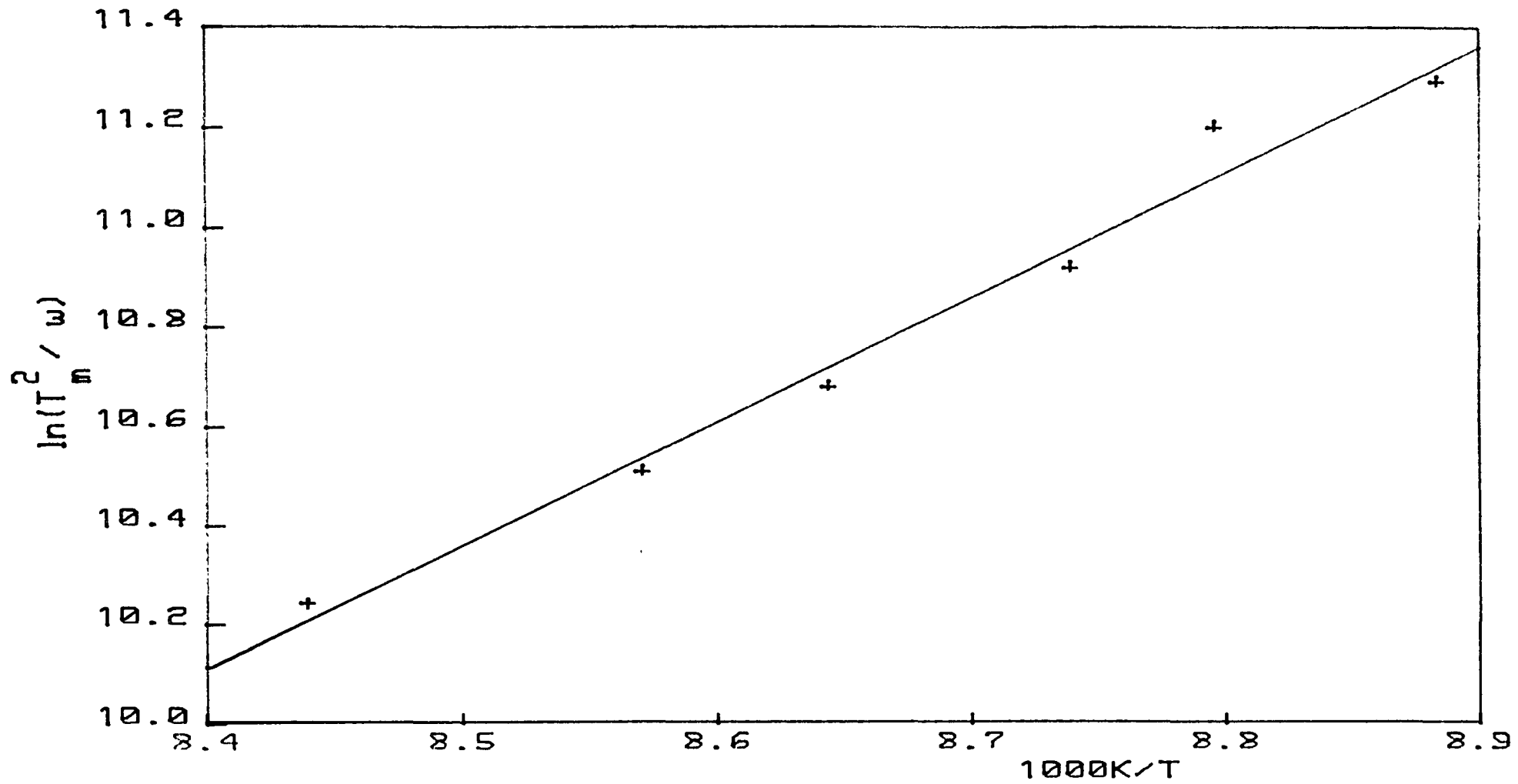


Figure 6.4.4 Analysis of peak at 115K in $TiO_2:Cr$

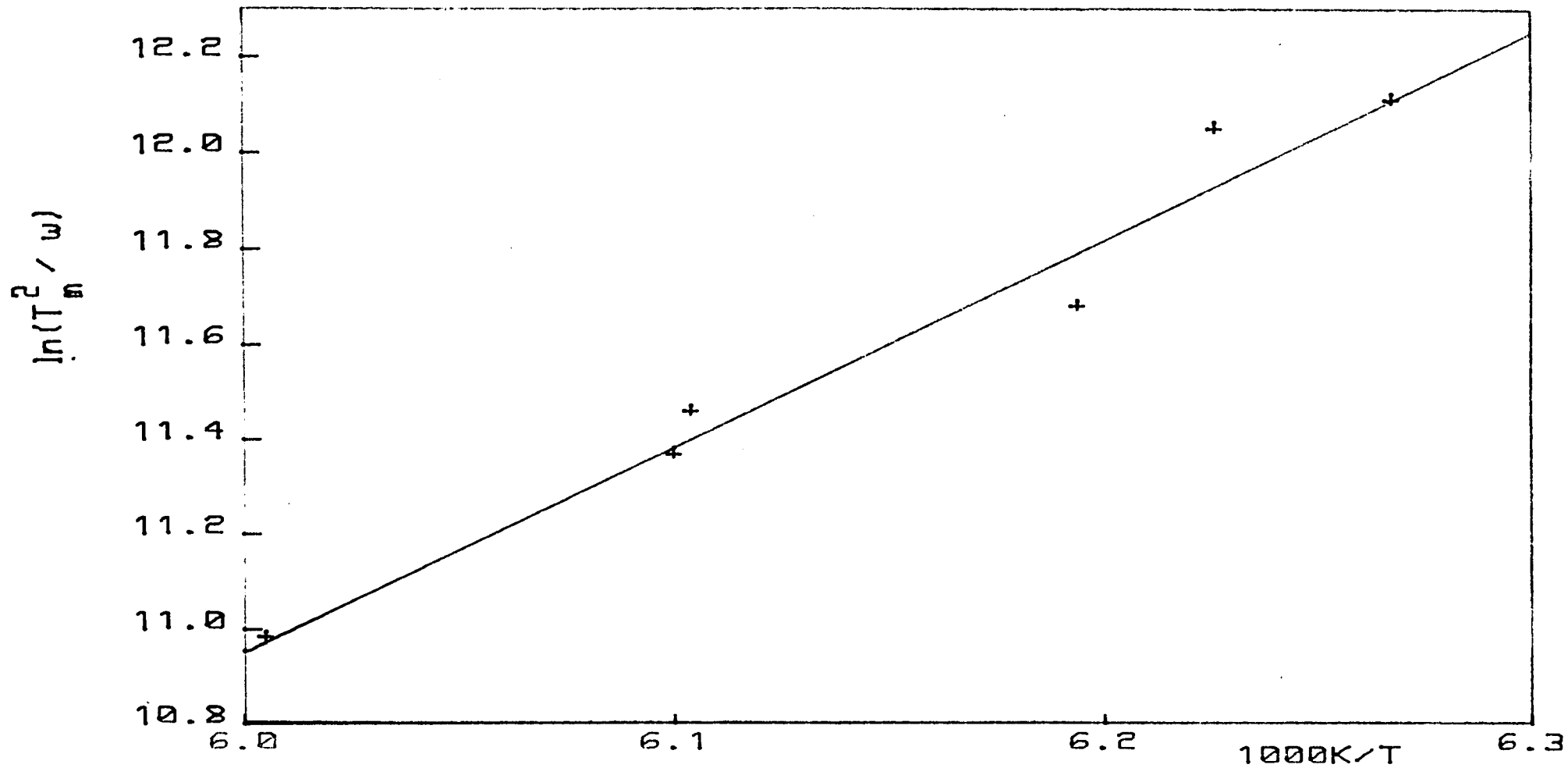


Figure 6.4.5 Analysis of peak at 165K in $TiO_2:Cr$

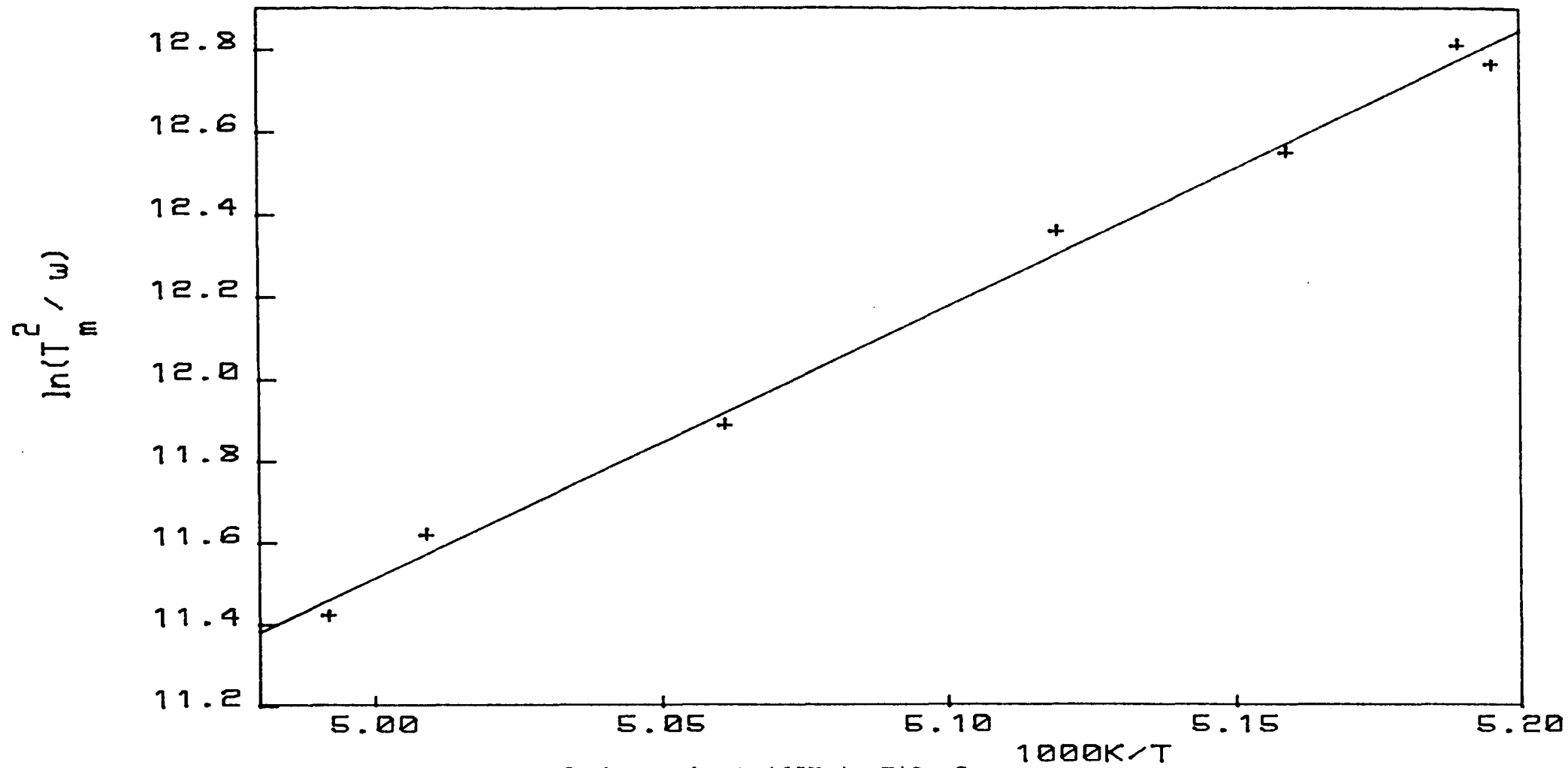


Figure 6.4.6 Analysis of the peak at 165K in $TiO_2:Cr$

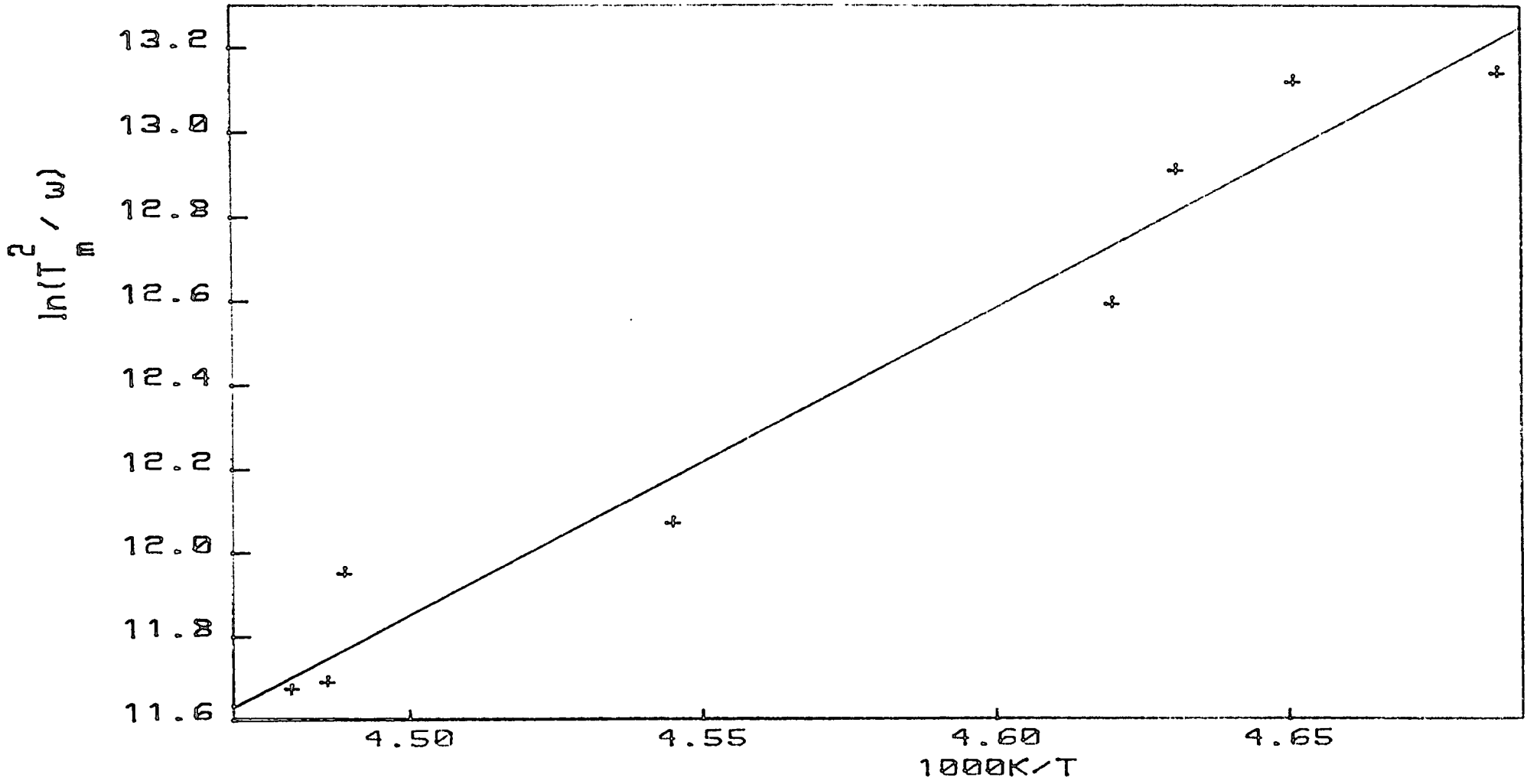


Figure 6.4.7 Analysis of the peak at 220K in $TiO_2:Cr$

figure 6.4.8. There is appreciable dark conductivity but peaks at about 190, 250 and 380 K can also be seen. The spectrum was plotted as $\ln(I)$ against $1/T$ and the result is shown in figure 6.4.9. The dark conductivity shows two linear segments with activation energies of 0.12 ± 0.1 eV below 295 K and 0.51 ± 0.2 eV above that. Subtracting the dark conductivity from the total TSC spectrum isolated the three peaks and the result is shown in figure 6.4.10. The area under a TSC curve when plotted as current versus time is proportional to the trap density since this represents the amount of charge released. For the case shown in figure 6.4.10 it would seem that the trap densities are in the ratio $1:100:10^4$ for the traps at 190, 250 and 380 K respectively. The area under the curve for the trap at 380 K is certainly much greater than that shown in figure 5.4.5 for an undoped sample. However, great care should be exercised in this situation, because several investigators [104,161-163] have suggested that the TSC method is not suitable for use in materials in which the dark current is of the same order as, or larger than the TSC excess current.

Hillhouse [10] has reported TSL and TSC spectra from chromium doped rutile crystals. He found eight TSL peaks, which occurred at temperatures of 89, 101, 118, 167, 191, 238, 299 and 324 K, and six TSC peaks, which occurred at 92, 103, 119, 176, 211 and 244 K, corresponding to his first six TSL peaks. The TSL peaks observed at 115, 165 and 200 K in the present study correspond to three of those observed by Hillhouse. The peak at 220 K was not found by Hillhouse and there was no evidence for a peak at 89 K which Hillhouse found in chromium doped rutile but not in undoped rutile. A comparison between the TSL results presented above and those reported by Hillhouse is given in table 6.4.2. The results from Ghosh et al [146] for nominally undoped rutile are also given. It can be seen that there is good agreement between this work and Hillhouse for the peaks at 115 and 165 K but a discrepancy occurs at 200 K, where better agreement is found with the work of Ghosh. The energies of 0.55 and 0.58 eV for the 200 and 220 K peaks, respectively, are consistent with the value of 0.68 eV found for the 240 K peak seen in undoped rutile.

Activation energies could not be obtained from the TSC spectra and it is,

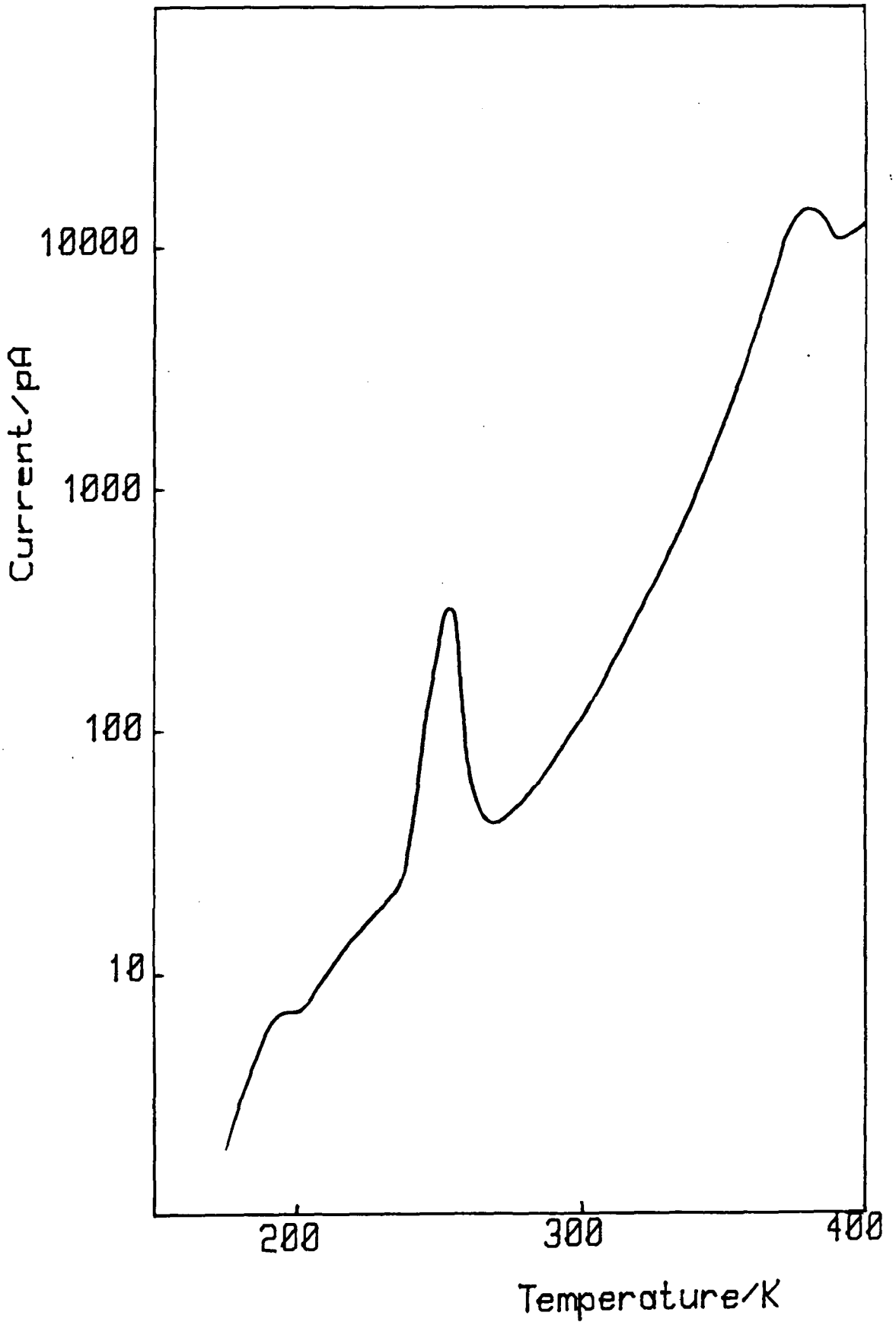


Figure 6.4.8 TSC spectrum for $\text{TiO}_2:\text{Cr}$

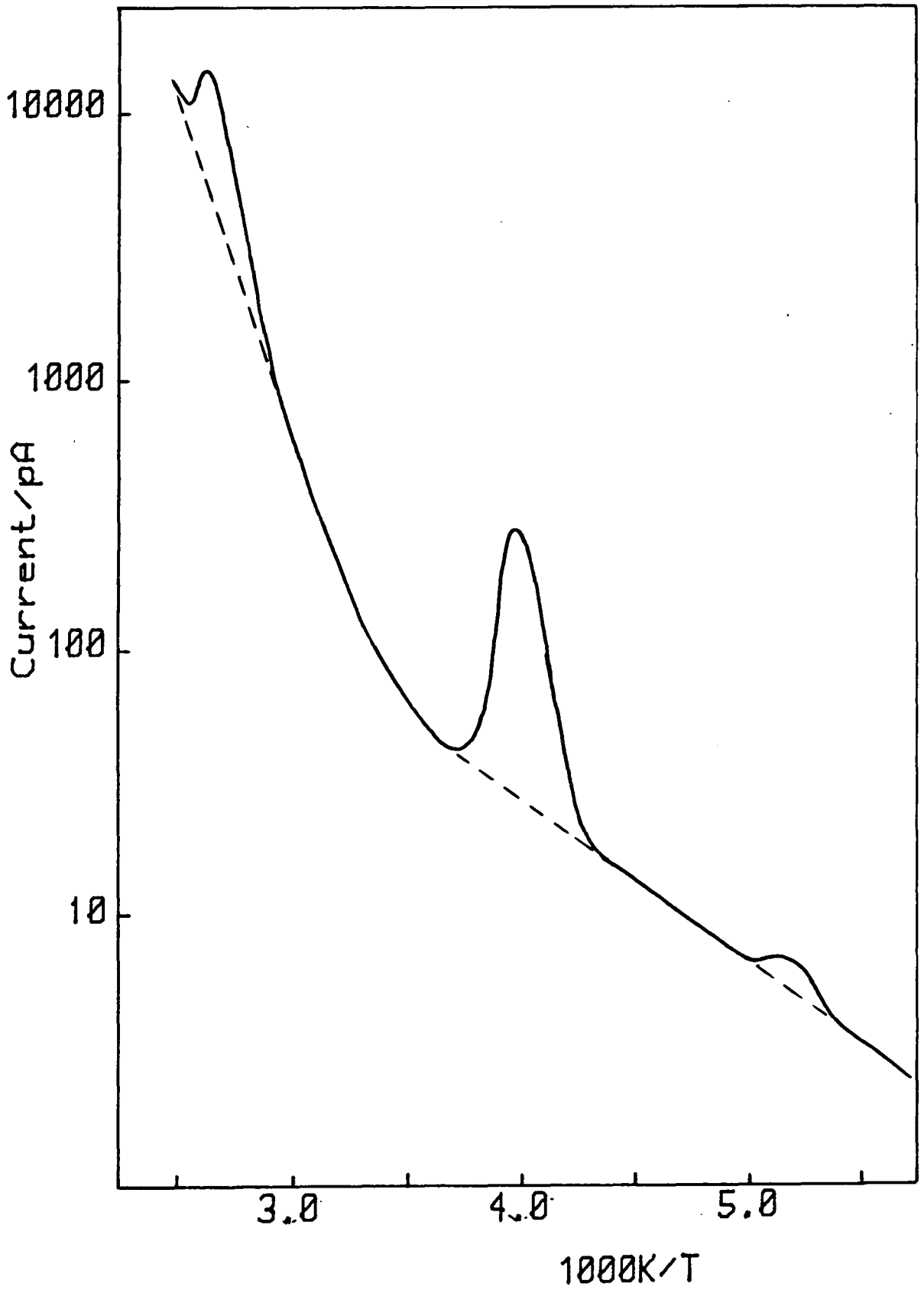


Figure 6.4.9 TSC spectrum for $\text{TiO}_2:\text{Cr}$

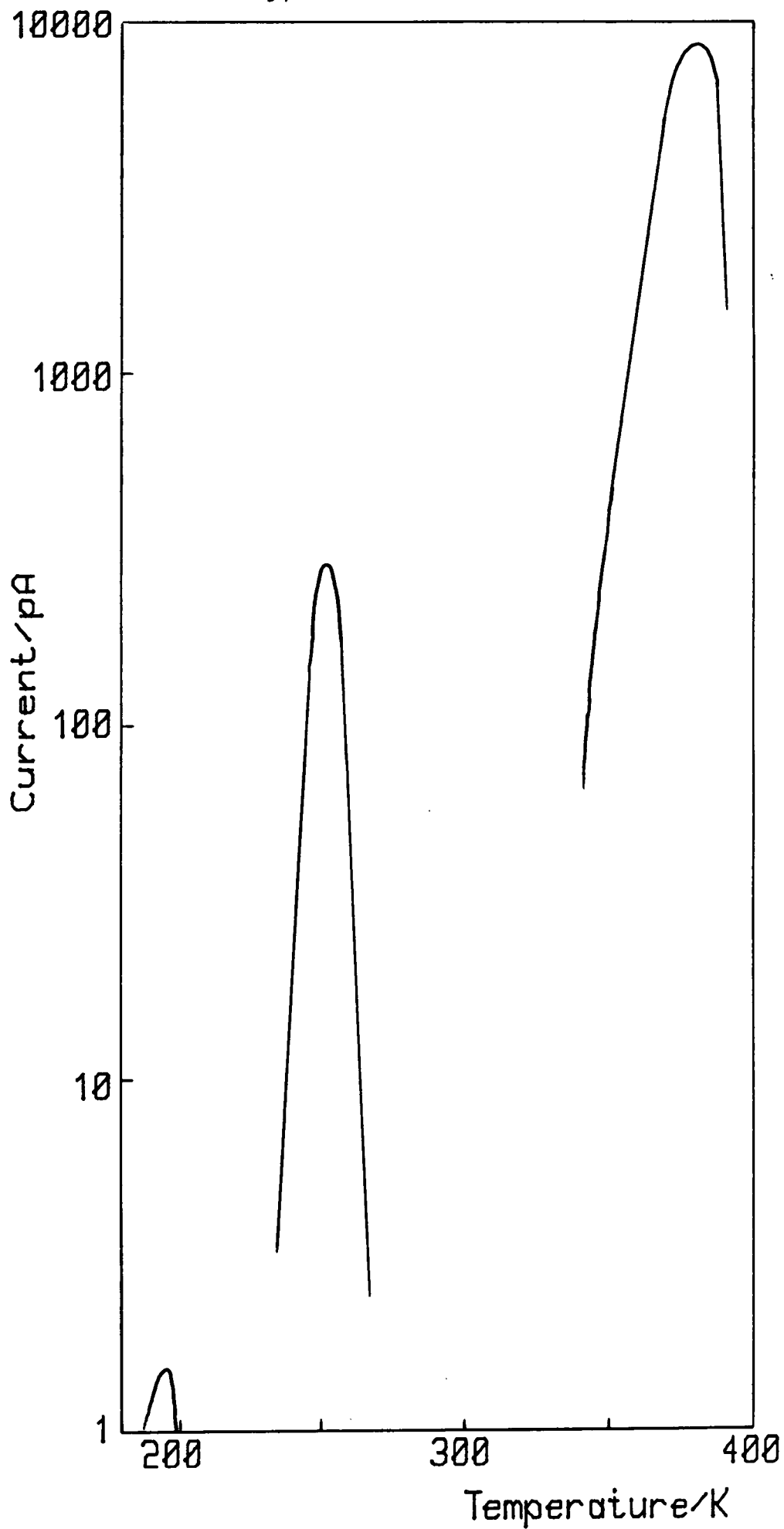


Figure 6.4.10 Excess of TSC over dark current for TiO₂:Cr

Comparison of trap parameters
for chromium doped rutile

Peak	This work		Hillhouse		Ghosh et al
Peak	E_T	σ	E_T	σ	E_T
89			0.18	10^{-18}	0.27
101			0.13	10^{-21}	0.28
115	0.22	10^{-18}	0.23	10^{-19}	0.32
165	0.38	10^{-17}	0.37	10^{-19}	0.48
200	0.55	10^{-14}	0.42	10^{-18}	0.56
220	0.58	5×10^{-16}			
238			0.52	10^{-19}	0.62
299			0.61		0.76
328			0.73	10^{-19}	0.87

Trap depths (E_T) in eV

Cross-sections (σ) in cm^2

Table 6.4.2

therefore, difficult to correlate these with the TSL spectra. It is possible that the TSC peak occurring at 195 K could correspond to the TSL peak at 200 K although, in general, TSC peaks occur at higher temperatures than corresponding TSL peaks [150]. The peak occurring at 250 K could correspond to that observed by Hillhouse at 244 K and also seen in an undoped NL sample. However, there would then be no TSC peak corresponding to the TSL peak at 220 K.

6.5 SUMMARY

Chromium doped rutile samples were studied by the methods of photoluminescence, thermoluminescence and thermally stimulated conductivity. Introduction of chromium into the rutile lattice increased the photoluminescence intensity and the intensity of the TSL spectrum; this was attributed to Cr^{3+} being the radiative centre in rutile.

The photoluminescence characteristics were very similar to those of undoped rutile apart from the increase in intensity. An activation energy of 0.35 eV for the thermal quenching of the luminescence was found, in agreement with that found for undoped rutile.

Thermoluminescence experiments showed the presence of four traps. Two of these have been seen in undoped rutile; the peaks associated with the other two traps occurred in a temperature range where undoped samples showed some thermoluminescence but no resolved peaks. The technique of thermal cleaning was used successfully to isolate overlapping peaks and allow analysis. Activation energies obtained from the analysis agreed well with previously reported values for three of the four peaks.

Thermally stimulated current measurements were dominated by a large dark current. This could be subtracted from the total TSC trace to isolate three peaks occurring above 190 K.

CHAPTER 7

IRON DOPED CRYSTALS

- 7.1 Introduction**
- 7.2 Material preparation**
- 7.3 Photoluminescence**
- 7.4 Thermally stimulated luminescence and conductivity**
- 7.5 Summary**

7.1 INTRODUCTION

Both chromium and iron dopants are known to affect the durability of paint films made from rutile pigments. The effect of doping with chromium was described in the previous chapter; the effect of doping with iron is described here.

7.2 MATERIAL PREPARATION

Two types of iron doped crystal were studied. The first type was doped by heating an undoped crystal with some iron filings in an evacuated quartz ampoule for 24 hours at 1050°C, followed by an anneal in oxygen for 24 hours at 1000°C. The second type had been doped with iron during growth.

The samples were cut, cleaned and mounted for measurement as described in chapter 4.

7.3 PHOTOLUMINESCENCE

Photoluminescence emission spectra from iron doped samples showed the same broad band emission at about 860nm as was observed from undoped samples. The emission intensity was approximately one tenth of that from undoped samples.

The temperature dependence of the photoluminescence emission intensity under constant illumination was measured for both types of samples described in the previous section. The results for the diffusion doped and plasma doped samples are shown in figures 7.3.1 and 7.3.2, respectively. It can be seen that the photoluminescence has a different temperature dependence than was observed in either undoped or chromium doped samples and that the doping causes a reduction in intensity of approximately an order of magnitude compared with undoped samples. The luminescence intensity shows a small decrease with increasing temperature and does not show the slight increase followed by a sharp fall that was observed from



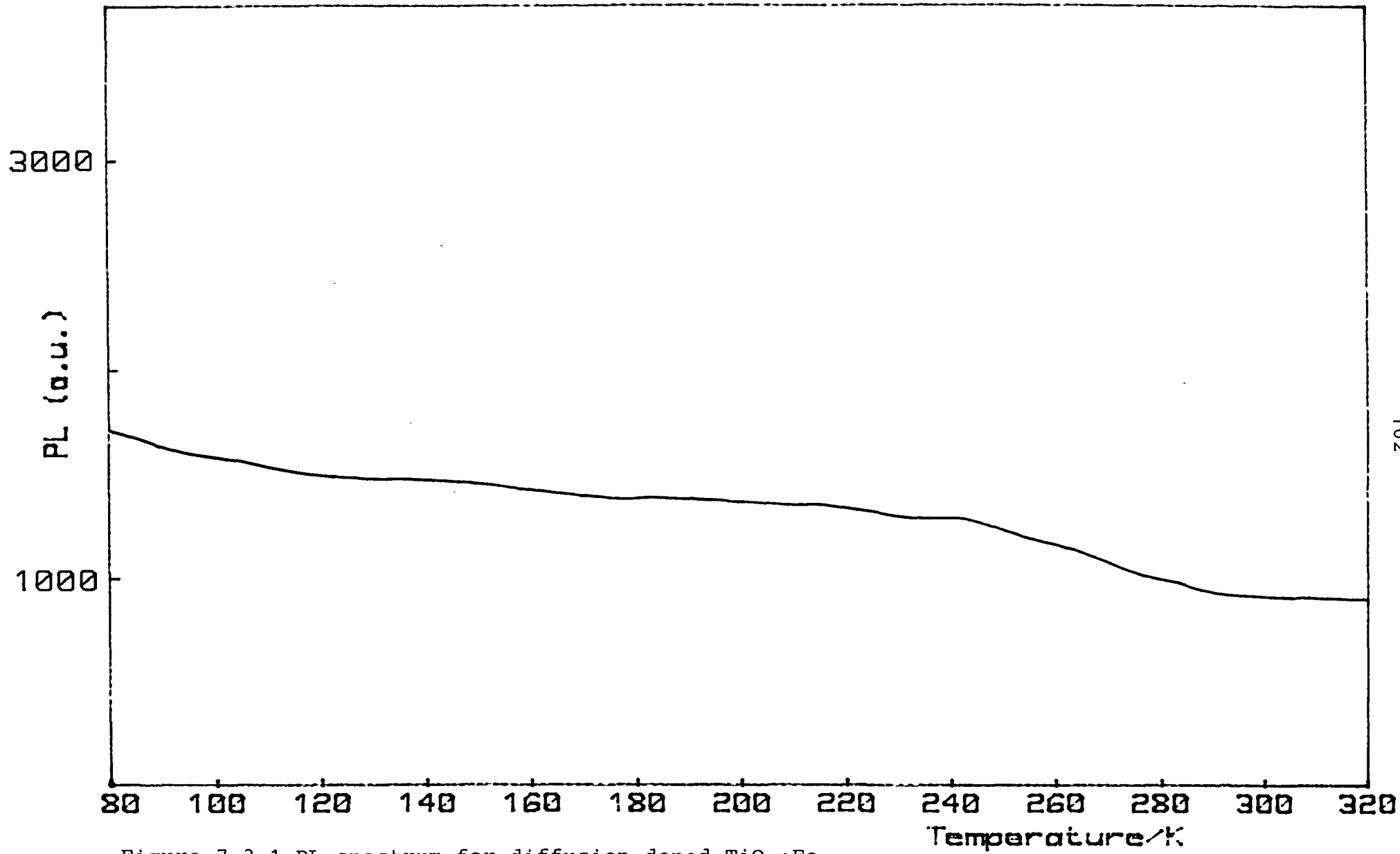


Figure 7.3.1 PL spectrum for diffusion doped $\text{TiO}_2:\text{Fe}$

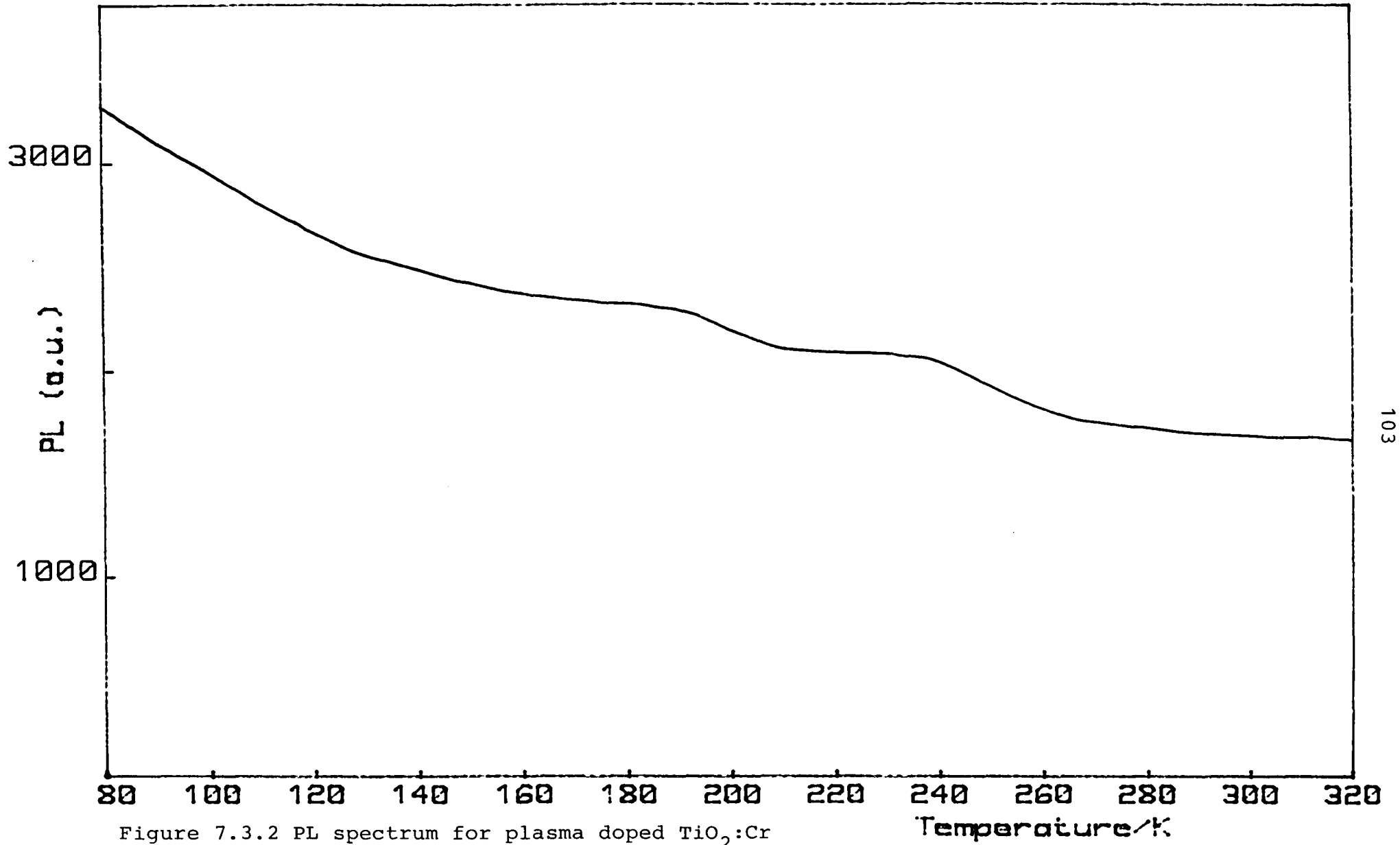


Figure 7.3.2 PL spectrum for plasma doped TiO₂:Cr

undoped and chromium doped samples. It seems unlikely that the mechanism proposed for the decrease in luminescence efficiency in undoped rutile could also be solely responsible for the decrease observed in the iron doped results and plots of $\ln((1-\eta)/\eta)$ against $1/T$, taking $\eta=1$ at 80 K, did not yield straight lines. A possible explanation is that the iron provides a fast non-radiative recombination path which competes with the luminescent chromium recombination path for carriers excited to the conduction band, thus both reducing the photoluminescence intensity and changing its temperature dependence.

7.4 THERMALLY STIMULATED LUMINESCENCE AND CONDUCTIVITY

TSL experiments were carried out on the iron doped samples studied in the photoluminescence experiments described above. TSC experiments were carried out on the sample produced by plasma doping.

A typical TSL spectrum from a plasma doped crystal is shown in figure 7.4.1. Three peaks are apparent in the spectrum, occurring at 170, 195 and 222 K, and above 260 K the TSL intensity increases without peaking. Similar results were obtained from a diffusion doped sample as shown in figure 7.4.2, although, in this case, the middle peak occurs at 202 K and the peak at 222 K is not clearly resolved. The increase in TSL intensity above 260 K is also seen. There is a difference in TSL intensity between the two samples which is consistent with the difference in photoluminescence intensity between them. Both samples show a reduction in TSL intensity compared to an undoped sample. In particular, the TSL intensity from the plasma doped crystal, as shown in figure 7.4.1, was very low and this made thermal cleaning to isolate the high temperature peaks impossible.

Thermal cleaning was carried out on TSL spectra from the diffusion doped sample and analysis of the variation in peak temperature with heating rate by Hoogenstraaten's method [109] yielded values of 0.36, 0.40 and 0.59 eV (all ± 0.2 eV) for the activation energies of the traps. These values agree closely with those

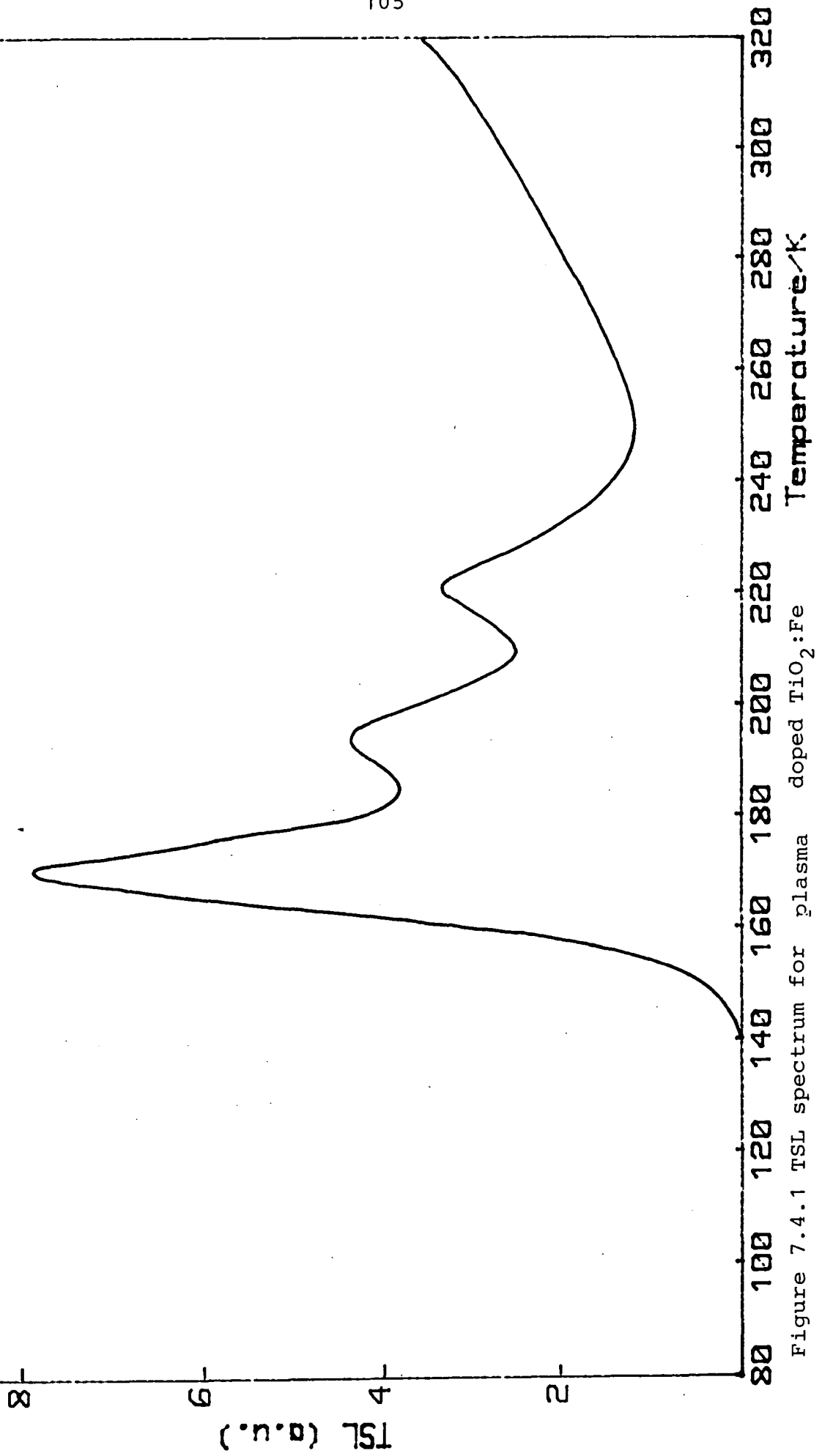


Figure 7.4.1 TSL spectrum for plasma doped TiO₂:Fe

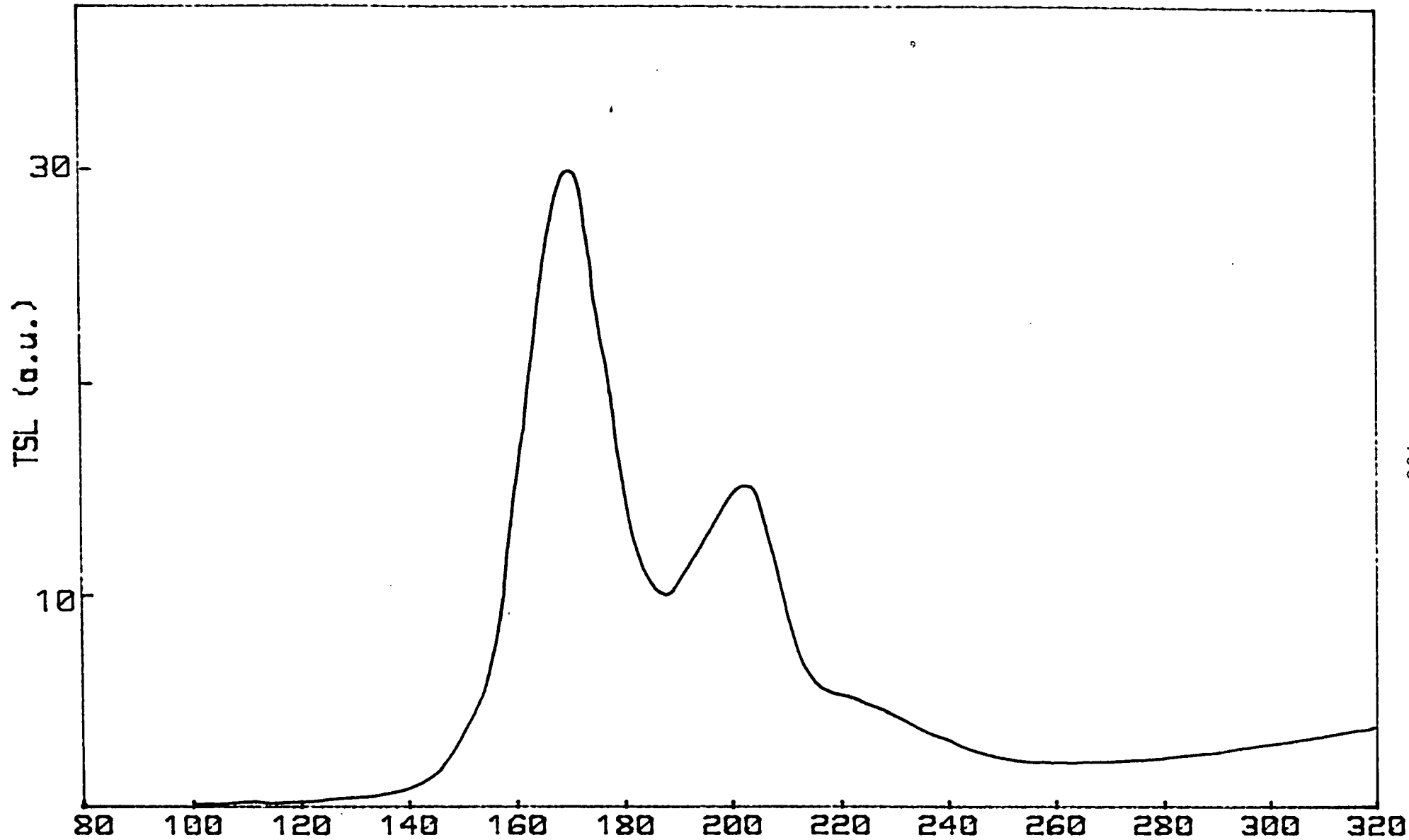


Figure 7.4.2 TSL spectrum from diffusion doped TiO₂:Fe

Temperature/K

reported by Hillhouse [10] for iron doped rutile. The values for the peaks at 170 and 222 K agree with the activation energies obtained by analysis of TSL spectra from chromium doped rutile as described in chapter 6. However, the peak seen at 200 K in spectra from chromium doped rutile yielded a value of 0.55 eV for its activation energy. This difference cannot be attributed to errors in determining the activation energies and seems to be due to a genuine difference in trap depth, with associated differences in emission kinetics causing the TSL peaks to occur at similar temperatures. There is also a large difference between the values of capture cross-section determined for these two peaks. The cross-section determined for the 200 K peak in the chromium doped sample was 10^{-14} cm^2 while that for the iron doped sample was $3 \times 10^{-19} \text{ cm}^2$. A difference in capture cross-section would be expected for two peaks occurring at the same temperature but with different activation energies.

It was possible to obtain TSC spectra from the plasma doped sample and a typical result is shown in figure 7.4.3. Three peaks are clearly visible, occurring at 183, 204 and 238 K, and above 260 K the dark current becomes dominant. The three TSC peaks appear to correspond to the peaks observed in the TSL spectra but occur between 9 and 16 K higher in temperature. Fields and Moran [150] have derived a correlation expression for TSL and TSC. Their analysis leads to a theoretical prediction that the TSL is decreasing at the TSC peak or, in other words, that the TSC peak occurs at a higher temperature than the TSL peak. Kivits and Hagebeuk [75] in their theoretical analysis of the simple trap model have shown that the temperature of the TSL maximum is insensitive to the retrapping ratio $\delta = \beta/\alpha$, where β is the trapping rate constant and α is the recombination rate constant, whereas the temperature of the TSC peak is dependent on δ such that the peak moves to highertemperatures for small values of δ . To explain the temperature dependence of the photoluminescence it has been proposed that iron doping introduces a fast recombination pathway for electrons in the conduction band. This, in turn, implies a small value of δ and, therefore, a large difference between

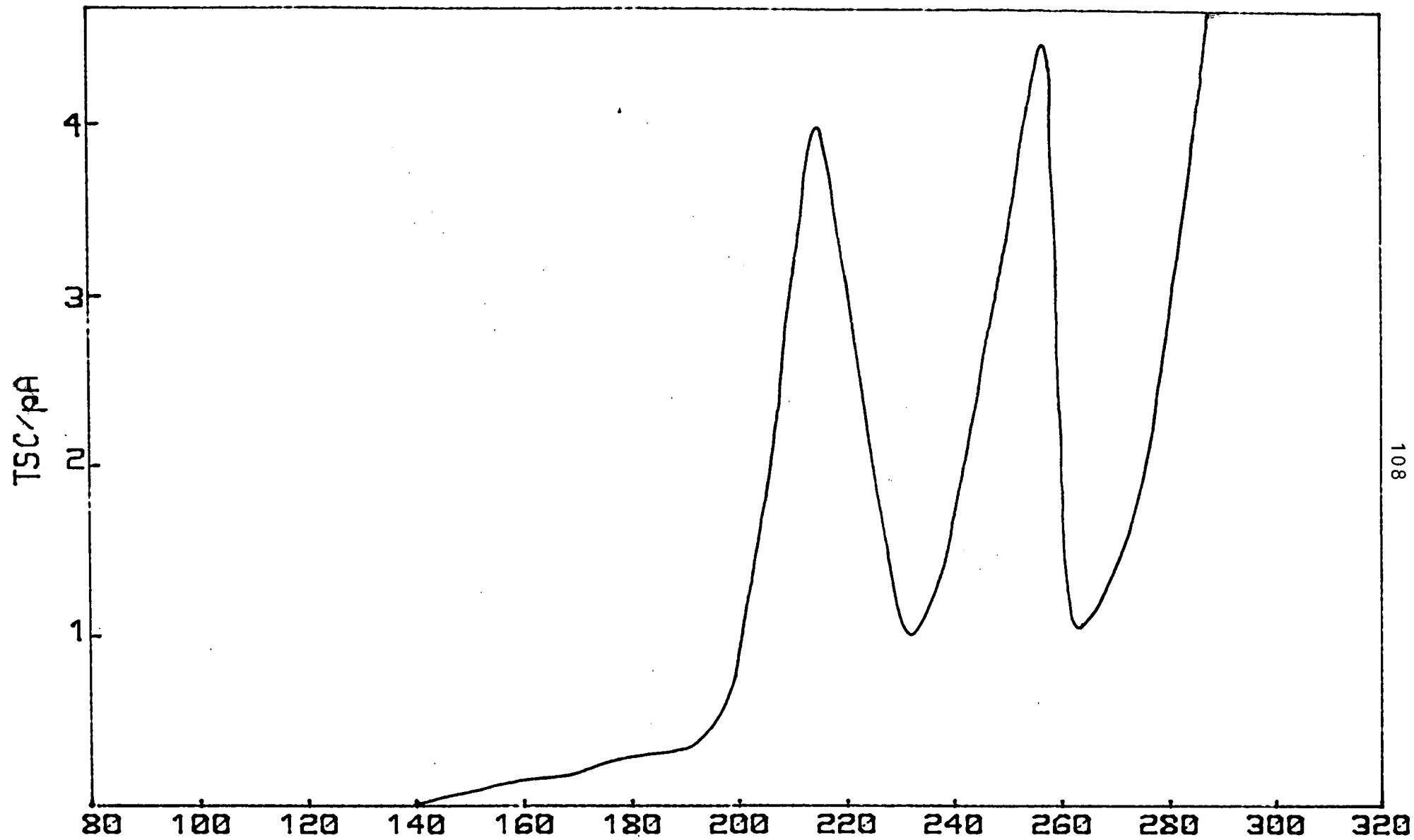


Figure 7.4.3 TSC spectrum from plasma doped TiO₂:Fe

the peak temperatures for TSL and TSC would be expected.

The TSC spectrum above 250 K was plotted as $\log(I)$ against reciprocal temperature as was a spectrum obtained without exciting the sample. These are shown in figure 7.4.4. It can be seen that above 340 K the two spectra are coincident indicating that there are no TSC peaks in this temperature range, unlike the TSC spectra obtained from chromium doped rutile which showed a large peak at 380 K.

7.5 SUMMARY

Iron doped samples were studied by the methods of photoluminescence, thermoluminescence and thermally stimulated conductivity.

Introduction of iron into the rutile lattice reduced the intensity of the photoluminescence and caused a change in its temperature dependence. These changes were attributed to a fast non-radiative recombination path competing with the luminescent transition.

Thermoluminescence experiments showed the presence of three traps. These occurred at temperatures where peaks had been observed in chromium doped samples, although activation energy determination yielded consistent values for only two of the three traps.

Thermally stimulated conductivity measurements showed three peaks with a large dark current at high temperatures. No evidence was found for a peak occurring at about 380 K which had been seen in TSC spectra from chromium doped samples.

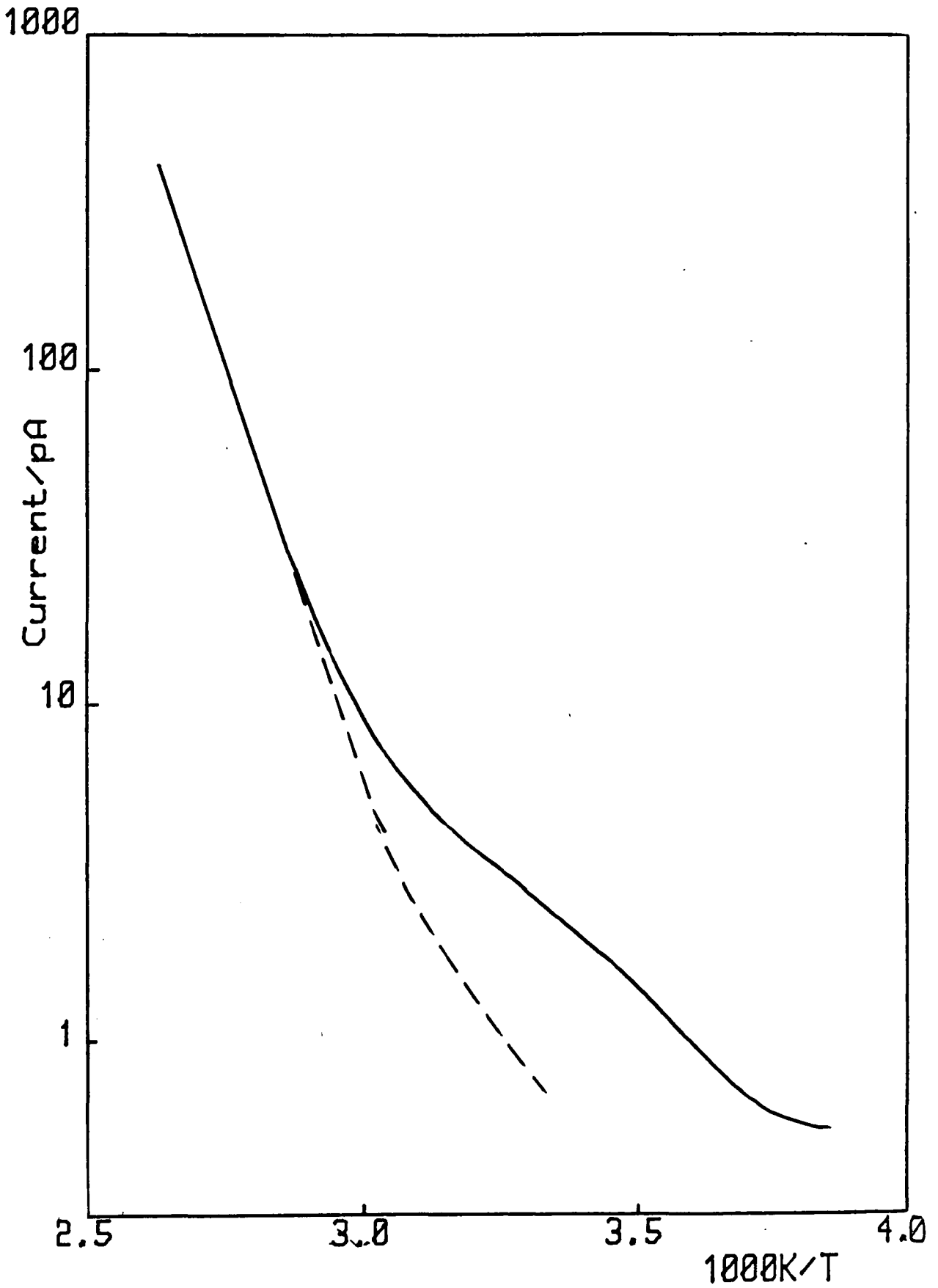


Figure 7.4.4 TSC and dark current for plasma doped $\text{TiO}_2:\text{Fe}$

CHAPTER 8

MANGANESE DOPED CRYSTALS

- 8.1 Introduction**
- 8.2 Photoluminescence**
- 8.3 Thermoluminescence**
- 8.4 Summary**

8.1 INTRODUCTION

Samples doped with three other transition metal dopants were available. These had been diffusion doped with manganese, cobalt and nickel and were studied by photoluminescence and thermoluminescence. The results of the experiments on manganese doped rutile crystals are given in this chapter.

The manganese doping had been carried out by diffusion doping at 900°C for 24 hours, followed by an anneal in oxygen at 1000°C for 24 hours.

8.2 PHOTOLUMINESCENCE

The photoluminescence emission spectrum from manganese doped rutile showed the same broad band emission centred on about 860 nm as was observed from undoped samples. The emission intensity was approximately one tenth of that from undoped samples.

The temperature dependence of the photoluminescence emission intensity under constant illumination is shown in figure 8.2.1. It can be seen that the intensity reduces steadily from 80 K and does not show the slight increase followed by a sharp fall in intensity that was observed from undoped samples. This temperature dependence is similar to that observed for iron doped rutile and described in the previous chapter. The intensity of the photoluminescence is also similar to that of iron doped rutile and less than that of undoped rutile. This behaviour indicates that manganese introduces a fast non-radiative recombination centre that competes with the luminescence transition.

8.3 THERMOLUMINESCENCE

TSL experiments were carried out on the manganese doped single crystal rutile. A typical TSL spectrum is shown in figure 8.3.1. Four peaks are apparent in

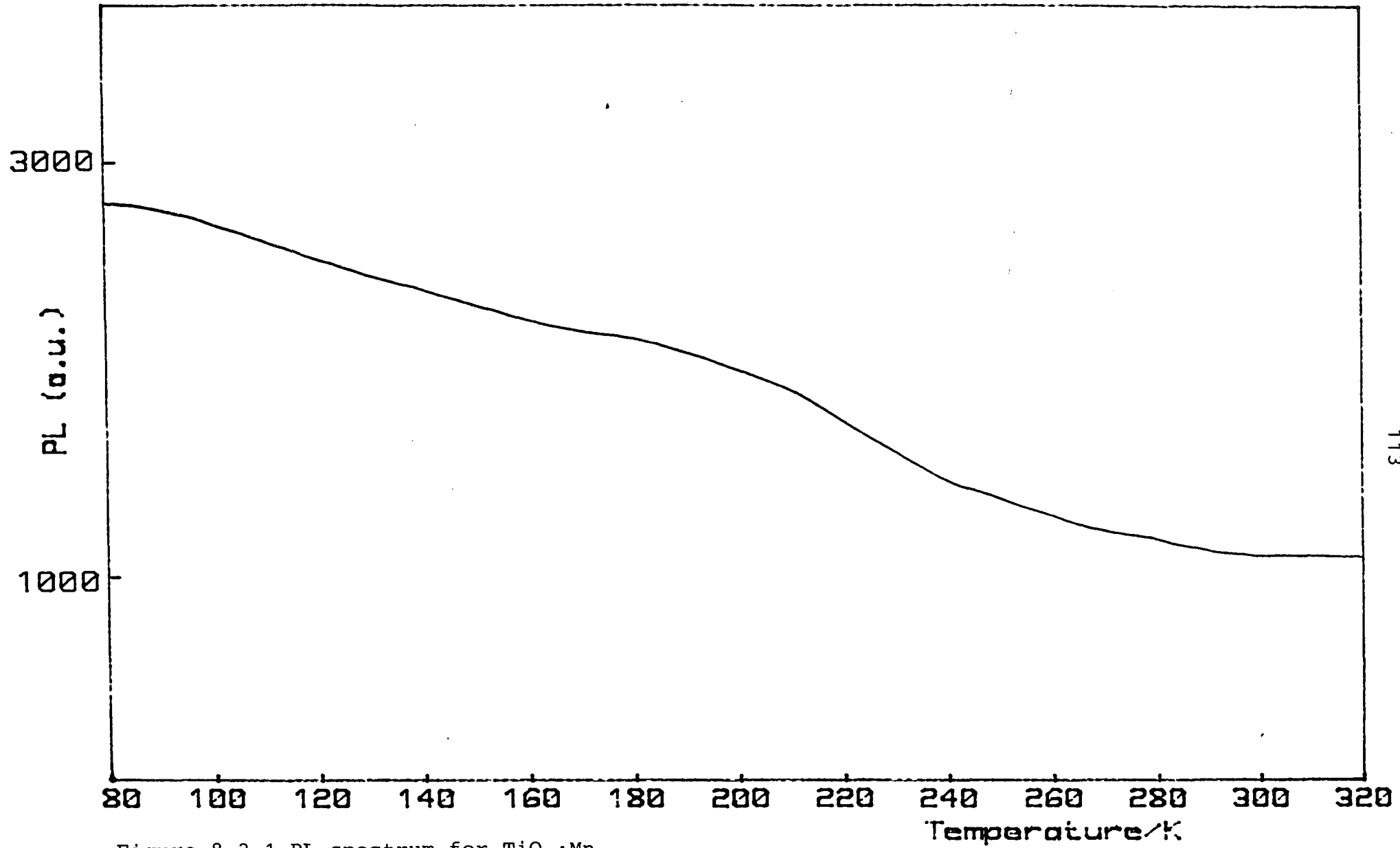


Figure 8.2.1 PL spectrum for $\text{TiO}_2:\text{Mn}$

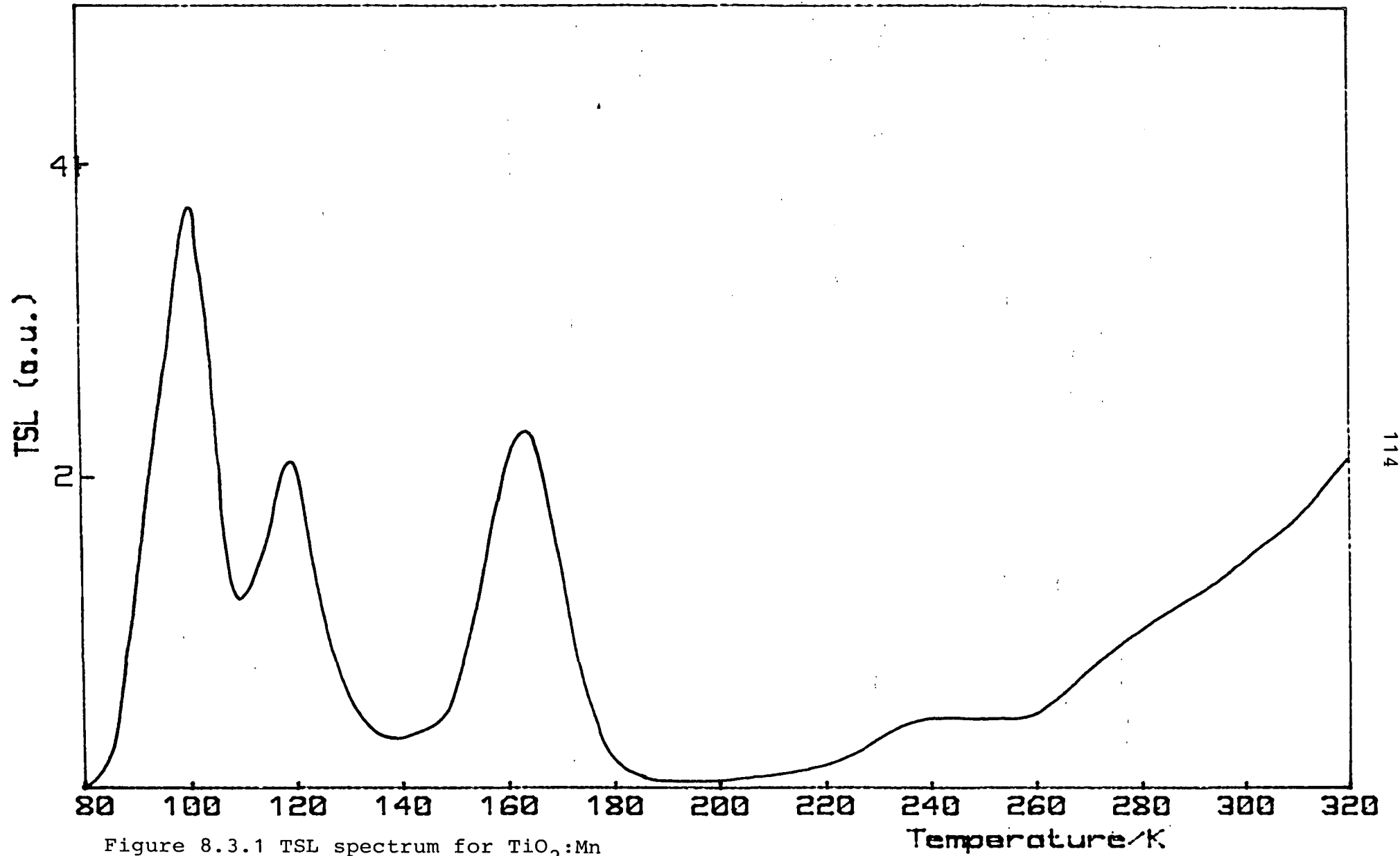


Figure 8.3.1 TSL spectrum for $\text{TiO}_2:\text{Mn}$

the spectrum, occurring at 101, 120, 164, and 240 K. Above 240 K the TSL intensity increases gradually without peaking.

Analysis of the peaks yielded values of 0.15, 0.20, 0.36 and 0.58 eV (all ± 0.02 eV) for the activation energies using the method of Hoogenstraaten [109]. These values of peak temperature and activation energy agree very closely with the four lowest temperature peaks observed in TSL spectra obtained from undoped samples, as described in chapter 5, but the absolute and relative magnitudes of the peaks differ markedly. In particular, the magnitude of the peak at 164 K is seen to be comparable to that of the peaks at 101 and 120 K, whereas in spectra from undoped samples it was found to be an order of magnitude higher than those peaks. This cannot be explained solely by the reduction in luminescence efficiency, and it would seem that the ratio of trap density for these peaks is changed. The fifth peak seen in the undoped spectra at 284 K was not detected but it is likely that, if it existed, it would be hidden by the steady rise in TSL seen above 240 K.

Hillhouse [10] has reported TSL spectra from manganese doped rutile. He found the same four peaks described here but did not determine activation energies for them.

8.4 SUMMARY

Manganese doped samples were studied by photoluminescence and thermoluminescence.

Introduction of manganese into the rutile lattice reduced the photoluminescence emission intensity and caused a change in the temperature dependence of the photoluminescence. This behaviour had also been observed for iron doped samples and may be attributed to a fast non-radiative recombination path competing with the luminescent transition.

Thermoluminescence experiments showed the presence of four traps. These had all been observed in undoped rutile.

CHAPTER 9

COBALT DOPED CRYSTALS

- 9.1 Introduction
- 9.2 Photoluminescence
- 9.3 Thermoluminescence
- 9.4 Summary

9.1 INTRODUCTION

A sample doped with cobalt was studied by photoluminescence and thermoluminescence. The doping had been carried out by diffusion at 1050°C for 24 hours followed by an anneal in oxygen at 1000°C for 24 hours.

9.2 PHOTOLUMINESCENCE

The photoluminescence from cobalt doped rutile showed the same broad band emission centred on about 860 nm as had been observed from undoped samples. The emission intensity was approximately one tenth of that from undoped rutile.

The temperature dependence of the photoluminescence intensity under constant illumination is shown in figure 9.2.1. It can be seen that the intensity reduces steadily from 80 K in the same manner as that observed for iron and manganese doped samples. The intensity of the photoluminescence is also similar to that from iron and manganese doped samples. It seems, therefore, that cobalt also introduces a fast recombination centre which competes with the Cr^{3+} luminescence.

9.3 THERMOLUMINESCENCE

TSL experiments were carried out on the cobalt doped single crystal rutile and a typical TSL spectrum is shown in figure 9.3.1. Four peaks are apparent in the spectrum, occurring at 101, 120, 166 and 190 K. Above 200 K, the TSL intensity increases without peaking. It can be seen that the intensity of the thermoluminescence is extremely low, with the peak at 166 K having a maximum intensity of only 5% of that measured for undoped rutile. The accurate determination of activation energies was very difficult for this sample because of the low level of the TSL. However, energies can be assigned to the first three peaks by inference from the results obtained for other dopants. Consistent values of 0.14, 0.22

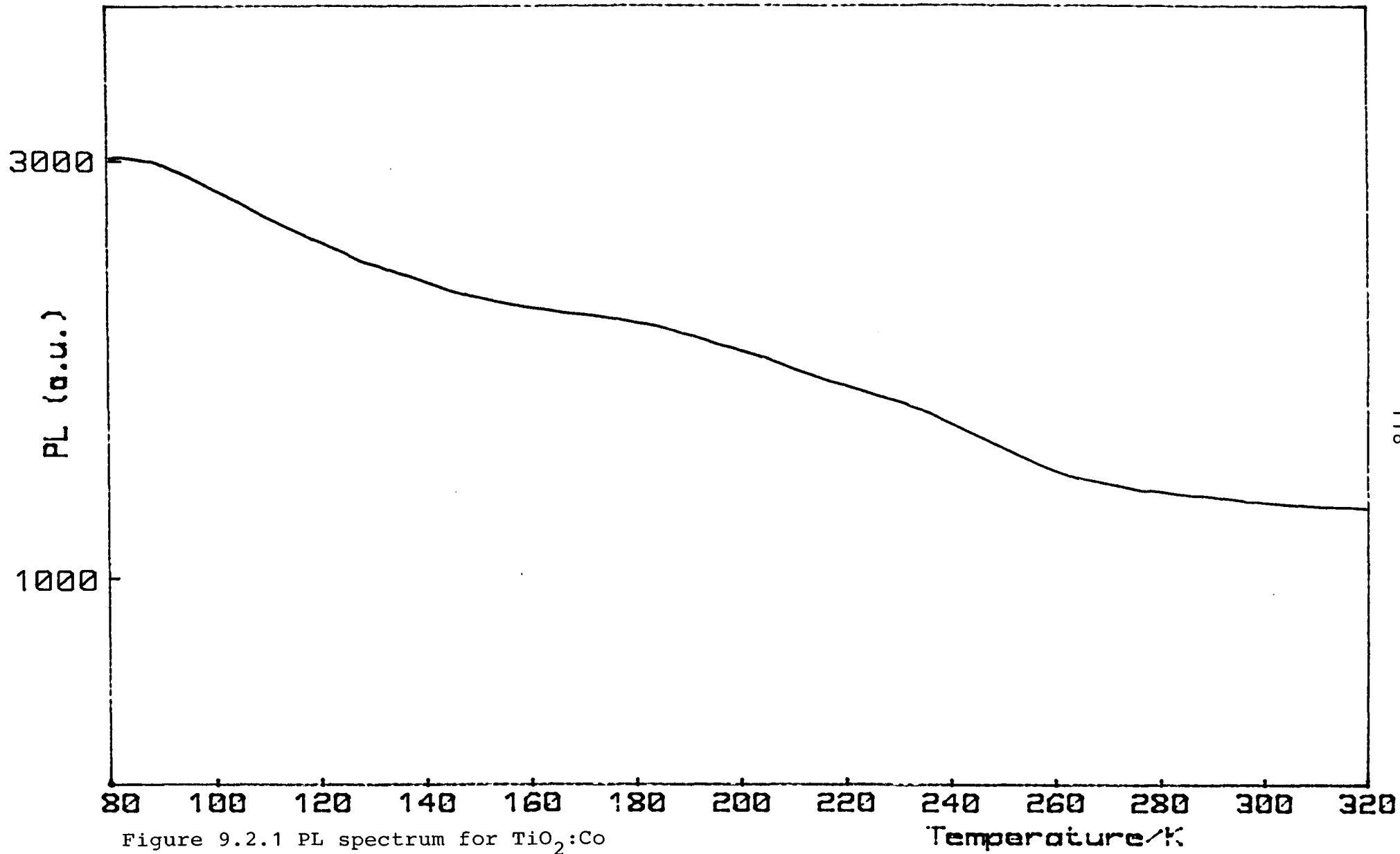


Figure 9.2.1 PL spectrum for $\text{TiO}_2:\text{Co}$

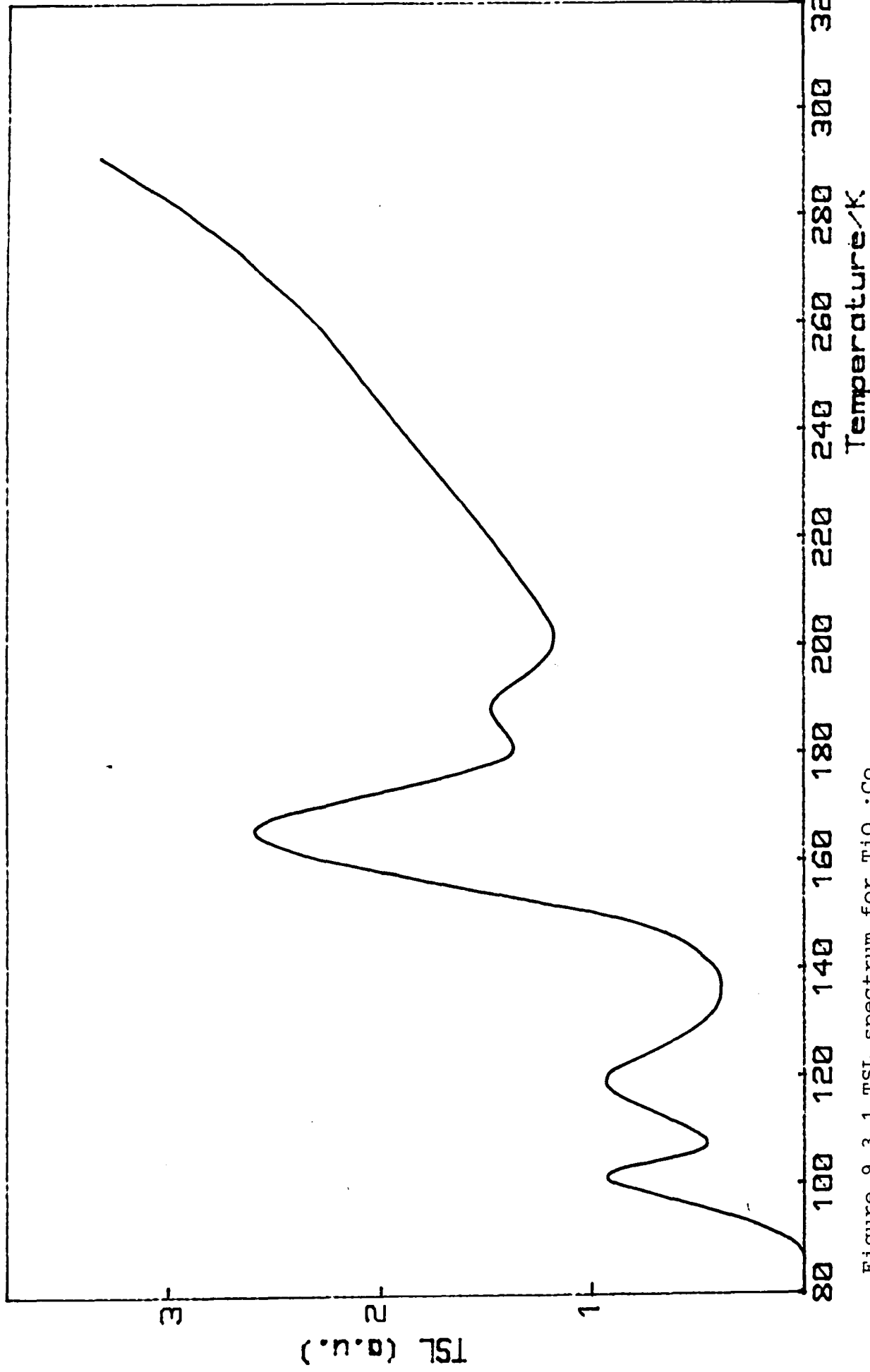


Figure 9.3.1 TSL spectrum for TiO₂:Co

and 0.37 eV have been determined for the peaks at 101, 120 and 166 K, respectively, from at least two other dopants in each case. Peaks at about 190 K have been observed from both chromium and iron doped samples, but these yielded two different values of activation energy. It is not possible, therefore, to assign a value to the 190 K $\text{TiO}_2\text{:Co}$ peak by inference.

Hillhouse [10] has reported TSL spectra from cobalt doped rutile which showed the same four peaks described here. His analysis yielded a value of 0.42 ± 0.03 eV for the peak at about 200 K which agrees closely with the value of 0.40 ± 0.02 eV determined for the $\text{TiO}_2\text{:Fe}$ peak at 195 K and suggests that this value can be assigned to the 190 K cobalt doped peak.

9.4 SUMMARY

Cobalt doped samples were studied by photoluminescence and thermoluminescence.

Introduction of cobalt into the lattice reduced the photoluminescence intensity and caused a change in its temperature dependence. These changes are similar to those observed for iron and manganese doped samples and may be attributed to a fast non-radiative recombination path competing with the luminescent transition.

Thermoluminescence experiments showed the presence of four traps. Three of these had been observed in undoped and manganese doped rutile, the fourth in iron doped rutile. The low level of the thermoluminescence made analysis of the peaks impossible but activation energies could be inferred from the results obtained from the other dopants.

CHAPTER 10

NICKEL DOPED CRYSTALS

- 10.1 Introduction
- 10.2 Photoluminescence
- 10.3 Thermoluminescence
- 10.4 Summary

10.1 INTRODUCTION

A sample doped with nickel was studied by photoluminescence and thermoluminescence. The doping had been carried out by diffusion at 1050°C for 24 hours followed by an anneal in oxygen at 1000°C for 24 hours.

10.2 PHOTOLUMINESCENCE

The photoluminescence emission from nickel doped rutile showed the same broad band centred on 860 nm that was observed from undoped samples. The emission intensity was similar to that from undoped samples.

The temperature dependence of the photoluminescence emission intensity under constant illumination is shown in figure 10.2.1. It can be seen that the intensity increases with increasing temperature up to a maximum at about 190 K and then decreases rapidly at higher temperatures. This behaviour is typical of that seen for undoped and chromium doped samples, although the reduction in intensity for temperatures below 190 K is more noticeable for the nickel doped sample. This could indicate an increase in the number of shallow traps causing a reduction in luminescence efficiency by Auger recombination.

10.3 THERMOLUMINESCENCE

TSL experiments were carried out on the nickel doped single crystal rutile and a typical TSL spectrum is shown in figure 10.3.1. Four distinct peaks can be seen; these occur at 89, 102, 118 and 166 K, with the peak at 166 K being considerably higher than the others (note the change in scale of the vertical axis at 136 K). A shoulder can be seen on the high temperature side of this main peak and above 240 K the thermoluminescence starts to increase without peaking.

The peak at 166 K is of a comparable height to that in TSL spectra from

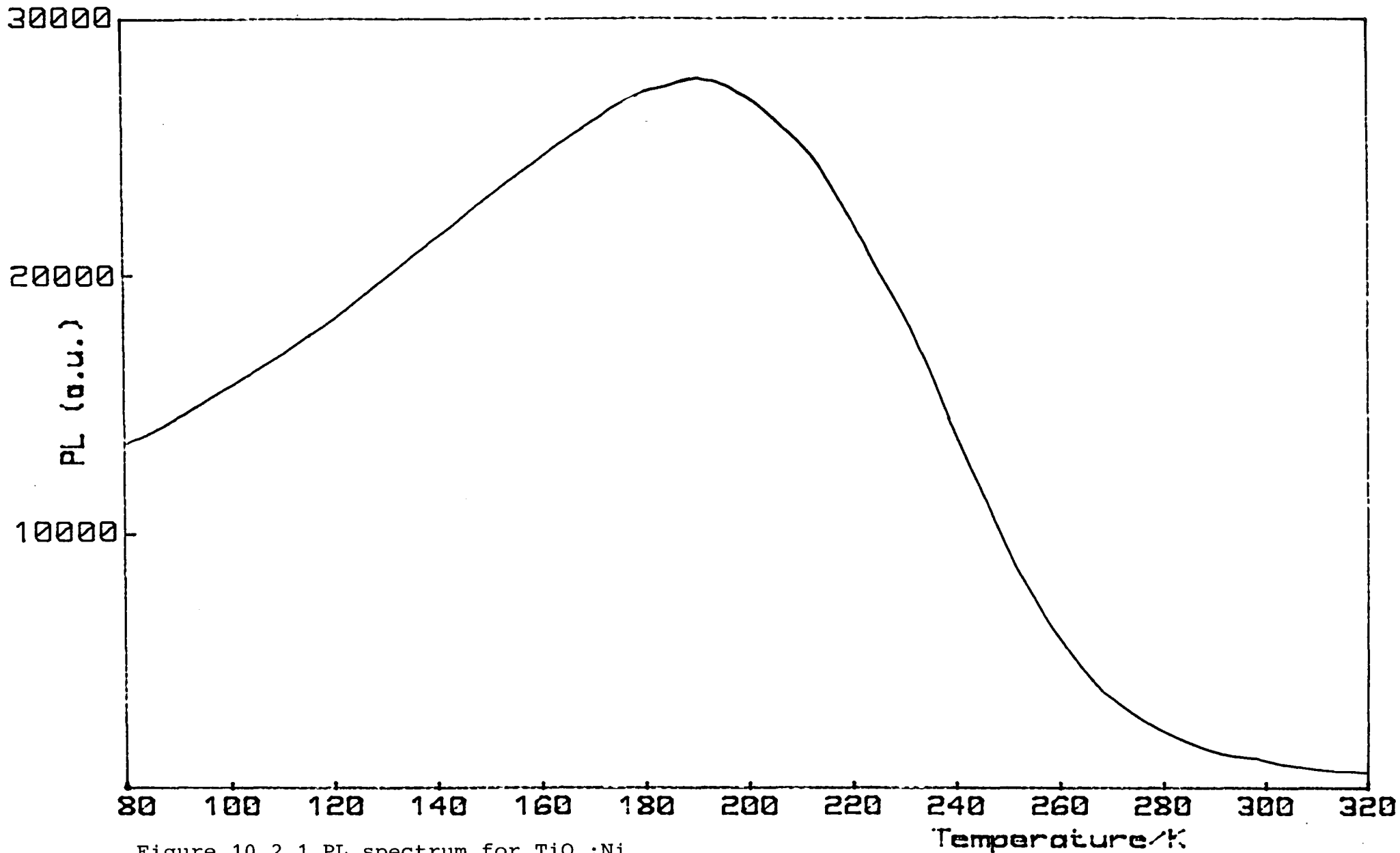
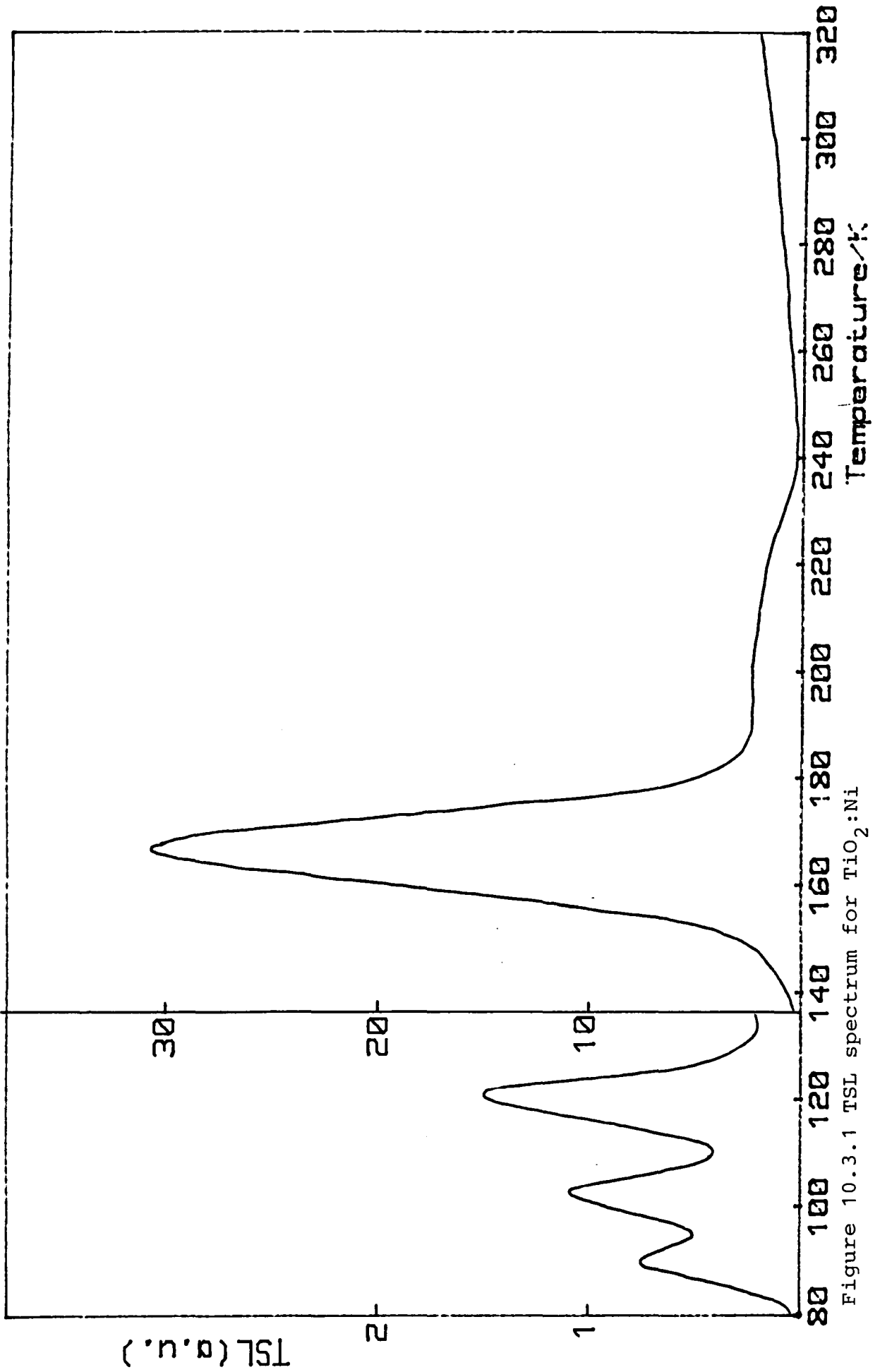


Figure 10.2.1 PL spectrum for $\text{TiO}_2:\text{Ni}$

Figure 10.3.1 TSL spectrum for $\text{TiO}_2:\text{Ni}$

undoped rutile and also yielded a value of 0.37 ± 0.03 eV for the activation energy. The low level of the thermoluminescence for the peaks between 80 and 140 K precluded determination of their activation energies. However, the peaks at 102 and 118 K correspond to peaks observed in spectra from undoped, manganese doped and cobalt doped samples and can be inferred to be the same. The peak at 88 K was not seen in spectra from any other crystals and seems, therefore, to be associated with nickel. The shoulder on the high temperature side of the main peak is possibly caused by an overlap of the peaks at 200 and 220 K which have been observed in chromium and iron doped samples. The low level of the thermoluminescence prevented thermal cleaning and further analysis of this temperature range.

Hillhouse [10] has reported TSL spectra from nickel doped rutile showing seven peaks which included the four described here plus others at 230, 300 and 330 K. He determined a value of 0.16 ± 0.2 eV for the peak at 88 K which compares with the values of 0.15 eV and 0.22 eV for the peaks at 100 K and 120 K determined from other dopants.

10.4 SUMMARY

Nickel doped samples were studied by photoluminescence and thermoluminescence.

After nickel doping both the intensity of the photoluminescence and its temperature dependence remained similar to undoped material.

Thermoluminescence experiments showed the presence of four traps, of which the one occurring at 89 K had not been observed in spectra from any other crystals.

CHAPTER 11

NIOBIUM DOPED CRYSTALS

- 11.1 Introduction
- 11.2 Material preparation
- 11.3 Capacitance-voltage measurements
- 11.4 Current-voltage measurements
- 11.5 Deep level transient spectroscopy
- 11.6 Summary

11.1 INTRODUCTION

Normally, rutile is too resistive for techniques such as deep level transient spectroscopy to be applied. Rutile is changed to an n-type semiconductor when reduced, because point defects due to the reduction act as donor centres. It is well known that rutile doped with elements from groups V and VI of the periodic table has semiconducting properties. Bogoroditskii et al [39] have studied the electrical properties of doped Verneuil grown crystals and shown that the niobium increases the conductivity. They also concluded that the semiconducting properties of rutile induced by doping are much more stable towards changes in oxygen pressure at elevated temperatures than those of reduced rutile.

Results of measurements on reduced rutile have been described in chapter 5; results for niobium doped rutile are given in this chapter.

11.2 MATERIAL PREPARATION

The niobium doped sample came from a boule grown by the plasma method and doped during growth by including a measured quantity of niobium oxide (Nb_2O_5) with the sandy rutile source material [10]. The as grown crystal was opaque and deep blue-black in colour and was not subjected to any post-growth oxidation. Solid source mass spectroscopy indicated the doping concentration of niobium to be about 140 at ppm.

A sample was cut from the boule in the shape of a rectangular prism with dimensions $4 \times 3 \times 1 \text{ mm}^3$ and with the large face perpendicular to the c-axis. The procedure for making contacts and mounting the sample in the cryostat to make measurements has been described in chapter 4. A rectifying contact was provided by a gold dot evaporated onto one face and a silver dot on the opposite face gave an injecting contact.

11.3 CAPACITANCE-VOLTAGE MEASUREMENTS

The capacitance of the gold- rutile Schottky diode was measured as a function of reverse bias and the result is shown in figure 11.3.1 as a plot of $1/C^2$ versus V . The slope of the line enables the ionised donor density to be calculated and this yields a value of $2.3 \times 10^{16} \text{ cm}^{-3}$. Taking a value of $1.0 \text{ cm}^2 \text{ V}^{-1} \text{ s}^{-1}$ for the mobility parallel to the c -axis this indicates a resistivity of $270 \text{ } \Omega \text{ cm}$. This is considerably higher than the value of $4.8 \text{ k}\Omega \text{ cm}$ obtained for the reduced rutile diode described in chapter 5 which had an ionised donor concentration of $1.3 \times 10^{15} \text{ cm}^{-3}$. The intercept of the line on the voltage axis yields a value of 0.68 V for the built-in voltage of the diode. This is much larger than the value of 0.3 V obtained from the measurements on the reduced rutile diode.

11.4 CURRENT-VOLTAGE MEASUREMENTS

The current-voltage characteristics of the gold - niobium doped rutile diode were measured under both forward and reverse bias. Figure 11.4.1 shows the results plotted on logarithmic scales. It can be seen that, in reverse bias, the current is ohmic up to an applied bias of 1.0 V after which the current becomes superlinear. When forward biased the current is ohmic up to an applied bias of 0.27 V when the current starts to increase rapidly with further applied bias. The current exhibits the same type of space charge limited (SCL) behaviour that was observed in the reduced rutile diode. In this case the current is proportional to V^2 for $0.27 < V < 0.46$, proportional to V^4 for $0.46 < V < 0.95$ and proportional to V^2 for applied biases greater than 0.95 V . As described in section 5.5 on reduced rutile, Roberts et al [159] have modified the Mott and Gurney [82] relationship between current, voltage and thickness in a trap free insulator to give this expression for a SCL current:

$$J = 9\theta \epsilon_r \epsilon_0 \mu V^2 / (8W^3) \quad (11.1)$$

where θ is the fraction of total carriers which are free.

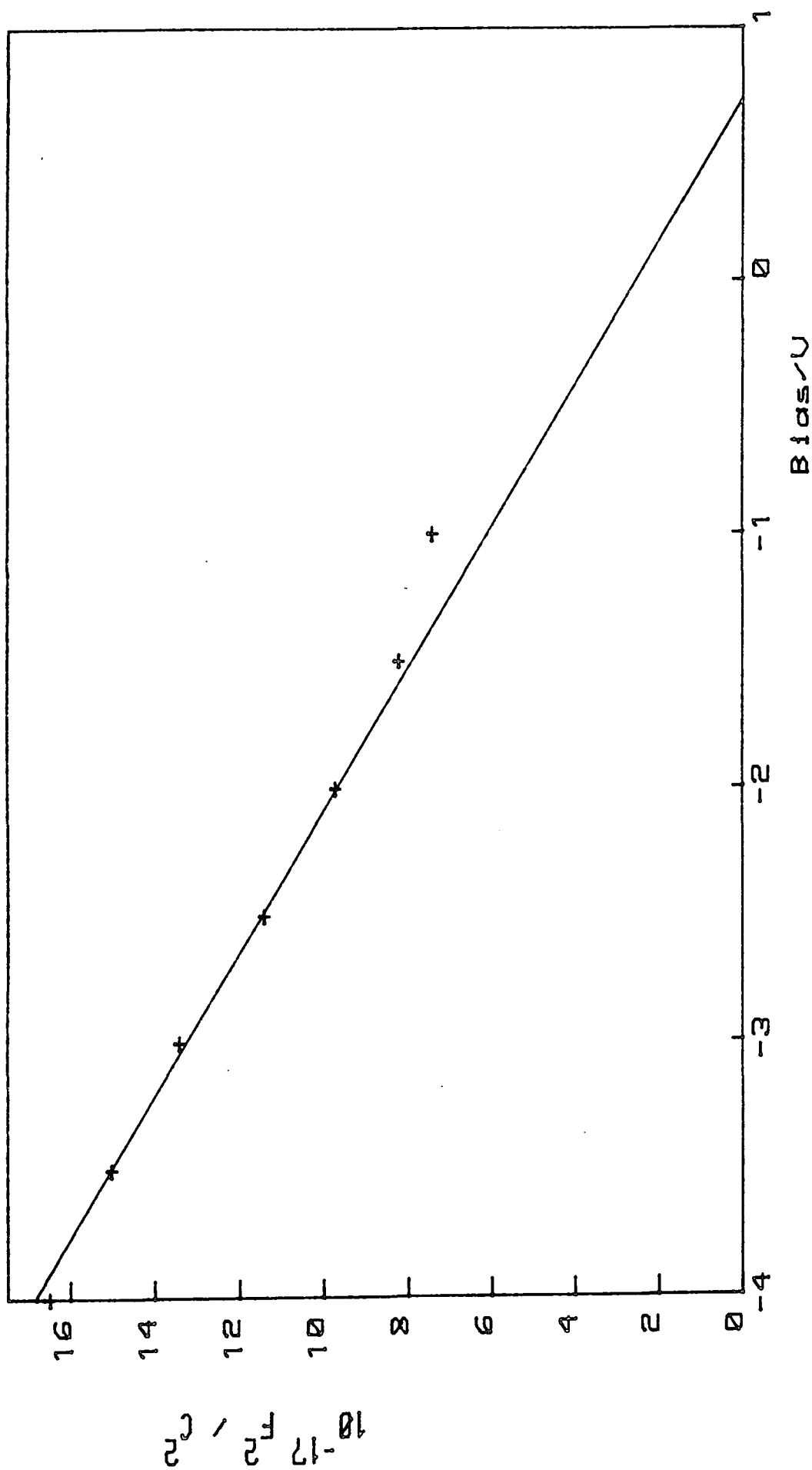


Figure 11.3.1 C-V plot for niobium doped diode

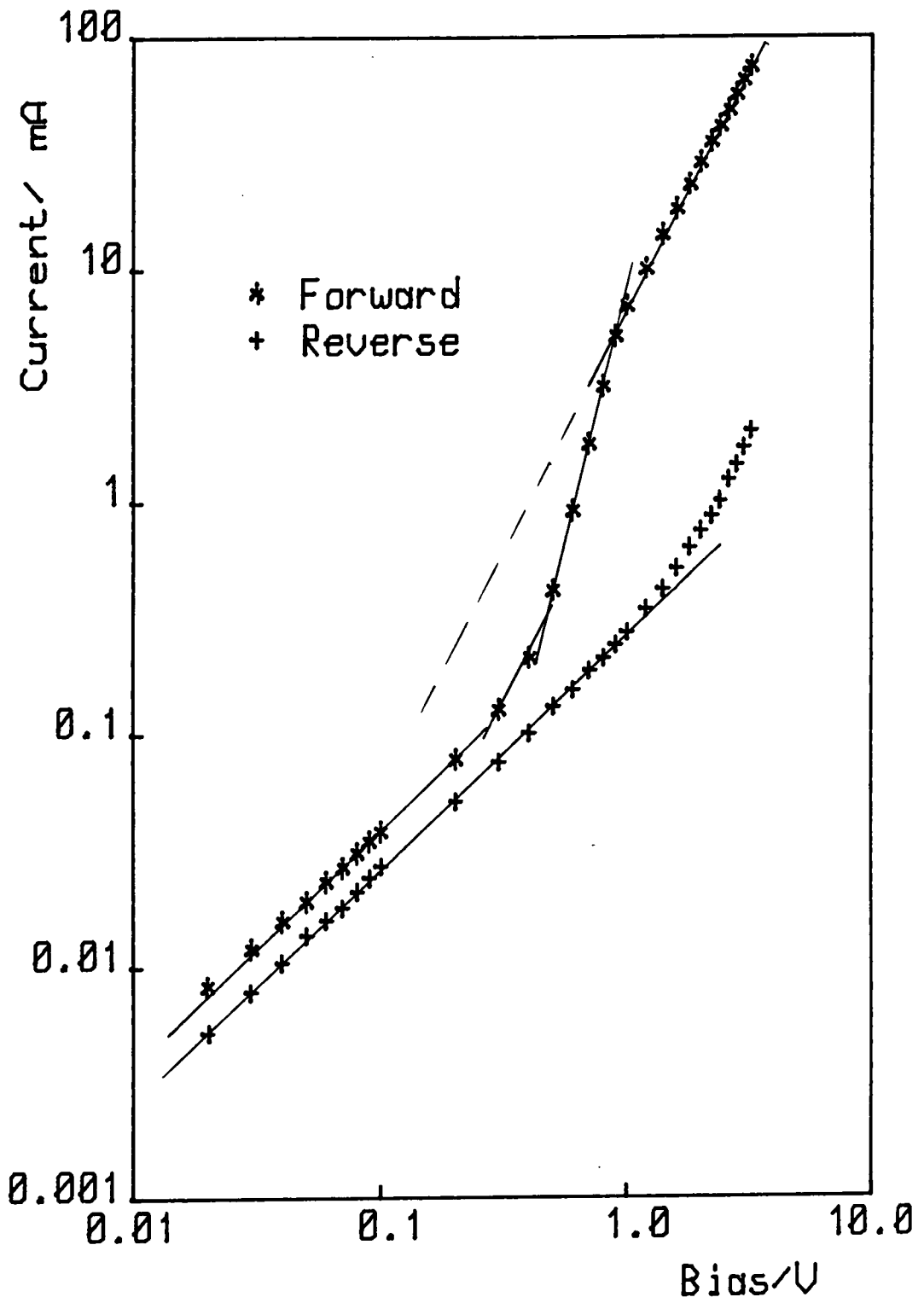


Figure 11.4.1 I-V characteristics for niobium doped diode

A value for θ may be estimated by extrapolating the two regions where $I \propto V^2$ and taking their ratio, since in the upper region the physical situation resembles a trap free solid with $\theta = 1$. In the present case this yields a value of $\theta = 0.2$. To apply the theoretical SCL expression to the regions where $I \propto V^2$ would require a value of $\mu\epsilon_r$ equal to $1.8 \times 10^{10} \text{ cm}^2 \text{ V}^{-1} \text{ s}^{-1}$ to achieve the measured current density. With a value for ϵ_r of 170 [160], this would imply a mobility of $10^8 \text{ cm}^2 \text{ V}^{-1} \text{ s}^{-1}$. Clearly, the one carrier injection space charge limited conduction mechanism does not adequately describe the forward bias conduction of this device and another explanation such as two carrier injection [174], contact emission kinetics [156] or high energy band conduction [43] must be sought.

11.5 DEEP LEVEL TRANSIENT SPECTROSCOPY

DLTS spectra were obtained over the temperature range 80 to 300 K by cooling the sample with liquid nitrogen. The liquid nitrogen was allowed to evaporate and the sample slowly returned to room temperature. The output from the thermocouple touching the sample was used to drive the X-axis of an X-Y chart recorder and the DLTS signal was recorded on the Y-axis. Spectra were recorded for rate windows of 6, 18, 55 and 182 s^{-1} and these are shown in figure 11.5.1. It can be seen that each spectrum shows a single dominant maximum occurring between 200 and 250 K depending on the rate window. There also appeared to be a small feature on the low temperature side of the main DLTS peak.

The activation energy of the main peak could be determined by plotting $\ln(T_m^2 \tau)$ against $1/T_m$, where $\tau = (t_1 - t_2) / \ln(t_1/t_2)$ and t_1 and t_2 are the times after the pulse of the sampling gates defining the rate window. This procedure should yield a straight line with slope E/k . The plot for the spectra shown in figure 11.5.1 is given in figure 11.5.2. It can be seen that this gives an excellent straight line, yielding a value of 0.38 eV for the activation energy. The intercept on the $\ln(T_m^2 \tau)$ axis gives an estimate of the capture cross-section

DLTS Signal

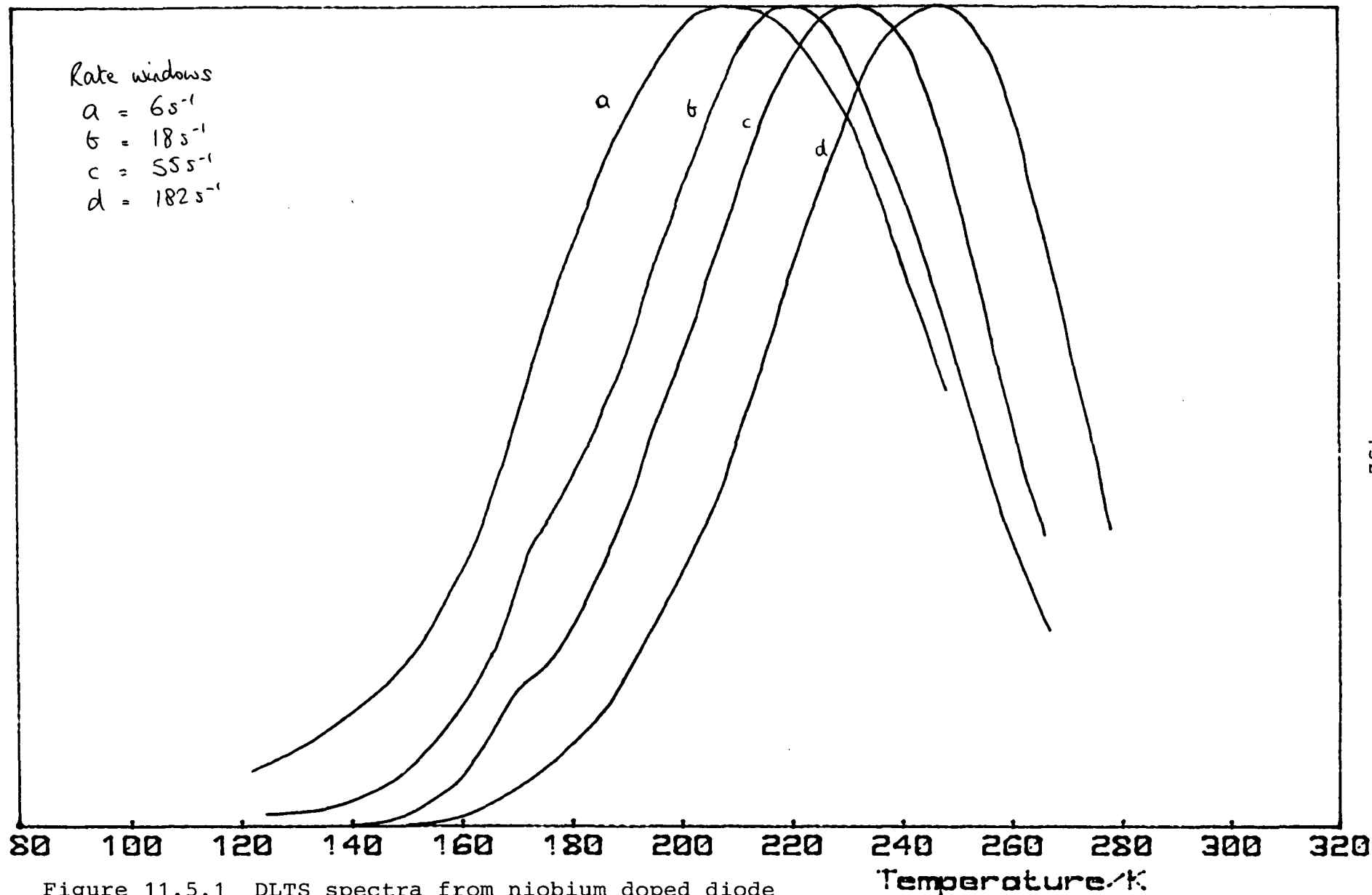


Figure 11.5.1 DLTS spectra from niobium doped diode

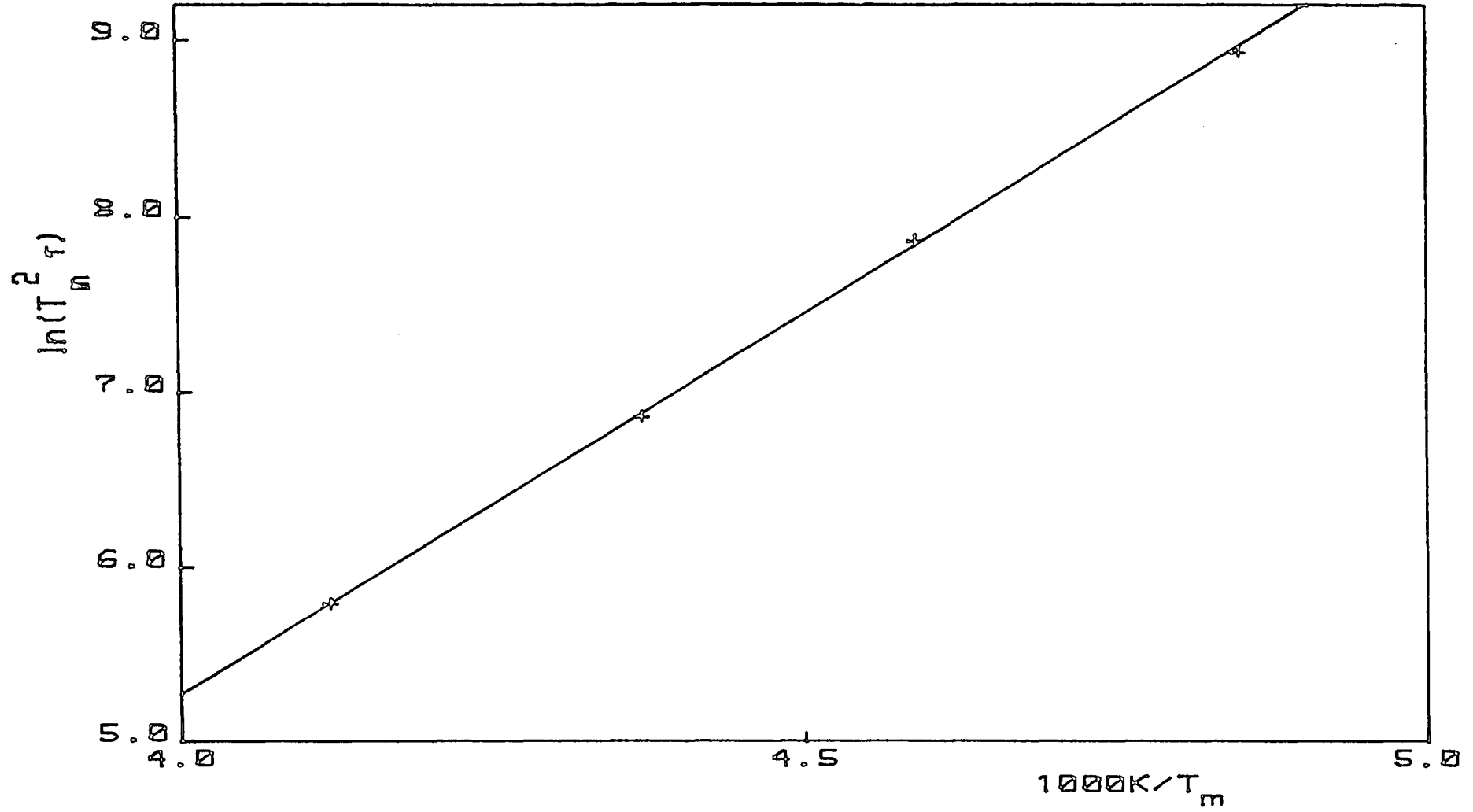


Figure 11.5.2 Arrhenius plot for DLTS spectra of figure 11.5.1

of $7 \times 10^{-18} \text{ cm}^2$ using a value of $8 m_0$ for the polaronic effective mass.

It was not possible to analyse the small feature on the low temperature side of the main peak because of the proximity of the dominant maximum.

Niobium doped rutile has been studied by Hillhouse [10] using a combination of photoluminescence and thermoluminescence. He found one main electron trap situated 0.37 eV below the conduction band edge and two additional traps of minor importance at energies of 0.13 and 0.51 eV. These three traps have also been observed in both doped and undoped rutile as discussed in the previous chapters. There is clearly excellent agreement between the activation energy of the dominant DLTS level and the dominant thermoluminescence peak. The value obtained for the capture cross-section is also very close to the value of 10^{-17} cm^2 obtained from the TSL peak. The 0.13 eV level may correspond to the small feature on the low temperature side of the main DLTS maximum. The 0.51 eV level would probably give rise to a peak above the maximum temperature of the DLTS spectrum and so would not have been observed.

11.6 SUMMARY

The properties of gold - niobium doped rutile Schottky diodes have been studied. The presence of a bias dependent depletion layer was shown by capacitance-voltage measurements. Current-voltage measurements showed rectifying characteristics and forward biased conduction typical of space charge limited mechanisms. The one carrier injection space charge limited conduction expression could not adequately describe the characteristics without requiring a very high mobility.

DLTS spectra showed one dominant maximum. The variation of peak temperature with rate window gave an activation energy of 0.38 eV and a capture cross-section of $7 \times 10^{-18} \text{ cm}^2$. The agreement between these values and the values of 0.37 eV and 10^{-17} cm^2 for the dominant thermoluminescence peak

suggests that the simple insulator model for thermoluminescence applies well in rutile. This confirms the conclusions of Hillhouse and Woods [149]. The DLTS result allows the results for trap depths derived from TSL measurements to be viewed with some confidence.

CHAPTER 12

POWDERS

- 12.1 Introduction
- 12.2 Material preparation
- 12.3 Photoluminescence
- 12.4 Thermoluminescence
- 12.5 Thermally stimulated conductivity
- 12.6 Summary

12.1 INTRODUCTION

Rutile powders have wide ranging uses as pigments and the understanding of their photoelectronic properties is, therefore, important. Several trapping centres have been observed in the work on rutile crystals; powder samples were studied in an attempt to identify whether the same centers were present and establish whether studies of single crystal rutile could be applied to powders. Samples of undoped, chromium doped and iron doped powders were studied by the methods of photoluminescence, thermoluminescence and thermally stimulated conductivity.

12.2 MATERIAL PREPARATION

A supply of undoped rutile powders was available and from this powders doped with up to 313 ppm chromium and 405 ppm iron were made. Two methods of mounting the powders were used. The first involved pressing pellets of powder and then furnacing these to produce ceramic discs. The second method was to make up a powder-binder mixture which was painted onto glass slides. The details of the doping and mounting have been given in chapter 4.

12.3 PHOTOLUMINESCENCE

The temperature dependence of the photoluminescence was measured for sintered pellets of undoped powder and powders doped with 48, 95, 225 and 313 ppm chromium and 35, 70, 135 and 405 ppm iron.

The temperature dependence of the photoluminescence of the undoped pellet is shown in figure 12.3.1. It can be seen that the intensity rises to a maximum at about 200 K and then decreases rapidly. This behaviour is typical of that observed for undoped and chromium doped crystals as described in chapters 5 and 6. Taking the luminescence efficiency, η to be 1 at 200 K enables a plot of $\ln((1-\eta)/\eta)$ versus

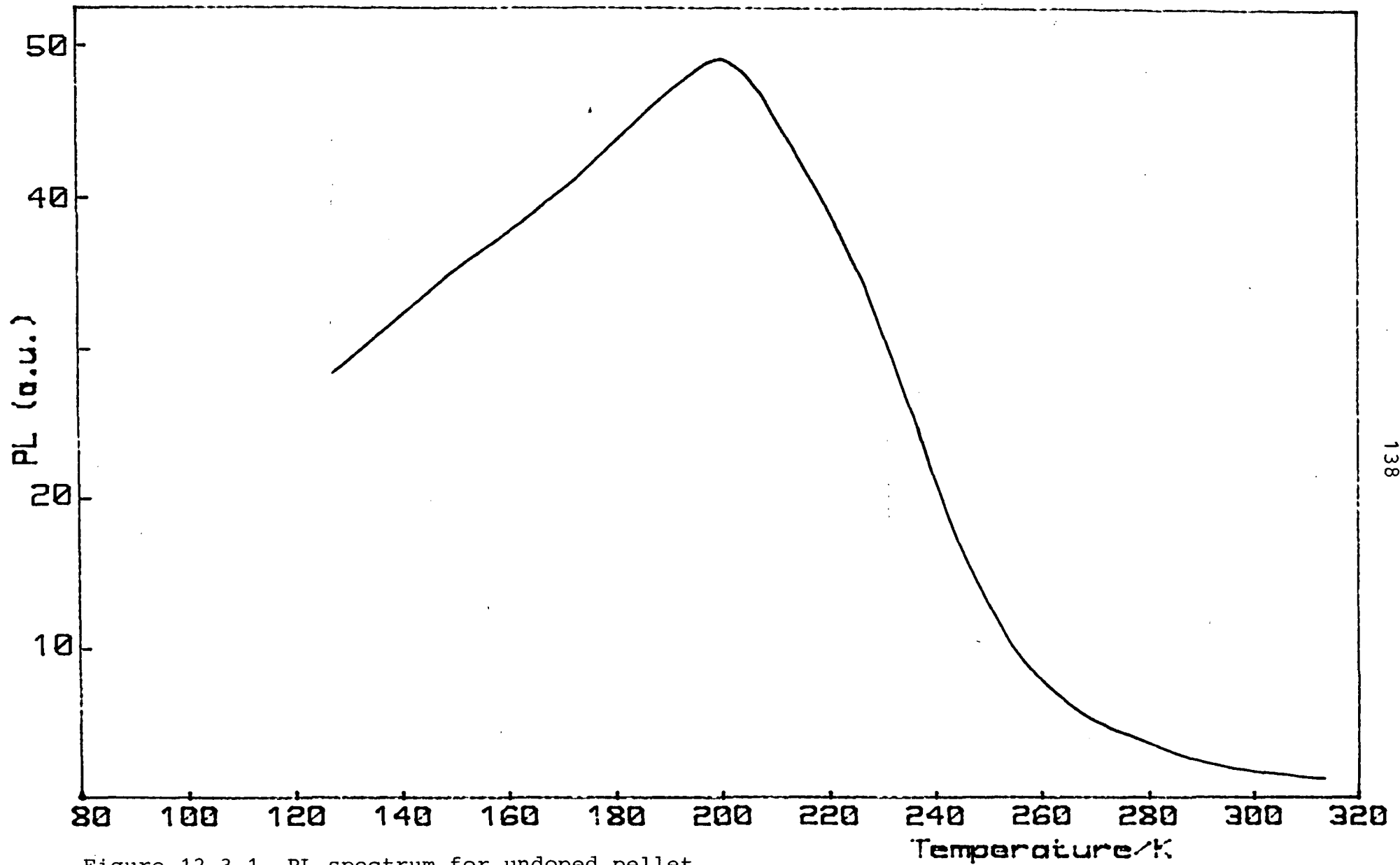


Figure 12.3.1 PL spectrum for undoped pellet

1/T to be made. This is shown in figure 12.3.2. The slope of the straight line gives an activation energy for the thermal quenching of the luminescence of 0.36 ± 0.02 eV.

Figure 12.3.3 shows the photoluminescence intensity as a function of temperature for the chromium doped sintered pellets. These all show similar behaviour to the undoped pellet with the luminescence increasing and then falling rapidly although, for these samples, the maximum intensity occurs at about 180 K. The results clearly show an increase in luminescence with chromium doping and this gives support for attributing the luminescence in rutile to chromium. Plots of $\ln((1-\eta)/\eta)$ versus 1/T for the chromium doped pellets are shown in figure 12.3.4. It can be seen that the points are almost coincident and the line yields a value of 0.29 ± 0.02 eV for the activation energy of thermal quenching of the luminescence.

Figure 12.3.5 shows the photoluminescence intensity as a function of temperature for the iron doped sintered pellets. It can be seen that increasing the iron content reduces the intensity of the photoluminescence and that the form of the temperature dependence changes. The curve for 35 ppm iron shows an increase to a maximum at about 190 K followed by a sharp decrease; this behaviour is similar to that described above for undoped and chromium doped samples. The curves for 135 and 405 ppm iron decrease monotonically with increasing temperature; this behaviour is similar to that described in chapter 7 for iron doped single crystals. The curve for 70 ppm iron shows behaviour intermediate between these two extremes. It was proposed in chapter 7 that iron provides a fast non-radiative recombination path that competes with the chromium luminescent recombination. The results shown here support that proposal. Plots of $\ln((1-\eta)/\eta)$ versus 1/T for the iron doped pellets are shown in figure 12.3.6. It can be seen that a straight line is only obtained for the 35 ppm sample which yields an activation energy of $0.32 \pm$ eV. The more highly doped samples do not show straight lines. For these samples it is almost certainly incorrect to assume that $\eta = 1$ at the maximum luminescence intensity. This leads to an error in determining $(1-\eta)/\eta$.

As a check that the furnacing of the samples to produce the sintered pellets had

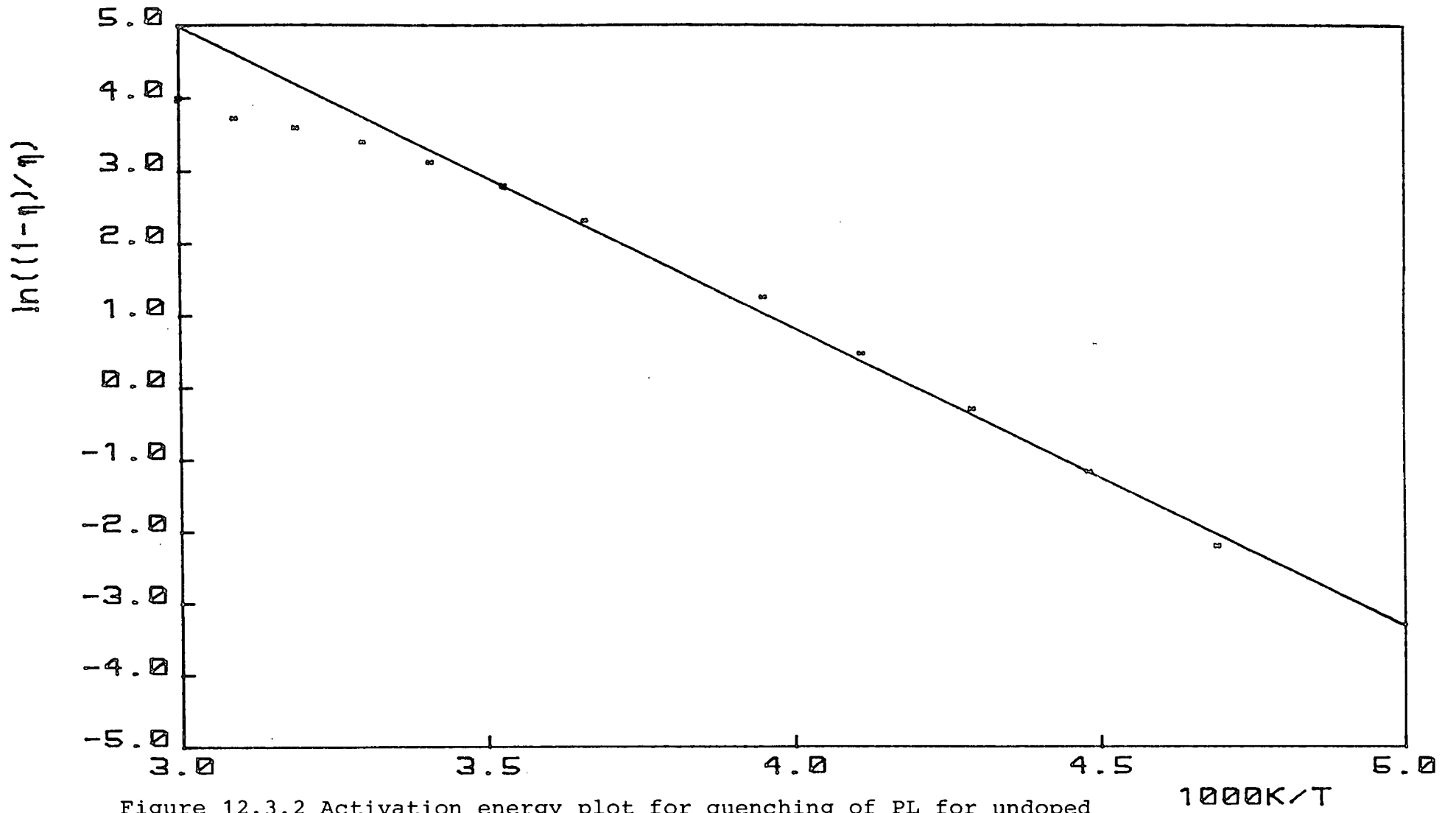


Figure 12.3.2 Activation energy plot for quenching of PL for undoped pellet

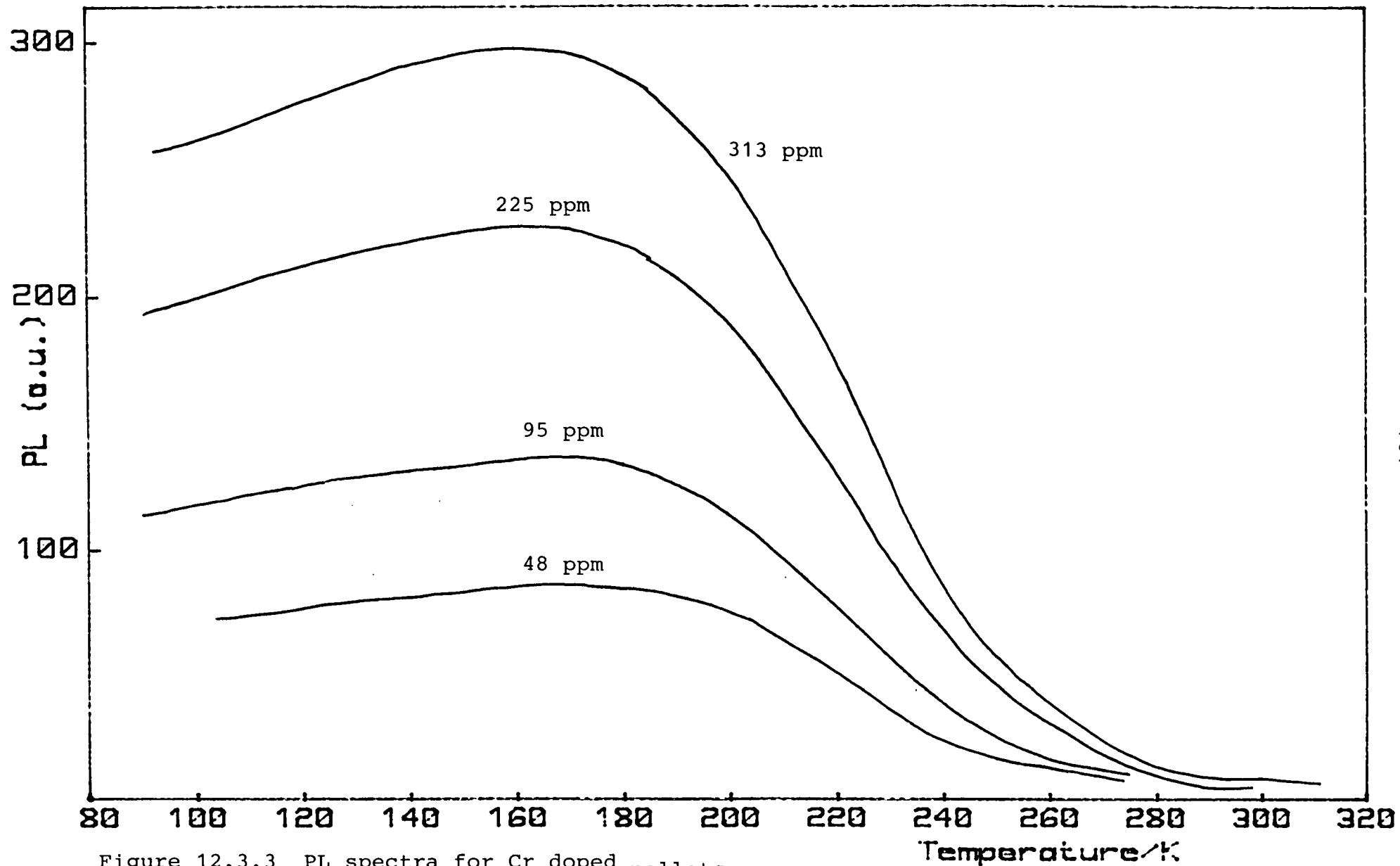


Figure 12.3.3 PL spectra for Cr doped pellets

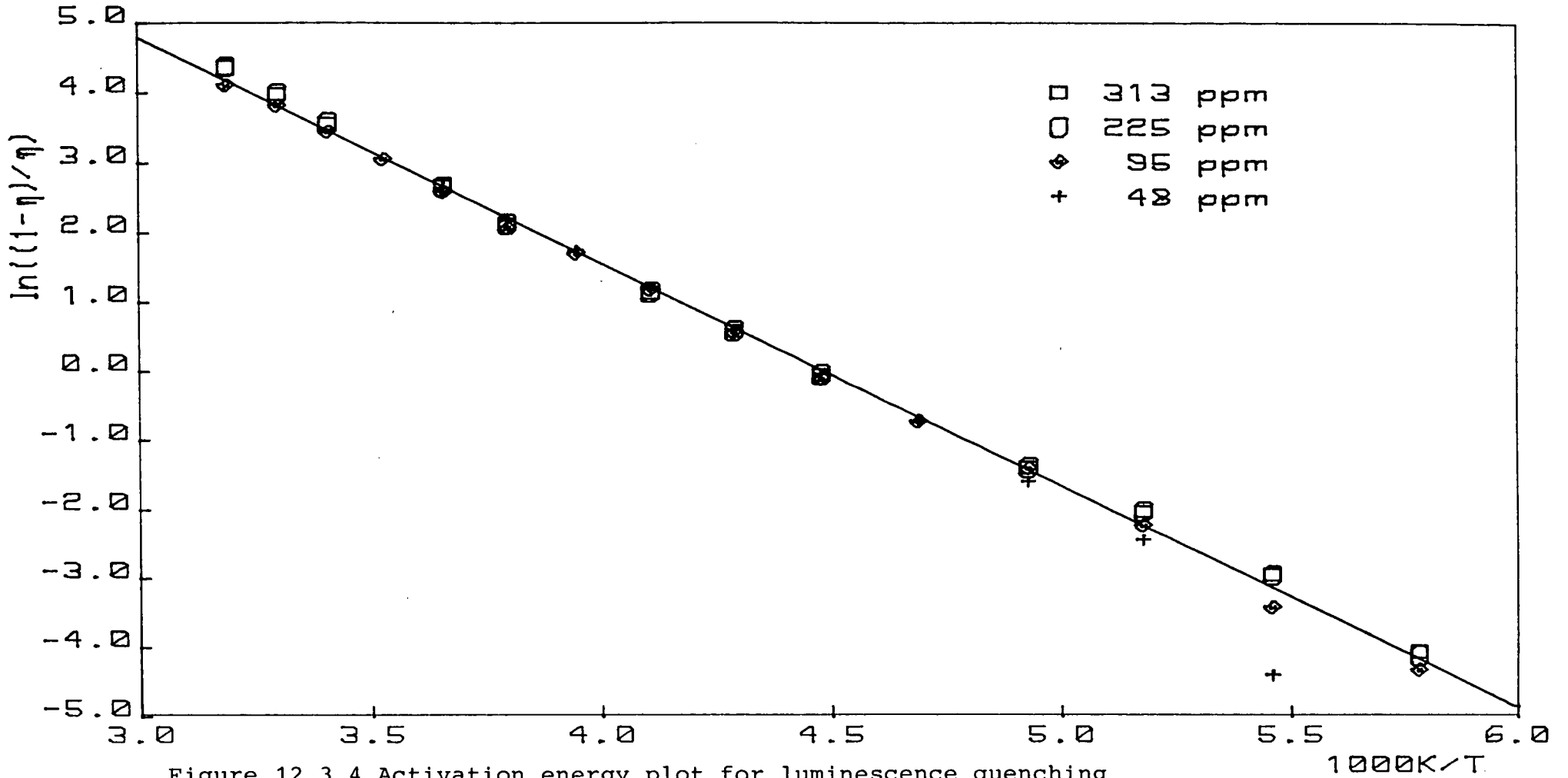


Figure 12.3.4 Activation energy plot for luminescence quenching of Cr doped pellets

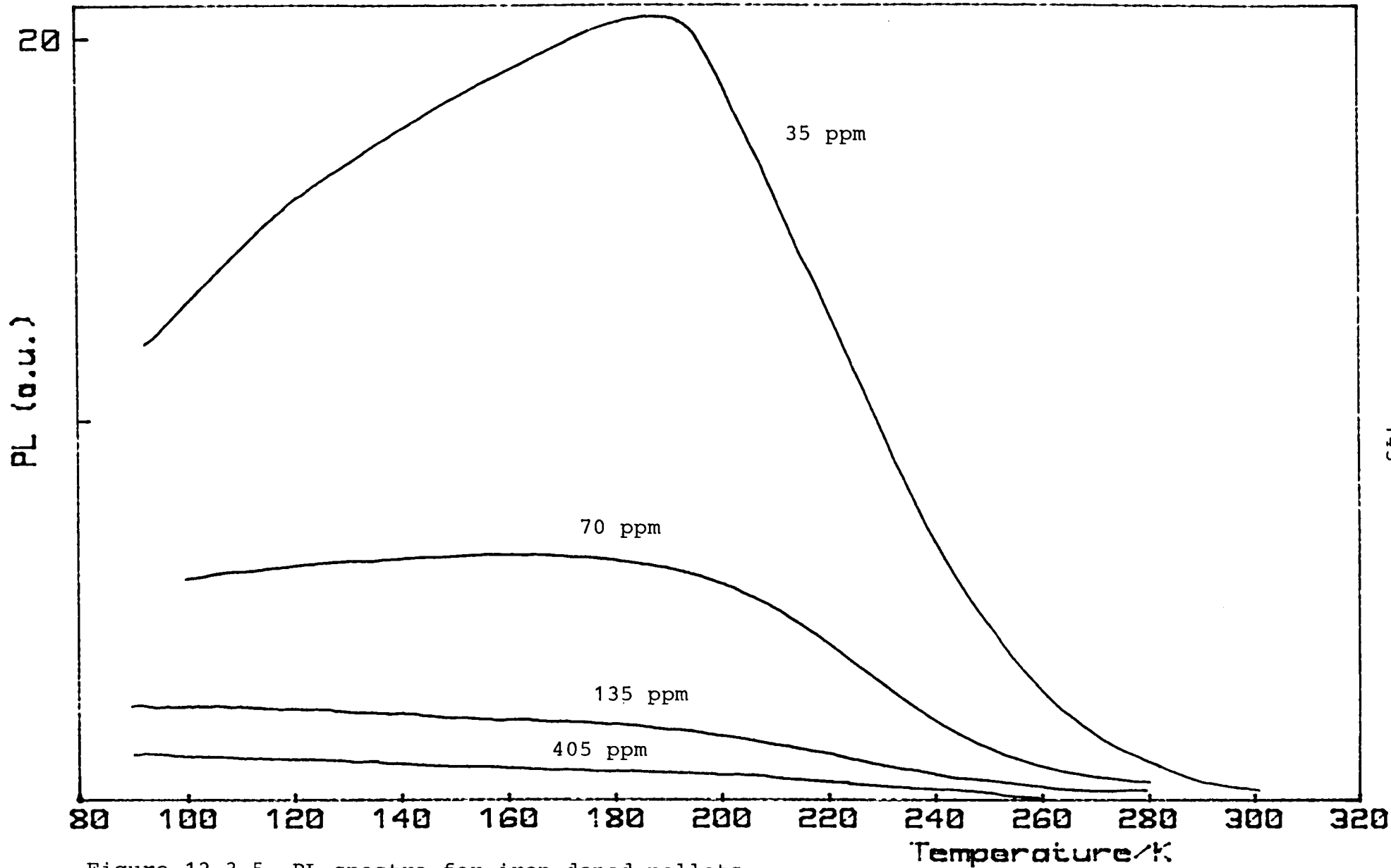


Figure 12.3.5 PL spectra for iron doped pellets

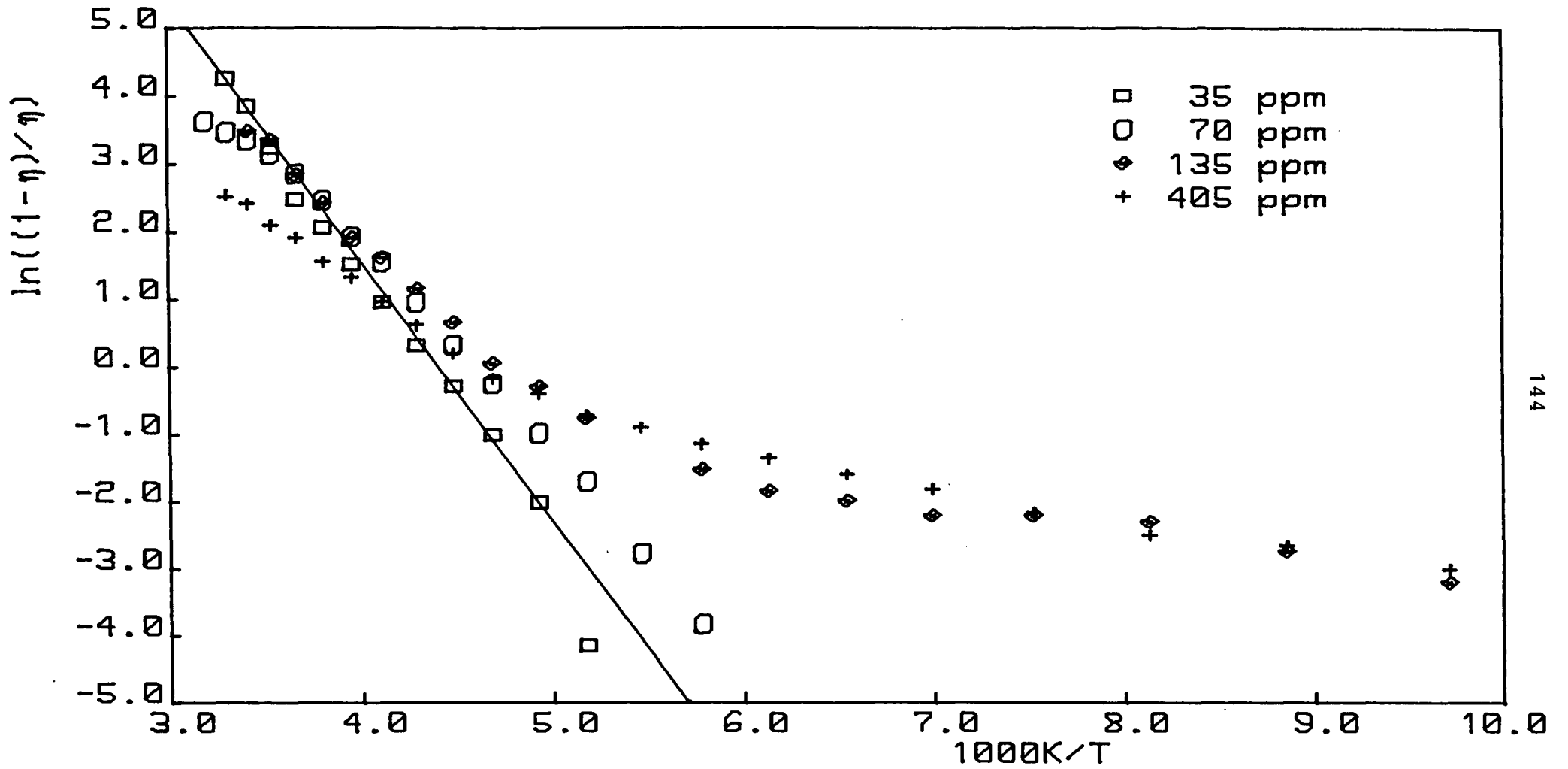


Figure 12.3.6 Activation energy plots for the thermal quenching of luminescence Fe doped pellets

not affected the results, some of the chromium doped powders were mixed with a 5% solution of nitrocellulose in butyl acetate and the mixture painted onto glass slides. The photoluminescence versus temperature results are shown in figure 12.3.7. By comparing these with the results for the sintered pellets in figure 12.3.3 it can be seen that the results are very similar, indicating that the furnacing had little effect on the photoluminescence. The powder-binder method has the advantage of simplicity over the sintered pellet method but can suffer from the disadvantages of poor reproducibility of film density and occasional problems of poor film adhesion to the glass slide.

12.4 THERMOLUMINESCENCE

Thermoluminescence spectra were measured for all the powders discussed in the previous section. A typical TSL spectrum for the undoped pellet is shown in figure 12.4.1 which shows a dominant peak at 175 K with shoulders on both the low and high temperature sides. Similar results were obtained from the chromium doped pellets as shown in figure 12.4.2 and the iron doped pellets as shown in figure 12.4.3. These figures show an increase in thermoluminescence peak height with increasing chromium content and a decrease in thermoluminescence peak height with increasing iron doping. Both these are consistent with the effect of doping on the photoluminescence intensity discussed in the previous section. The shoulder on the low temperature side of the main peak could be removed by thermal cleaning and the resulting spectrum for the 313 ppm chromium doped pellet is shown in figure 12.4.4. This peaks at 169 K and analysis yielded a value of 0.37 ± 0.03 eV for the activation energy. This is the same as the main peak found at about 169 K in all the crystal samples. It seems very likely that the spectra from powder pellets are made up from the same peaks that are seen in single crystal spectra.

Thermoluminescence spectra were measured from the chromium doped powder-binder mixtures; these are shown in figure 12.4.5. It can be seen that the

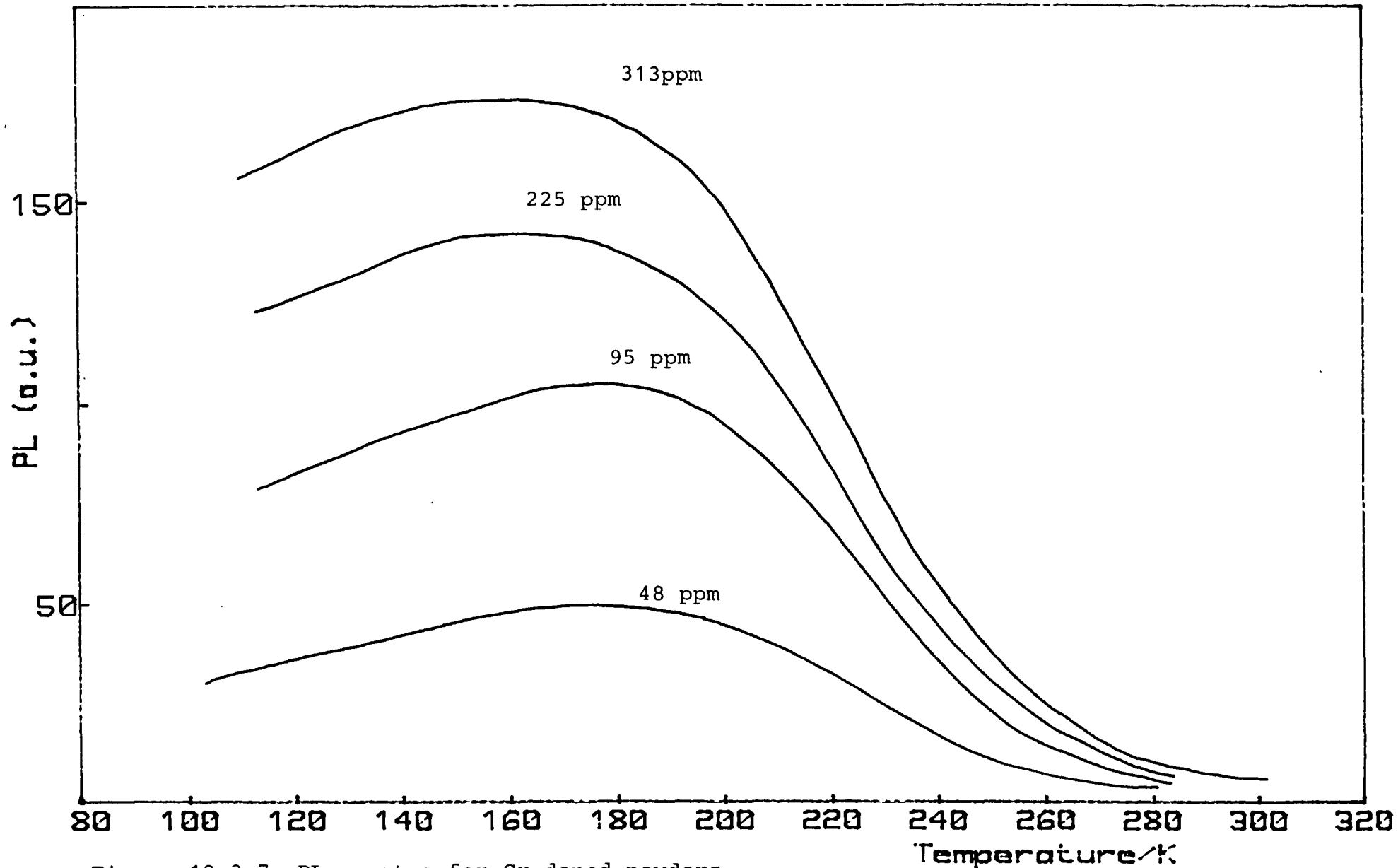


Figure 12.3.7 PL spectra for Cr doped powders

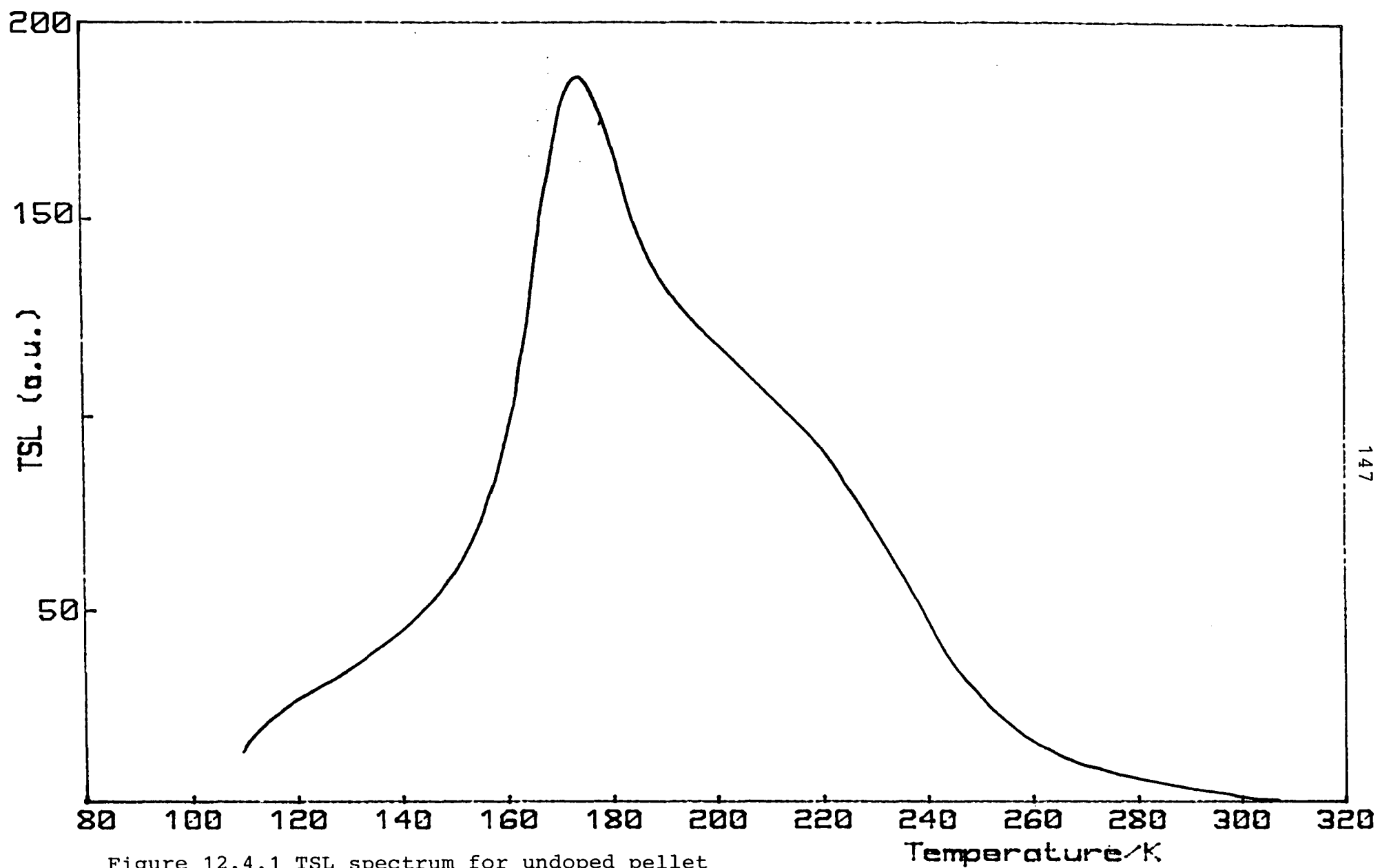


Figure 12.4.1 TSL spectrum for undoped pellet

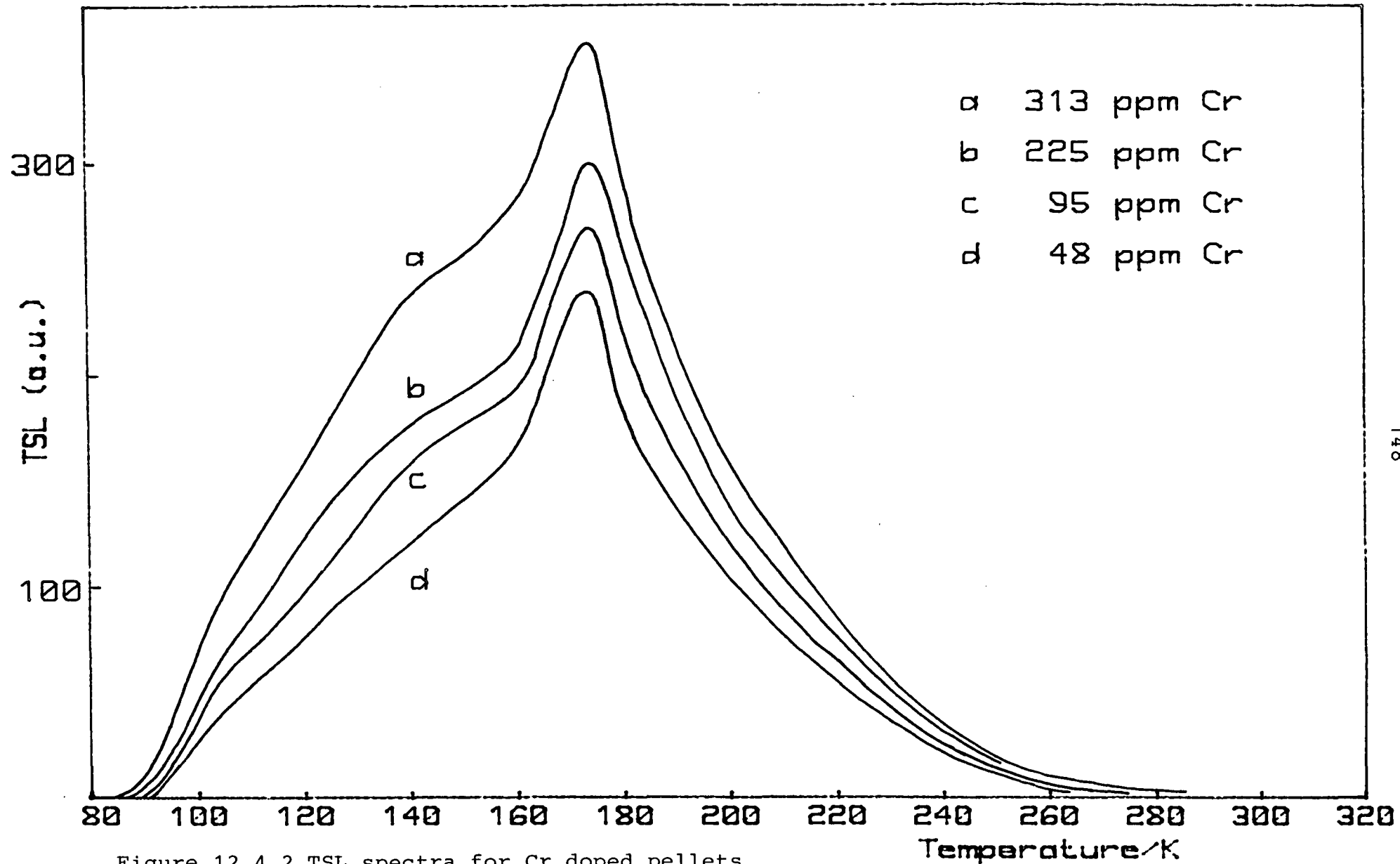


Figure 12.4.2 TSL spectra for Cr doped pellets

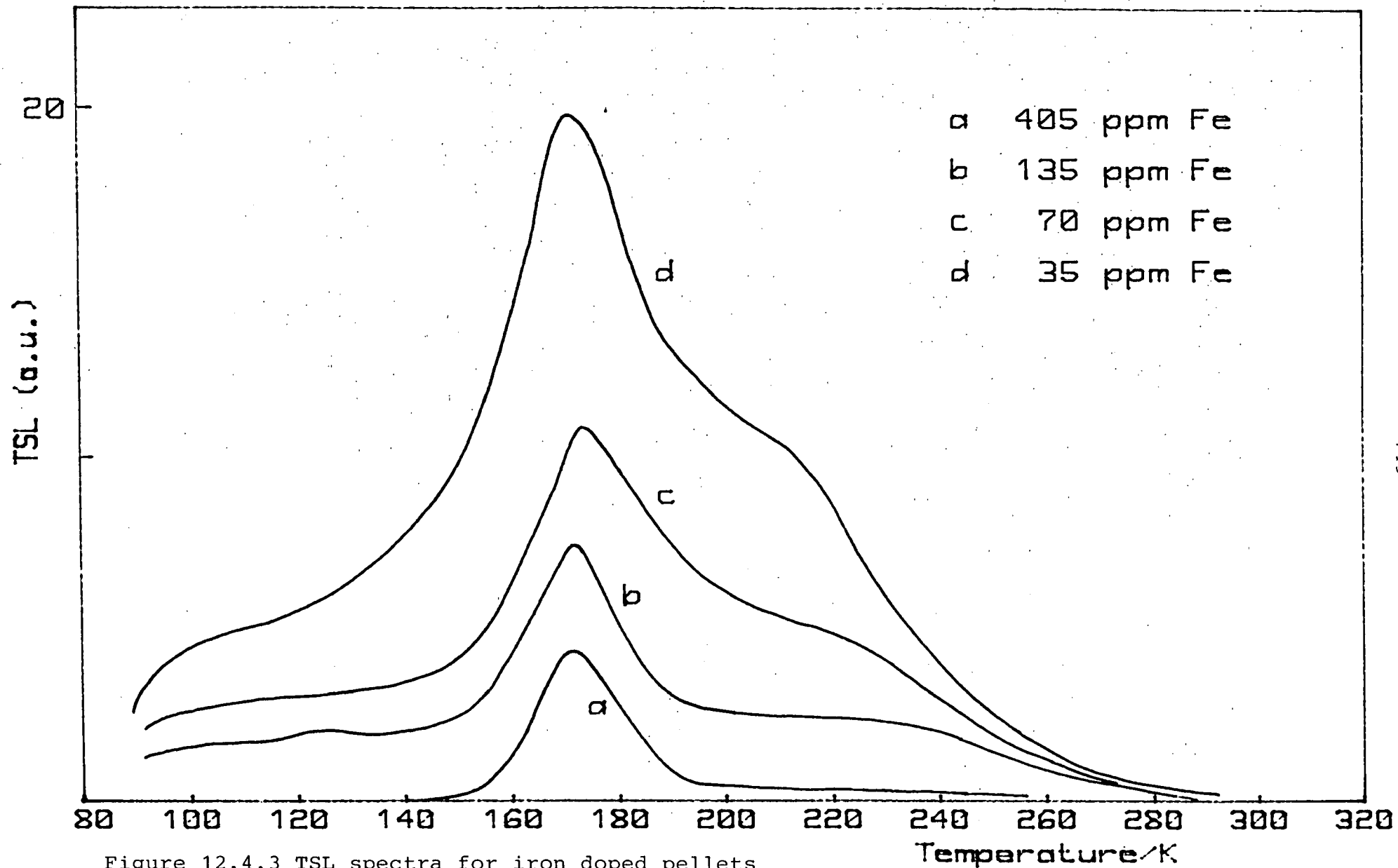


Figure 12.4.3 TSL spectra for iron doped pellets

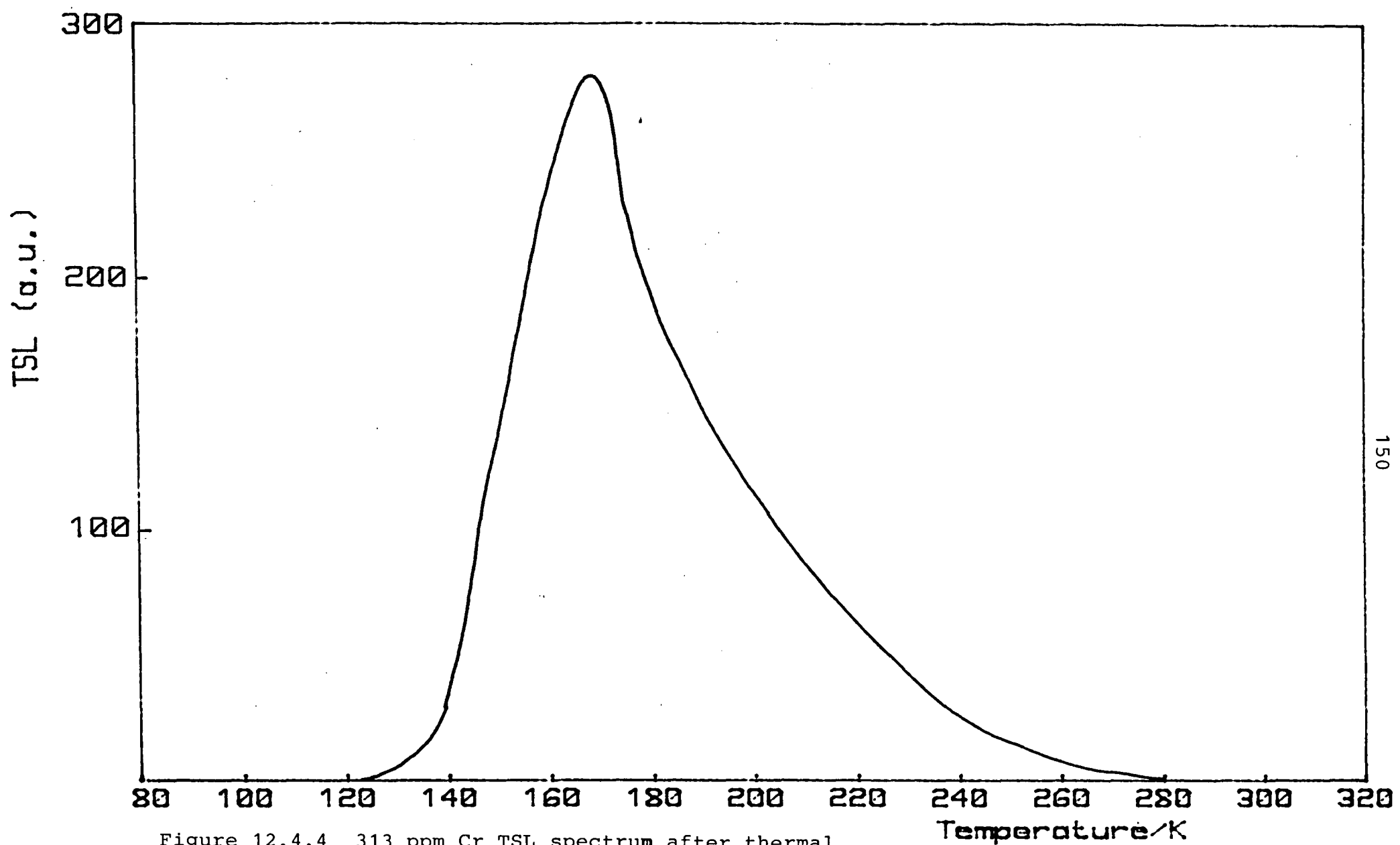


Figure 12.4.4 313 ppm Cr TSL spectrum after thermal cleaning to 160K

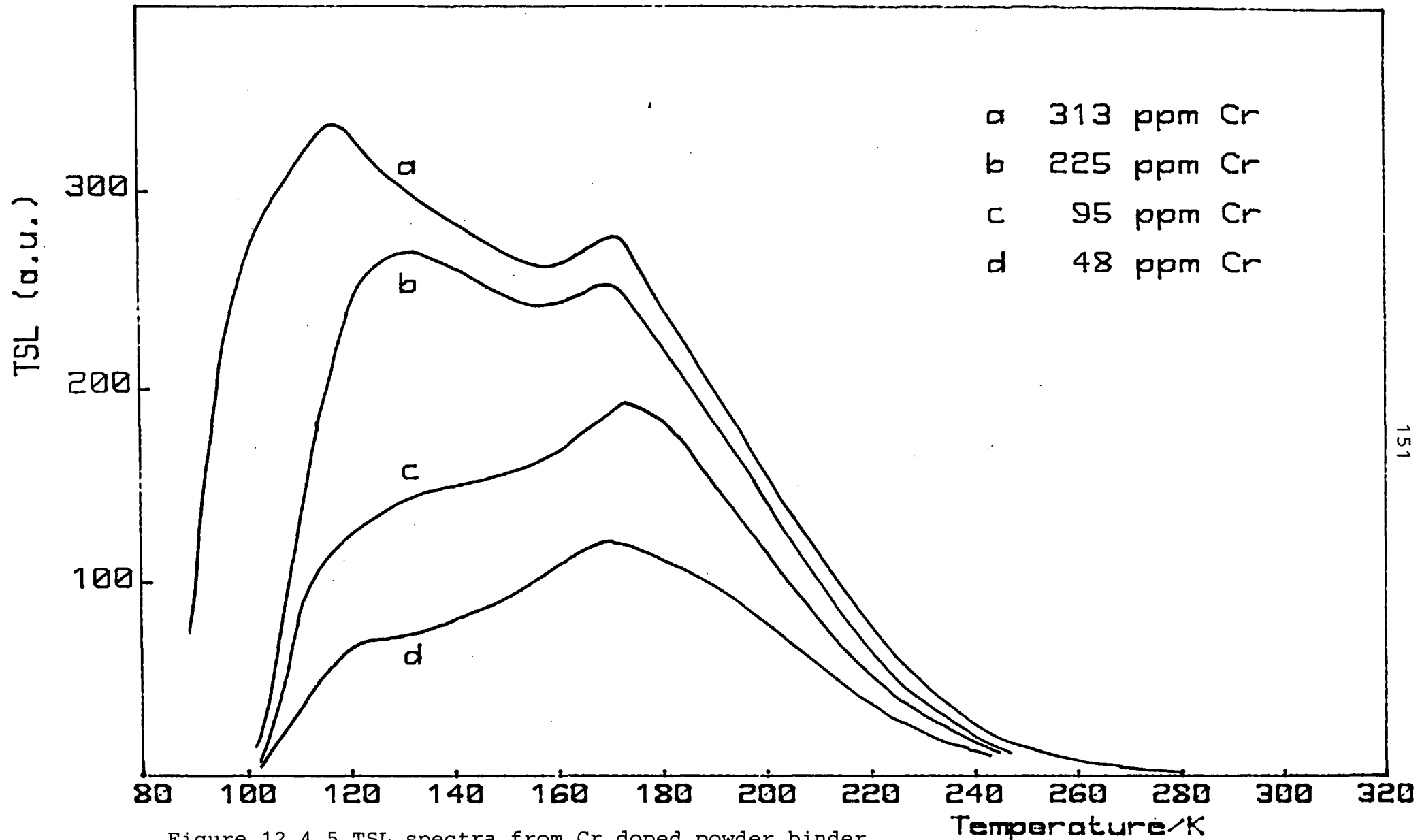


Figure 12.4.5 TSL spectra from Cr doped powder binder mixtures

relative magnitudes of the main peak and the low temperature shoulder have changed, with the shoulder becoming more pronounced with increasing doping. The conclusion that the spectrum is composed of overlapping peaks is supported by this observation.

12.5 THERMALLY STIMULATED CONDUCTIVITY

TSC spectra were obtained from all the sintered pellets discussed above. The spectrum from an undoped pellet is shown in figure 12.5.1, spectra from chromium doped pellets in figures 12.5.2-5 and spectra from iron doped pellets in figures 12.5.6-9. All the spectra show the same structure. No TSC was seen below 170 K and above 200 K there is a large dark current with one peak at about 250 K. The dark current for the undoped pellet had an activation energy of 0.43 ± 0.02 eV while for all the doped pellets the dark current had an activation energy in the range $0.30 < E < 0.38$ eV. There appeared to be no correlation between the relative magnitudes of the peak and the doping concentration. Unfortunately, it was not possible to obtain an activation energy from the TSC peak.

12.6 SUMMARY

Powder samples have been studied by the methods of photoluminescence and thermoluminescence. Sintered pellets were studied by these methods and also by thermally stimulated conductivity. The TSC measurements were disappointing but the other techniques could be applied successfully to rutile powders.

The results of the photoluminescence measurements showed that increasing chromium doping caused an increase in photoluminescence intensity and that increasing iron doping had the opposite effect. All the chromium doped powders showed the same form of temperature dependence as seen in undoped and chromium doped single crystals, while the iron doped powders showed a transition to the form found for iron

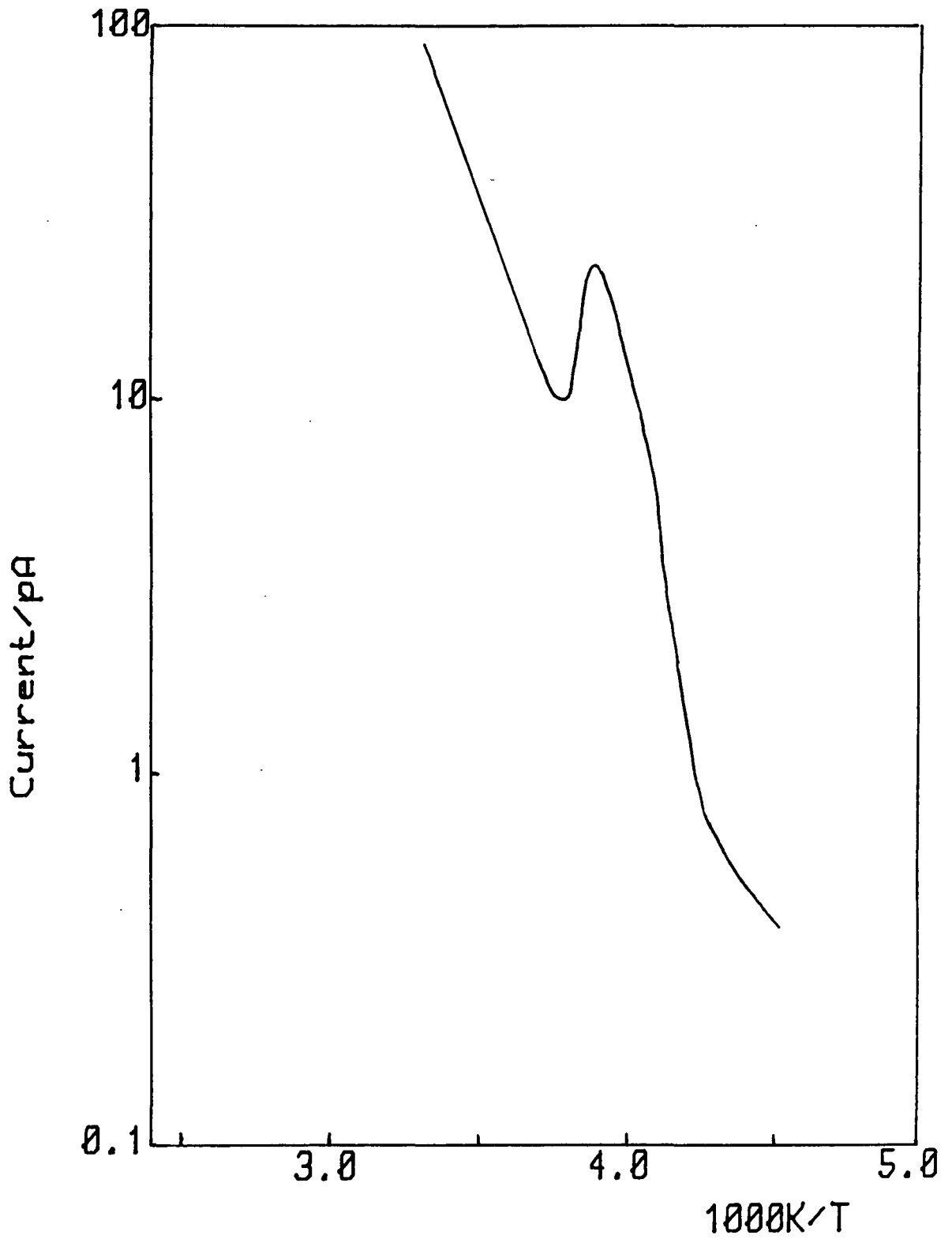


Figure 12.5.1 TSC spectrum from undoped pellet

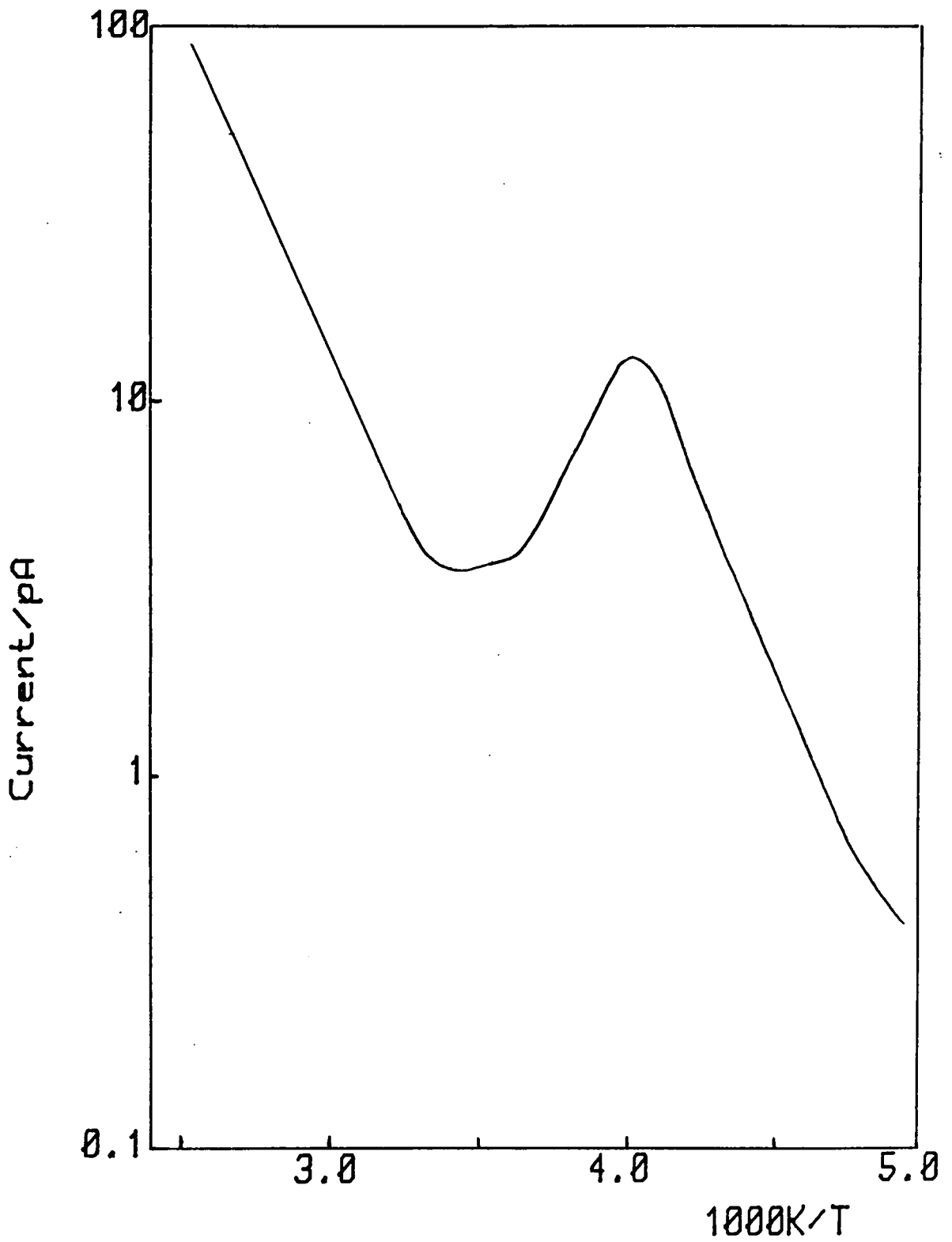


Figure 12.5.2 TSC spectrum from 313ppm Cr pellet

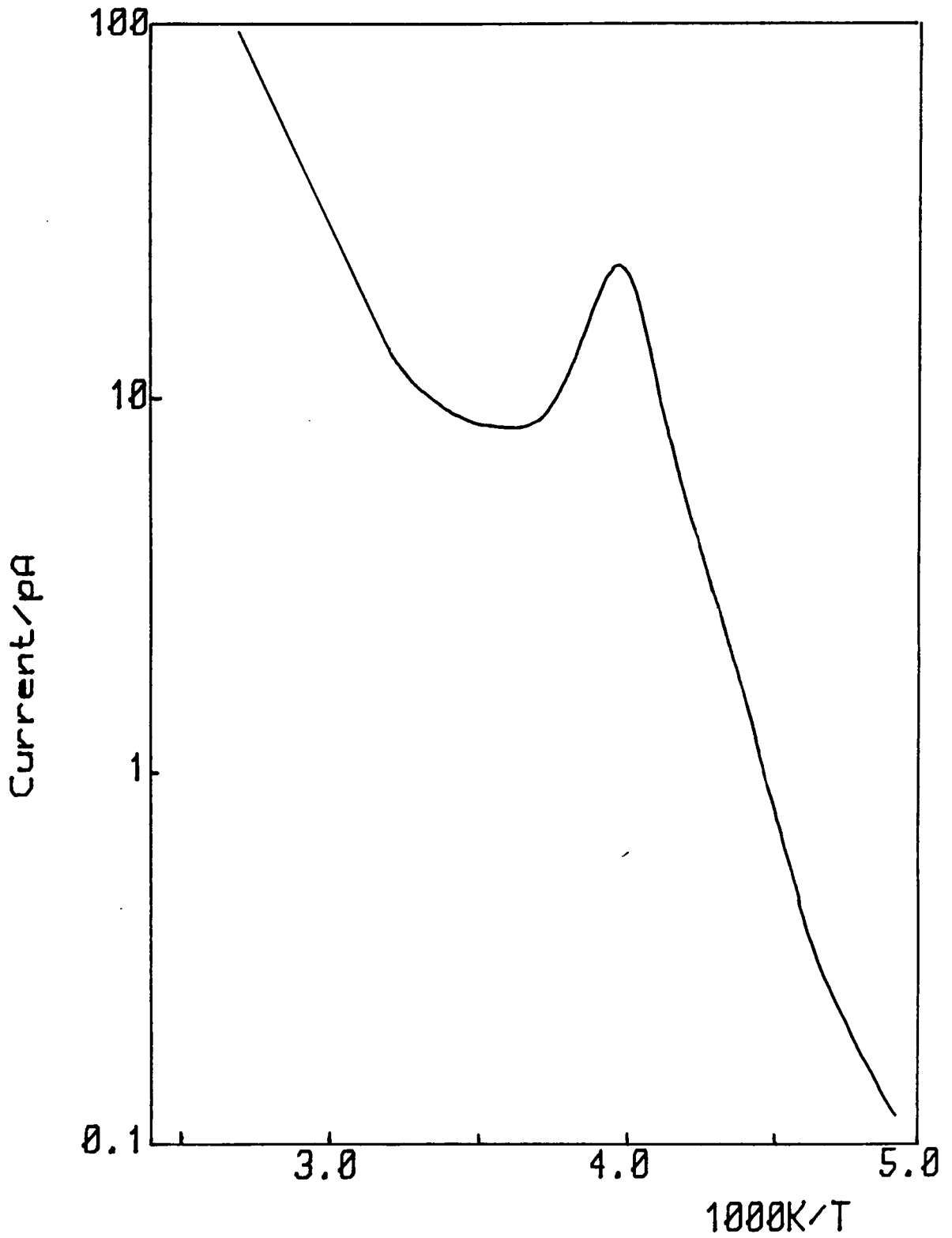


Figure 12.5.3 TSC spectrum from 225ppm Cr pellet

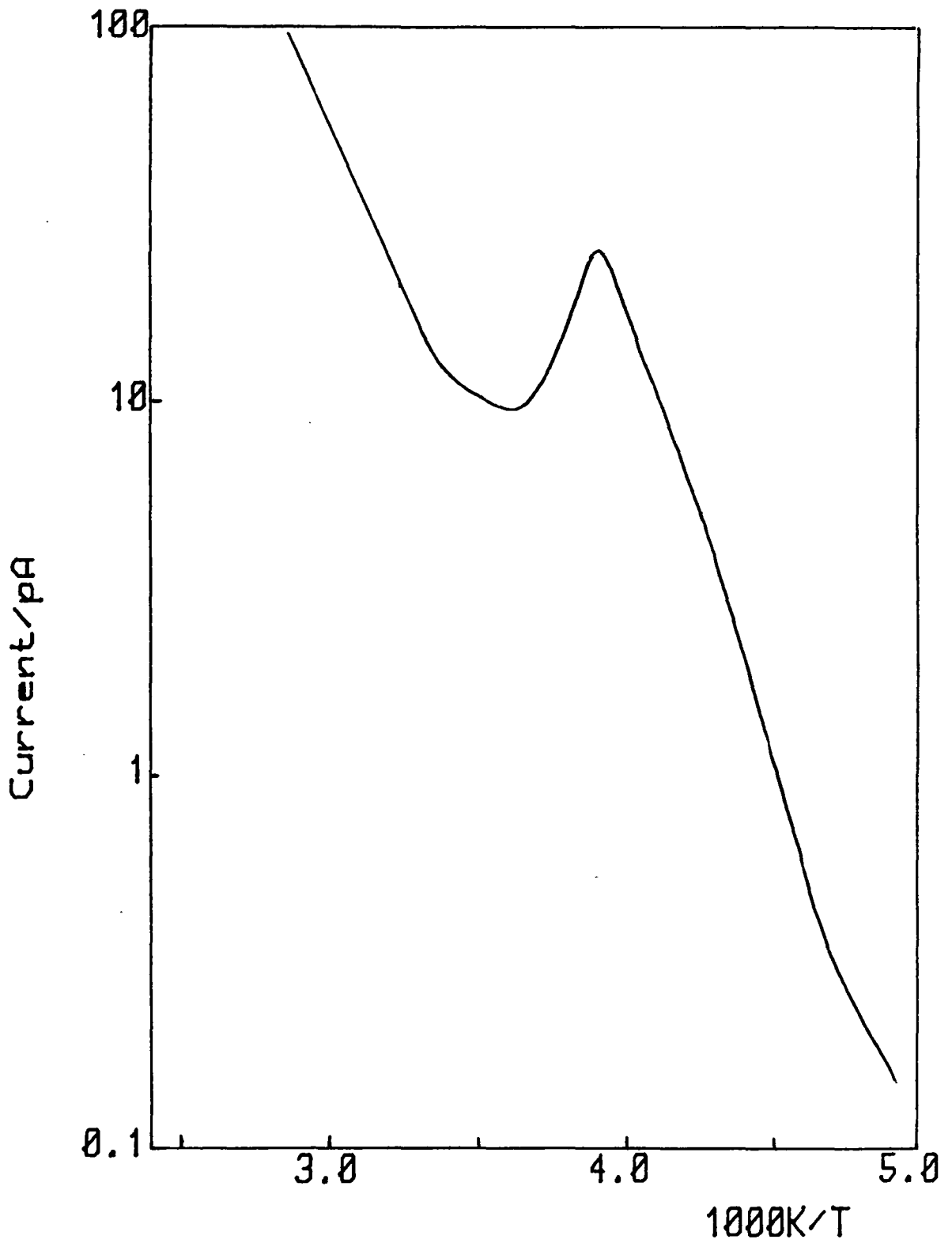


Figure 12.5.4 TSC spectrum from 95ppm Cr pellet

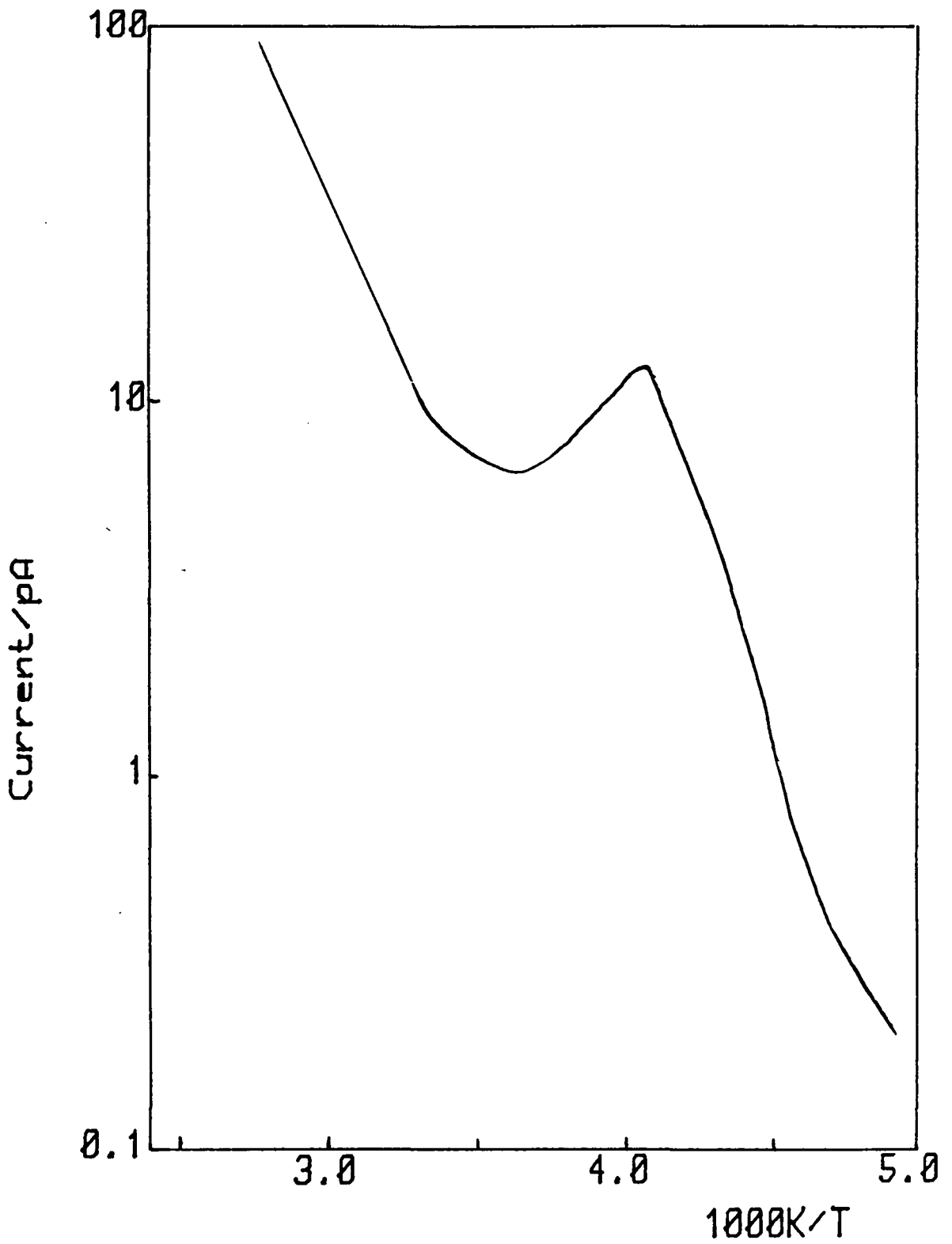


Figure 12.5.5 TSC spectrum from 48 ppm Cr pellet

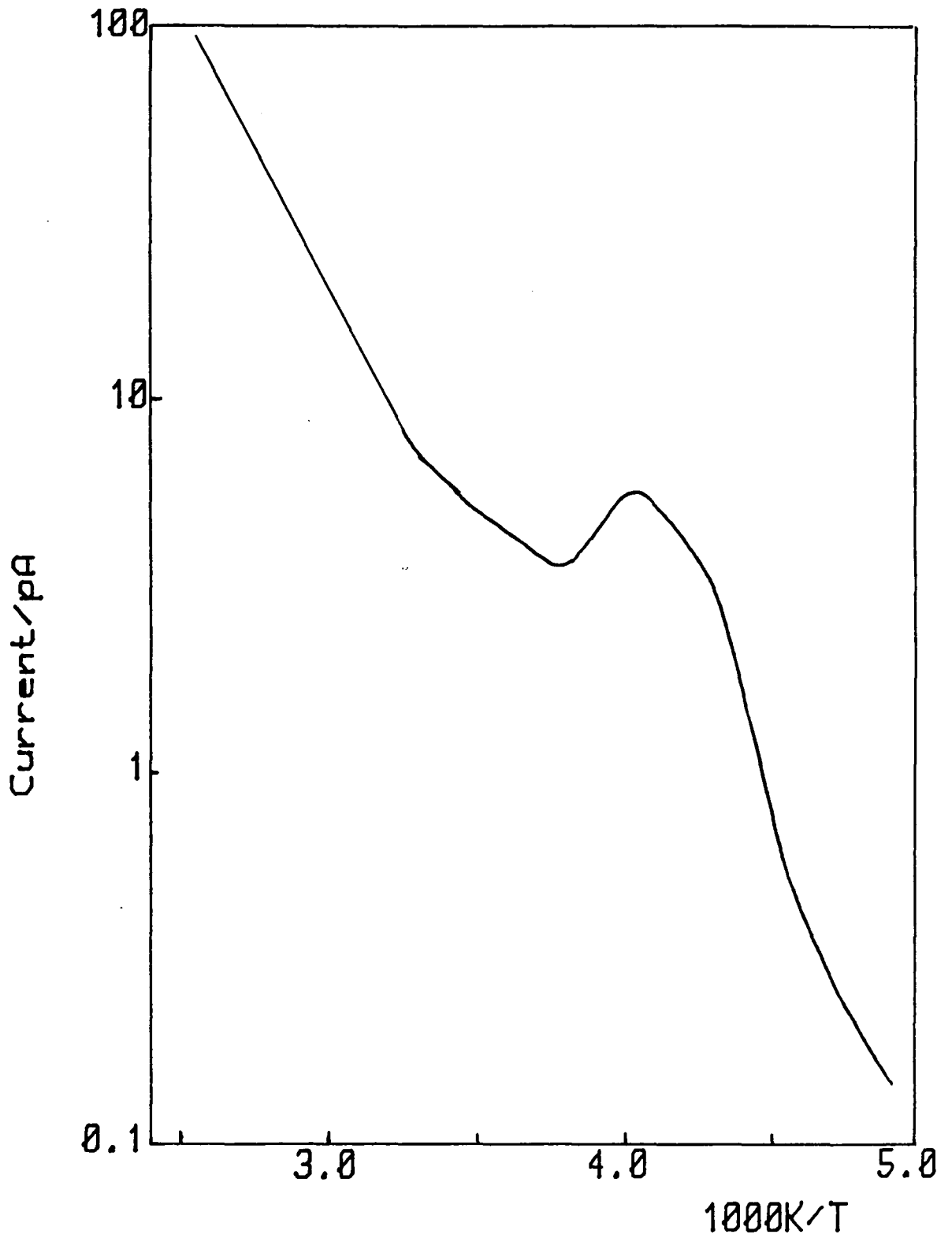


Figure 12.5.6 TSC spectrum from 405ppm Fe pellet

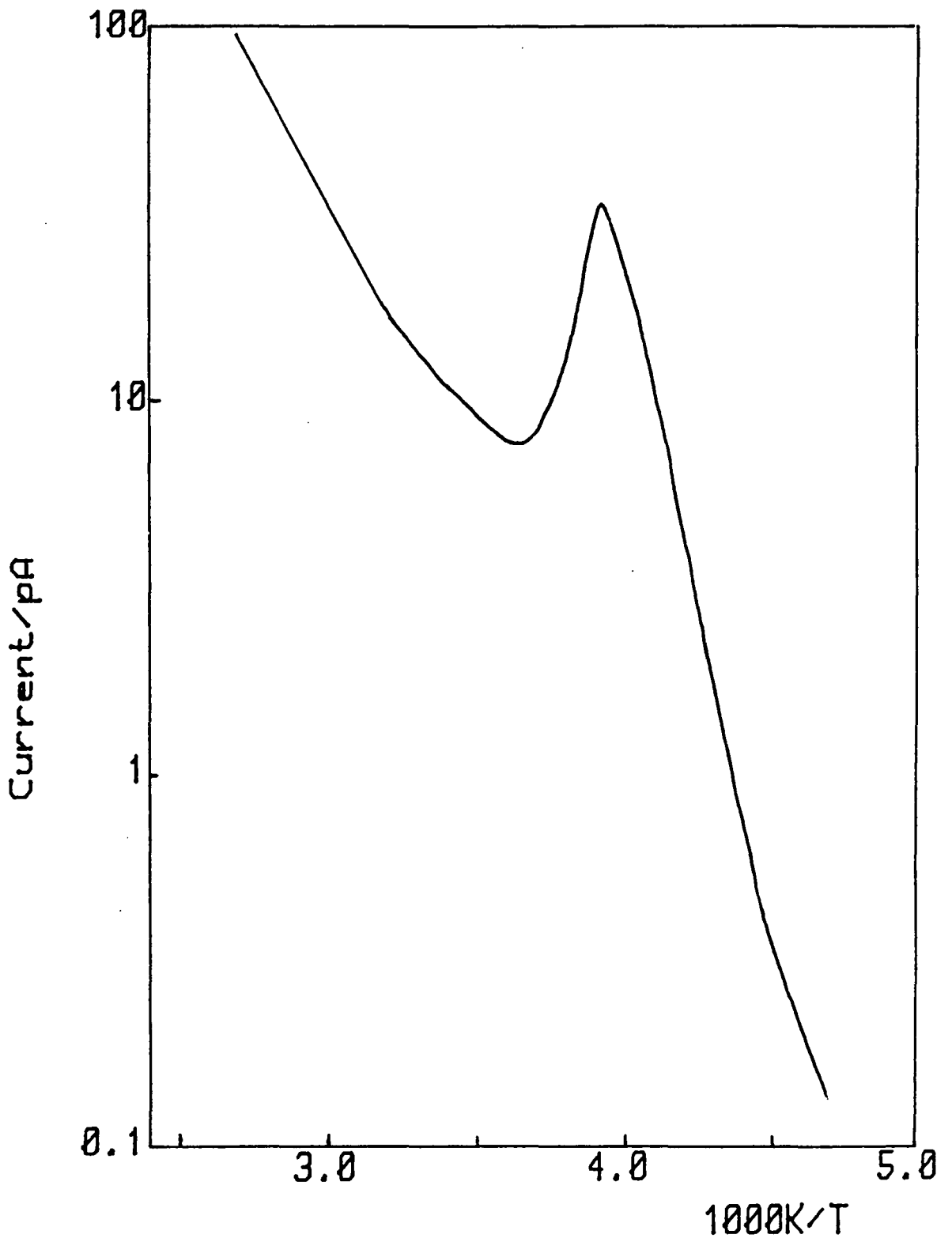


Figure 12.5.7 TSC spectrum from 135ppm Fe pellet

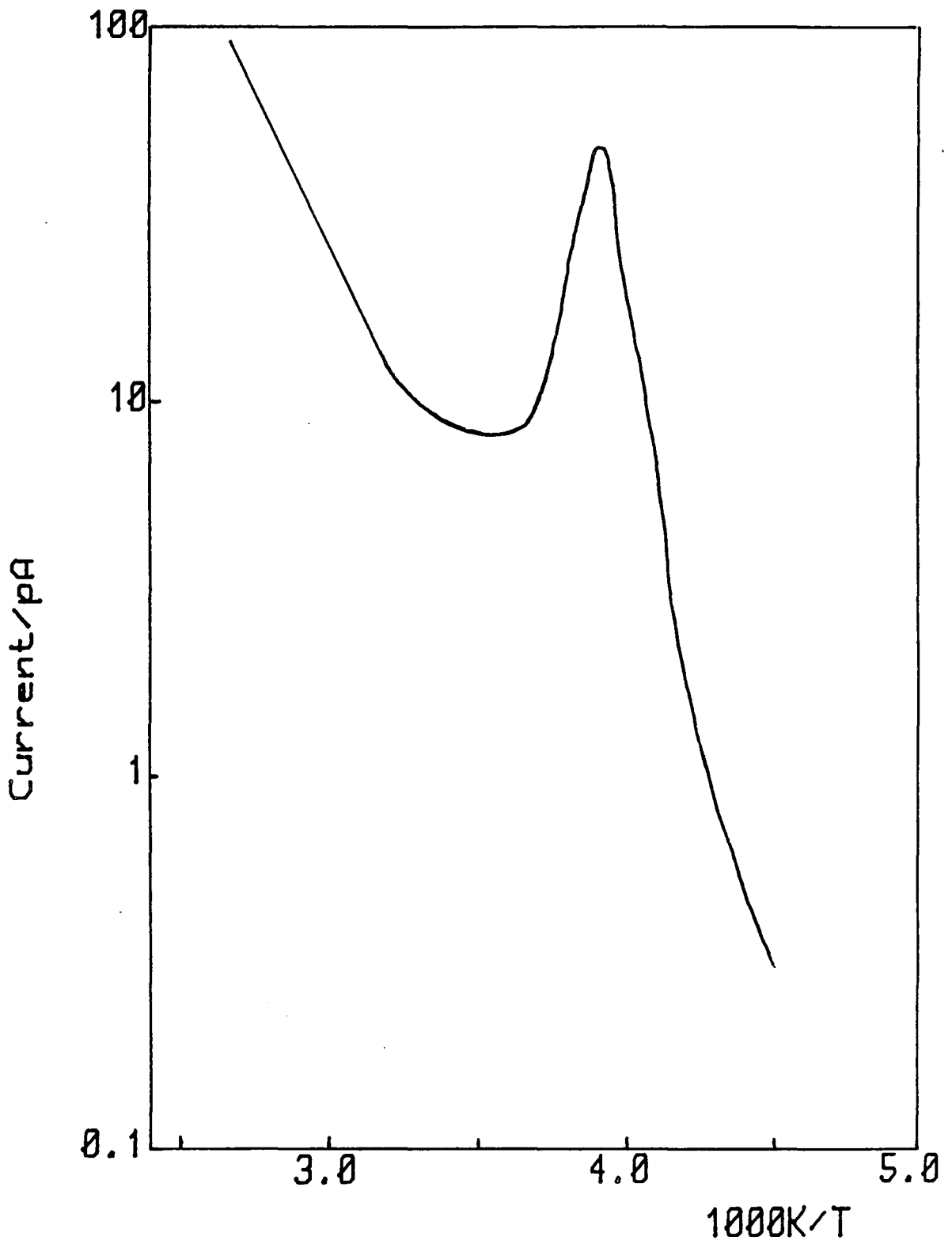


Figure 12.5.8 TSC spectrum from 70 ppm Fe pellet

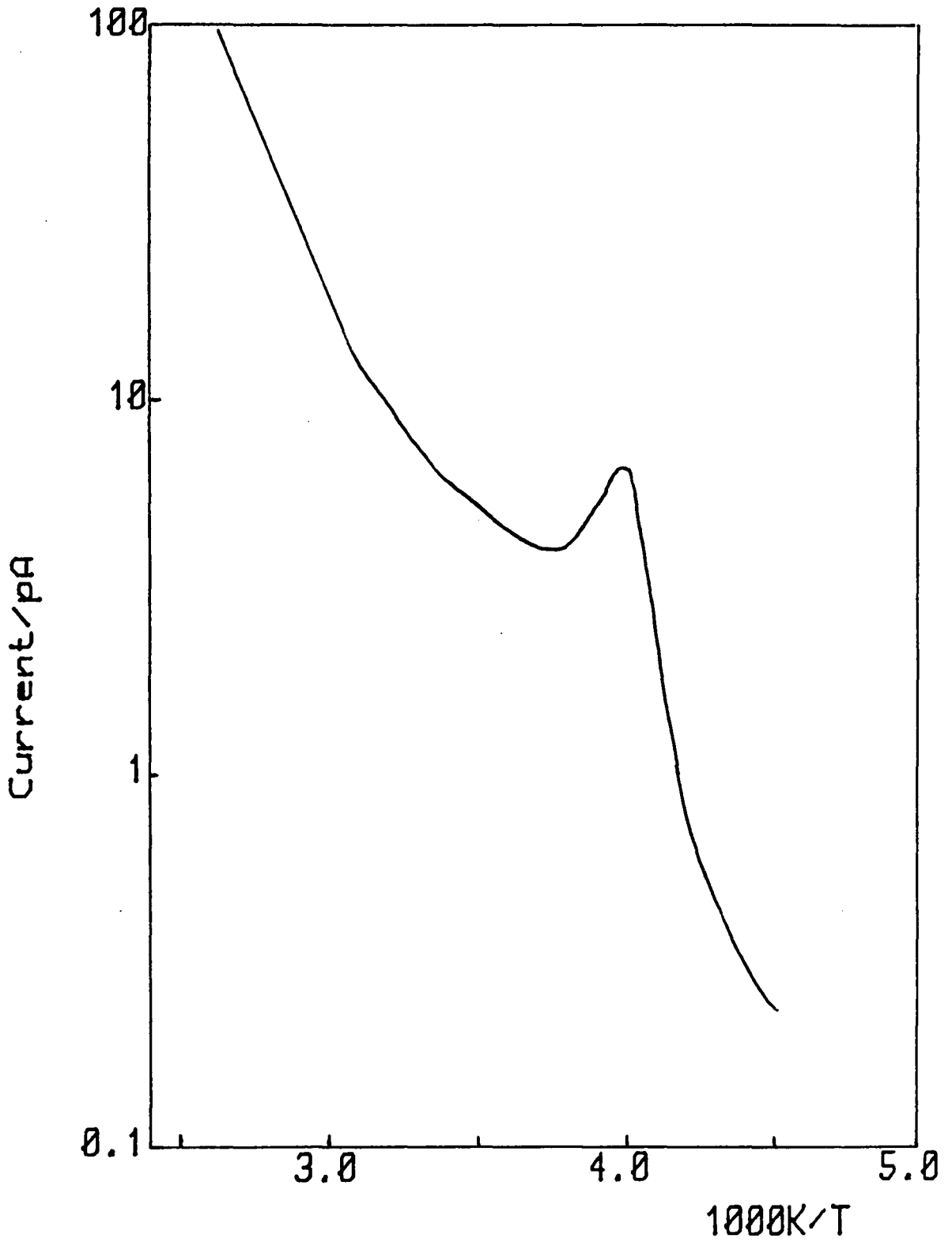


Figure 12.5.9 TSC spectrum from 35 ppm Fe pellet

doped single crystals. This supports the idea that the iron introduces an additional recombination path that reduces the luminescence efficiency.

Thermoluminescence measurements indicated that the spectra were composed of the same peaks found in the crystal samples. Thermal cleaning enabled one peak to be isolated. This agreed closely with the dominant peak found in all the single crystals.

CHAPTER 13

CONCLUSIONS

13.1 Summary

13.2 Conclusions

13.1 SUMMARY

Undoped samples of single crystal rutile and rutile powder have been studied by the methods of photoluminescence, thermoluminescence and thermally stimulated conductivity. Crystal samples doped with chromium, iron, manganese, cobalt and nickel and powder samples doped with chromium and iron were also studied. Additionally capacitance-voltage, current-voltage and deep level transient spectroscopy measurements were made on Schottky diodes fabricated on rutile made semiconducting by reduction and niobium doping.

All the samples showed photoluminescence in a broad band centred on about 850 nm, although the intensity of the luminescence varied with the doping of the sample. Table 13.1.1 gives a summary of the photoluminescence intensity relative to an undoped sample. It was found that chromium doping increased the luminescence intensity, nickel doping made little difference and iron, manganese, or cobalt doping reduced the intensity significantly.

These differences were borne out in measurements of the temperature dependence of the photoluminescence. Undoped, chromium and nickel doped samples all showed one form of PL temperature dependence in which the luminescence was quenched above 190 K. Iron, cobalt and manganese doped samples showed a different dependence in which the intensity decreased from 80 K. This was attributed to a fast non-radiative recombination path being introduced by these dopants.

Powder samples confirmed these differences. Chromium doped powders showed the same form of photoluminescence temperature dependence as seen in undoped and chromium doped samples, while iron doped powders showed a transition to the form found for iron doped crystals as the doping level was increased. The chromium doped powders showed an increase in photoluminescence intensity with chromium doping which supports the view of several workers that chromium provides the luminescence centre in rutile.

Evidence was found in thermoluminescence spectra for nine different trapping

Relative photoluminescence intensity for
the various dopants

	Relative PL intensity
undoped	1
Cr	10
Fe	0.1
Mn	0.1
Co	0.1
Ni	1

Table 13.1.1

levels. A summary of the activation energies and capture cross-sections obtained is given in table 13.1.2. Entries under each dopant show which peaks were found for each dopant and the magnitude of the peak. It can be seen that those dopants that caused a reduction in photoluminescence intensity also had low intensity TSL peaks. Activation energies obtained from the TSL spectra agreed closely with those reported by Hillhouse [10] and Hillhouse and Woods [142,149] apart from one peak in a chromium doped sample.

Capture cross-sections determined by analysis of the peaks were generally larger than determined by other workers. This may be due to the steady reduction over the years in estimates for the value of the effective mass in rutile. Since the capture cross-section is determined from a value of $N_c \langle v \rangle \sigma_n$ and $N_c \langle v \rangle \propto m^*$, a smaller value of m^* would imply a larger value of σ for a given value of $N_c \langle v \rangle \sigma_n$.

Thermoluminescence measurements on powders indicated that the spectra were composed of the same peaks found in the crystal samples, although they were not distinct.

Thermally stimulated conductivity measurements were, generally, marred by large dark currents, although some spectra were obtained. Hillhouse [10] has shown that furnacing and then quenching crystal samples can lead to an increase in dark conductivity. It is possible that the samples studied here were in a similar state to that achieved by quenching, although the samples had been annealed in oxygen for long periods in an attempt to avoid this problem.

Some TSC peaks were found in excess of the dark current at temperatures between 300 and 400 K. A technique of subtracting the dark current from the total TSC was adopted to isolate the excess TSC. This technique could produce distinct peaks but is only valid if the total TSC can be considered as the sum of two parts. Several investigators [104,161-163] have suggested that the TSC method is not suitable for use in materials in which the dark current is of the same order or larger than the TSC excess current. For some of the TSC peaks isolated by this subtraction

Summary of trapping parameters and relative TSL peak intensities

Temp	E_T /eV	σ/cm^2	undoped	Cr	Fe	Mn	Co	Ni
89	0.18							0.75
100	0.14	10^{-20}	10			4	1	1.0
115	0.22	10^{-18}	27	64		2	1	1.5
165	0.37	10^{-17}	55	115	8	2	2.5	30
200	0.40	3×10^{-19}		45				
200	0.55	10^{-14}			4.5		1.5	
220	0.58	5×10^{-16}		15	3.5			
245	0.68	10^{-18}	7					
284	?	?	0.5(NL)					

Table 13.1.2

technique this question of TSC suitability must be taken seriously. The method of thermally stimulated depolarisation currents (TSDC) may be a way of overcoming this limitation. Driver and Wright [175] and Kirov and Zhelev [176] were among the first to use the TSDC method to study trapping centres in CdS crystals. With this method, the traps are first filled at some high temperature by the application of an electric field across the solid specimen, which is provided with one ohmic and one blocking contact, and the specimen is then cooled down with the field applied so that the carriers injected into the specimen through the ohmic contact are trapped. Upon heating and applying a field of reverse sign (or by short-circuiting the electrodes on heating) the trapped carriers are released giving rise to the thermally stimulated depolarisation current. This method is similar to the TSC method; the only difference is the method of filling the traps, so that techniques similar to those used for TSC can be used to analyse TSDC curves.

It is interesting to note that the samples with high luminescence efficiency and thermal quenching of the luminescence showed little, if any, increase in TSL corresponding to the onset of appreciable dark current, while the samples with reduced luminescence efficiency did show an increase in TSL. This could indicate a reduction in the cross-section for the fast recombination path with increasing temperature.

The properties of semiconducting reduced and niobium doped rutile were investigated by studying gold Schottky diodes. Poor diode characteristics were found but the diodes did show rectifying properties and bias dependent depletion layers. Forward biased current-voltage characteristics were typical of space charge limited conduction. These have been reported by other workers [157] and could imply a very high mobility, possibly with conduction in a separate band.

DLTS measurements were successful on the niobium doped crystal. The spectra showed one dominant maximum. The variation of this peak with the rate window gave an activation energy of 0.38 eV and a capture cross-section of $7 \times 10^{-18} \text{ cm}^2$. This is in excellent agreement with the values of 0.37 eV and

10^{-17} cm^2 for the dominant TSL peak and suggests that the simple insulator model used for TSL analysis applies well to rutile. The DLTS result allows the results for trap depths derived from TSL measurements to be viewed with some confidence.

13.2 CONCLUSIONS

It has been shown by the correlation between DLTS and TSL measurements that the simple insulator model applies well to rutile. Photoluminescence and thermoluminescence measurements have shown that these techniques can be applied successfully to powders. Trapping parameters can be deduced from these measurements but the lack of distinct peaks in thermoluminescence spectra from powder samples makes a study of crystal samples useful. Having established trapping parameters from single crystal samples, the powder results can be interpreted more easily.

While pigment manufacturers are, for commercial reasons, cautious about revealing the effects of dopants on their pigments, it is interesting to note two features which might have an influence on, for example, paint durability. The first of these is the reduction in luminescence efficiency attributed to a fast recombination path in iron, cobalt and manganese doped samples. Clearly, a pathway of this nature would allow any photo-excited carriers to recombine quickly and reduce photo-degradation. The second feature is the large excess TSC peak at 380 K seen in undoped and, particularly, chromium doped rutile. While most of the other traps reported earlier would be quickly emptied at room temperature and would have little influence on carrier concentration, a trap emptying at 380 K might have sufficient influence to alter the carrier concentration and hence photo-degradation. A TSDC study of traps in this temperature range could prove worthwhile.

- 1 J.Kiwi, E.Bergaiello, E.Pelizzetti, M.Visca, M.Gratzel; 'Photogeneration of
Hydrogen', (eds, A.Harriman, M.West), Academic, New York, 1982, p119
- 2 S.Forberg, B.Bergman; Proc. 8th. Int. Symp. on the Basis for Nuclear Waste
Management, Boston, 1984, p421
- 3 R.Darby, J.Leighton; 'The Modern Inorganic Chemicals Industry', The Chemical
Soc., London, 1977
- 4 'Unitani Titanium Dioxide Pigments', American Cyanamid Co., USA, 1956
- 5 'Tioxide Pigments, A Guide to Selection', Tioxide International, Stockton, 1977
- 6 G.Neville; Encyclopaedia of Chemical Technology, 20, (1969), 380
- 7 B.Ranby, J.Rabek; 'Photodegradation, Photo-oxidation and Photostabilisation of
Polymers', Interscience, New York, 1975
- 8 G.Kaempf, W.Papenroth, R.Holm; J. Paint Technol., 46, (1974), 56
- 9 S.Torluachi, U.Baructi, G.Zorzella; Cent. Ric. Pigmenti Montecatini Edison, 24,
(1974), 10
- 10 R.Hillhouse; PhD Thesis, Durham University, 1981
- 11 Bursill, Hyde, Terasaki, Watanabe; Phil. Mag. 20, (1969), 347
- 12 O.Johnson; Phys Rev, 136A, (1964), 284
- 13 H.Huntingdon, G.Sullivan, Phys. Rev. Lett., 14 (1965), 177
- 14 F.Kroger, H.Vink; 'Solid State Physics, Chemistry of Imperfect Crystals', Wiley,
1964
- 15 A.Fujishima, K.Honda; Bull. Chem. Soc. Japan, 44, (1971), 1148
- 16 J.Marucco, J.Gautron, P.Lemasson, J.Loup; C. R. Acad. Sci. Paris, 289C,
(1979), 117
- 17 P.Kofstad; J. Phys. Chem. Solids, 23, (1962), 1579
- 18 K.Forland; Acta. Chem. Scand., 18, (1964) 1267
- 19 C.Pickard, P.Gerdanian; J. Solid State Chem., 14 (1975), 66

- 20 R.Dirstine, C.Rosa; Z. Metallkunde, 70, (1979), 322
- 21 C.Alcock, S.Zador, B.Steele; 'Electromotive Force Measurements in High Temperature Systems', Institute of Mining and Metallurgy, London, 1968
- 22 J.Marucco, J.Gautron, P.Lemasson; J. Phys. Chem. Solids, 42, (1981), 363
- 23 D.Cronemeyer; Phys. Rev., 87, (1952), 876
- 24 P.Moch, M.Balkanski, P.Aigfain; C. R. Acad. Sci., 251, (1960), 1373
- 25 B.Soffer; J. Chem. Phys., 35, (1961), 940
- 26 A.Stepanov, V.Agekyan; Sov. Phys. Solid State, 17, (1975), 3676
- 27 F.Arntz, Y.Yacobi; Phys. Rev. Lett., 17, (1966), 857
- 28 K.Vos, H.Krusemeyer; Solid State Comm., 15, (1974), 949
- 29 H.Frederikse; J. Appl. Phys. Suppl., 32, (1961), 2211
- 30 A.VonHippel, J.Kalnoys, W.Westphal; J. Phys. Chem. Sol., 23, (1962), 779
- 31 J.Becker, W.Hosler; Phys. Rev., 137, (1965), 1872
- 32 G.Acket, J.Volger; Physica, 32, (1966), 1680
- 33 J.Pak; Sov. Phys. Solid State, 16, (1975), 2023
- 34 V.Agekyan, Y.Stepanov; Sov. Phys. Solid State, 17, (1975), 2390
- 35 D.Fisher; Phys. Rev., B5, (1972), 4219
- 36 D.Adler; 'Solid State Physics', (ed. F.Seitz), Academic Press, New York, 1968
- 37 A.Kahn, A.Leyendecker; Phys. Rev., 135, (1964), 1321
- 38 K.Vos; J. Phys. C, 10, (1977), 3917
- 39 N.Bogoroditskii, V.Kristya, Y.Panova; Sov. Phys. Solid State, 9, (1967), 187
- 40 V.Bogomolov, V.Zhuze; Sov. Phys. Solid State, 8, (1967), 1904
- 41 V.Bogomolov, I.Smirnov, E.Shadrichev; Sov. Phys. Solid State, 11, (1970), 2606
- 42 R.Blumenthal, J.Kirk, W.Hirthe; Phys. Chem. Solids, 28, (1967), 1077
- 43 E.Greener, F. Barone, W.Hirthe; J Amer. Ceram. Soc 48, (1965) 623
- 44 J.Baumard, E. Tani; Phys Stat. Sol. (a) 39 (1977) 373

- 45 E. Tani. & J.F. Baumard; *J Sol. St. Chem* 32 (1980) 105-13
Electrical Properties and Defect Structure of Rutile Slightly Doped with Cr and Ta
- 46 B.Poumellec, J.Marucco, F.Lagnel; *Phys. Stat. Sol.(a)* 89 (1985) 375
- 47 I.Austin and N Mott; *Advance in Physics* 18 (1969)
- 48 V.Bogomolov E.Kudinov and Y.Firsor; *Sov. Phys. Solid. State* 9 (1968) 2502
- 49 R.A.Brekenridge W.Hosler; *Phys per* 91 (1953) 793
- 50 R.Hasiguti, E.Yagi, M.Aono; *Radiat. Eff.* 4 (1970) 137
- 51 J.Baumard, F.Gervais; *Phys. Rev.*, B15 (1977) 2316
- 52 J.Pascual, J.Camassel, H.Mathieu; *Phys. Rev., Lett* 39 (1977) 1490
- 53 V.Cristea, V.Babes; *Phys. Stat. Sol. (a)* 45 (1978) 617
- 54 J.Deford, O.Johnson; *J. Appl. Phys.* 54 (1983) 889
- 55 P.Kelly, P.Braunlich; *Phys. Rev.*, 31 (1970) 1587-96. 'Phenomenological Theory of Luminescence'
- 56 K.H.Nicholas, J.Woods; *Brit. J. Appl. Phys* 1964 15 783. 'The evaluation of electron trapping parameters from conductivity glow curves in CdS.'
- 57 H.Dittfeld and J.Voigt; *Phys. Stat. Sol.* 3 (1963) 1941
- 58 K.Unger; *Phys. Stat Sol* 2 (1962) 1279
- 59 P.Kivits, J.Reulen, J.Hendricx. F.Van Empel and J.Van Kleef. *J.Luminescence* 16 (1978) No. 2145-160
- 60 F.Schmidlin, G.Roberts; *Phys. Rev., lett* 20 (1968) 1173
- 61 A.Rose; 'Concepts of Photoconductivity and Allied Problems', Interscience (1963)
- 62 M.Lampert, P.Mark; 'Current Injection in Solids', Academic Press, New York, 1970
- 63 M.Lampert; *Rep, Prog. Phys* 27 (1964) 329
- 64 J.Randall, and M.Williams; *Proc. Roy. Soc A* 184 (1945) 390

- 65 F.Daniels, C.Boyd, D.Saunders; Science 117 (1953) 343
- 66 R.Bube; Phys. Rev., 83 (1951) 393
- 67 R.Bube; Phys. Rev., 99 (1955) 1105
- 68 R.Bube; Phys. Rev., 101 (1956) 1668
- 69 R.Bube; Phys. Rev., 106 (1957) 703
- 70 R.Bube; J.Chem. Phys, 23 (1955) 18
- 71 C.Delbecq, P.Pringsbeim, P.Yuster; Z.Phys. 138 (1954) 266
- 72 I.Broser, R. Broser-Warminsky; Brit. J.Appl, Phys. Suppl. 4 (1955) 90
- 73 G.Garlick and A.Gibson. Proc. Roy. Soc. 60 (1948) 574
- 74 R.Chen; J.Mat.Sci 11 (1976) 1521-41. 'Review: Methods for Kinetic analysis of thermally stimulated processes'
- 75 P.Kwits and H.Hagebeuk; J. Lunim 15 (1977); 'Evaluation of the model for thermally stimulated Luminescence and conductivity: reliability of trap depth determinations'
- 76 I.Saunders; J.Phys C 2 (1969) 2181-98; 'The thermally stimulated luminescence and conductivity of insulators'
- 77 P.Braunlich, P.Kelly; Phys. Rev., B1 (1970) 1596-603; Correlations Between Thermoluminescence and Thermally Stimulated Conductivity.
- 78 G Dussel and R.Bube. Phys. Rev., 155 (1967) 764-79; 'Theory of Thermally stimulated Conductivity in a previously photoexcited Crystal'
- 79 P.Kelly and M.Laubitz, P.Braunlich; Phys. Rev., B4 (1971) 1960
- 80 H.J.L.Hagebeuk and P.Kivits; Physica 83B (1976) 289-294; 'Determination of trapping parameters from the conventional model for thermally stimulated luminescence and conductivity'
- 81 D.Curie; 'Luminescence in Crystals' Methuen London (1963)
- 82 N.Mott R.Gurney; 'Electronic Processes in Ionic Crystals', Clarendon Press, Oxford (1940)
- 83 F.Seitz; Trans Faraday Soc. 35 (1939) 79

- 84 H.Klasens; J. Phys. Chem. Solids. 7 (1958) 175
- 85 M.Schön; Tech. Wiss. Abh. Osram-Ges 6 (1953) 49
- 86 C.Henry, D.Lang, Phys. Rev., B15 (1977) 989
- 87 R.Pässler; Czech. J.Phys. B24 (1974) 322
- 88 R.Pässler; Czech. J.Phys. B25 (1974) 219
- 89 R.Pässler; Phys. Stat Sol. (6) 78 (1976) 625
- 90 R.Pässler; Phys. Stat. Sol. (6) 85 (1978) 203
- 91 P.T.Landsberg; Phys. Stat Sol 41 (1970) 457-89; 'Review Article: Non-Radiative Transitions in Semiconductors'
- 92 P.T.Landsberg; J. Lumin 7 (1973) 3
- 93 E.F.Smith P.T.Landsberg. J.Phys. Chem. Solids 27 (1966) 1727-38; 'Phonon Cascade Theory'
- 94 A.Milnes; 'Deep Impurities in Semiconductors', Wiley, New York, 1973
- 95 M.Lax; Phys. Rev., 119 (1960) 1502
- 96 K.I.Ralph, F.D.Hughes; Sol. St. Communications 9 (1971) 1477-80 'Capture Cross Section of Trapping Centres in Polar Semiconductors'
- 97 V.L.Bonch-Bruevich, E.G.Landsberg; Phys. Stat. Sol. 29 (1968) 9-43
- 98 D.Howgate; Phys. Rev., 177 (1969) 1358
- 99 F.Urbach; Sitzbes Akad Wiss Wein Math. Natavio Klasse 139 (1930) 353
- 100 R.Chen: J.Appl, Phys. 40 (1969) 570-85; 'On the Calculation of Activation Energies and Frequency Factors from Glow Curves'
- 101 R. Chen; J. Appl. Phys. 42, (1971), 5899
- 102 J. Simmons, G. Taylor, M. Tam; Phys. Rev. B7, (1973), 3714
- 103 J. Helfrich, N. Riehl, P. Thoma; Phys. Lett. 10, (1964), 31
- 104 P. Devaux, M. Schott; Phys. Stat. Sol, 20 (1967), 301
- 105 C. Westgate, G. Warfield; J. Chem. Phys. 46 (1967) 537
- 106 I. Saunders, R. Jewitt; 'Thin film circuit element', Annual Report on Research Project R7-27, Document AD 480752, National Technical Information Service, Springfield, Virginia, USA., 1965

- 107 A. Booth; *Canad. J. Chem.* 32 (1954), 214
- 108 A. Bohun; *Czech J. Phys.* 4, (1954), 91
- 109 W. Hoogenstraaten; *Phil. Res. Repts.* 13, (1958), 515
- 110 P. Keating; 'Thermally Stimulated Emission and Conductivity Peaks in the Case of Temperature Dependent Trapping Cross Sections', *Proc. Phys. Soc.*, 78, (1961), 1408-15
- 111 K. Boer, S. Oberlander, J. Voigt; *Ann. Lpz.* 2, (1958), 130
- 112 H. Sacks; PhD thesis, Carnegie-Mellon University, Pittsburgh, Pennsylvania, 1970
- 113 C. Gear; *Comm. ACM*, 14, (1971), 176
- 114 P. Braunlich, P. Kelly, J. P. Fillard; 'Thermally Stimulated Luminescence and Conductivity in Thermal Relaxation of Solids', ed. P. Braunlich, Springer Verlag, Berlin, 1978, Chap. 2, pp 35-91
- 115 I. Parfianovitch; *J. Exp. Theor. Phys. SSSR*, 26, (1954), 696
- 116 R. Chen, S. Winer; *J. Appl. Phys.*, 41, (1970), 5227
- 117 R. Haering, E. Adams; *Phys. Rev.*, 117, (1960), 451
- 118 M. Selion; *Tech. Wiss.* 7, (1958), 175
- 119 I. Boiko, E. Rashba, A. Trofinenko; *Sov. Phys. Solid State*, 2, (1960), 99
- 120 Luschik; *Dok. Akad. Nauk. SSSR*, 101, (1955), 641
- 121 A. Halperin, A. Braner; *Phys. Rev.*, (117) (1960), 408
- 122 R. Chen; *J. Appl. Phys.*, 40, (1969), 570
- 123 R. Chen; *Chem. Phys.* 6, (1970), 125
- 124 R. Chen; *Chem. Phys.* 11, (1971), 371
- 125 L. Grossweiner; *J. Appl. Phys.* 24, (1953), 1306
- 126 J. Franks, P. Keating; 'The Measurements of Defect States in CdS', *J. Phys. Chem. Sol.*, 22, (1961), 25
- 127 V. Sandoninskii, A. Zhdan; *Sol. St. Electr.*, 13 (1970), 69
- 128 J. Voigt; *Dipolmarbeit* (1968)

- 129 P. Kivits; 'Interpretation of thermoluminescence and thermally stimulated conductivity experiments. Part 1: Extensions of the conventional model', *J. Lumin*, 16, (1958), 119-44
- 130 E. H. Rhoderick; 'Metal-semiconductor contacts', *I.E.E. Proc.*, 129, (1982), 1-13
- 131 W. Schottky; *Naturwiss.* 26, (1938), 843
- 132 E. Rhoderick; 'Metal-Semiconductor Contacts', Clarendon, Oxford, 1977
- 133 J. Hildebrand, R. Gold; *RCA Rev.*, 21, (1960), 245
- 134 P. Baxandall, D. Colliver, A. Fray; *J. Sci. Instrum.* 4, (1971), 213
- 135 J. Copeland; *IEEE Trans.*, ED16, (1969), 445
- 136 G. Miller; *IEEE Trans.*, ED19, (1972), 1103
- 137 D. Lang; 'Fast capacitance transient apparatus: Application to ZnO and O centres in GaP pn junctions', *J. Appl. Phys.*, 45, (1974), 3014-22
- 138 D. V. Lang; 'Deep-level transient spectroscopy: A new method to characterise traps in semiconductors', *J. Appl. Phys.*, 45, (1974), 3023-32
- 139 C. Wagner; *Phys. Z.*, 32, (1931), 641
- 140 D. Verity, D. Shaw, F. Bryant, C. Scott; *Phys. Stat. Sol. (a)*, 78, (1983), 267
- 141 D. Lang; 'Thermally Stimulated Relaxations in Solids', ed. P. Braunlich, Springer Verlag, Berlin, 1979
- 142 R. Hillhouse, J. Woods; 'Growth of rutile crystals and photoelectronic props', *Phys. Stat. Sol (a)*, 46 (1978), 163
- 143 N. Szydlo, R. Poirier; 'I-V and C-V characteristics of Au/TiO₂ Schottky diodes', *J. Appl. Phys.* 51, (1980), 3310-2
- 144 Bowen; 'Chemical Aspects of light', Oxford, 1946
- 145 M. Verneuil; *C R Acad. Sci.* 135 (1902), 791

- 146 A.K.J. Ghosh, F. G. Wakim, R. R. Addis; 'Photoelectronic Processes in Rutile',
Phys. Rev. 134, (1969), No. 3, 979-988
- 147 L. Grabner, S. Stokowski, W. Brower; 'No-Phonon ${}^4T_{2g} - {}^4A_{2g}$
Transitions of Cr^{3+} in TiO_2 ', Phys. Rev. B2, (1970), 590-7
- 148 A. K. Ghosh, R. B. Lauer, R. R. Addiss; 'Photoconductivity and photoluminescence
kinetics associated with the luminescence centre in
rutile (TiO_2)', Phys. Rev. B8 (1973) 4842
- 149 R. Hillhouse, J. Woods; Phys. Stat. Sol. (a), 67, (1981), 119
- 150 D. Fields, P. Moran; Phys. Rev. B9, (1974), 1836
- 151 R. Lauer, R. Addiss, A. Ghosh; 'Properties of the Room-Temp Electron Trap in
Rutile', J. Appl. Phys., 42, (1971), 3508-12
- 152 F. A. Grant; Rev. Mod. Phys., 31 (1959), 646
- 153 R. Hasiguti; Metal Physics 9, (1963), 95
- 154 E. Iguchi, K. Yajima; 'Diffusion of Oxygen Vacancies in Reduced Rutile
(TiO_2)', J. Phys. Soc. Jap., 32, (1972), 1415
- 155 L. Partain; J. Appl. Phys. 54, (1983), 5218
- 156 M. Abhowitz, M. Scharfe; Solid State Commun., 23, (1977), 305
- 157 E., Greener, D. Whitmore; J. Appl. Phys., 32, (1961), 1320
- 158 R. Tredgold; 'Space Charge Conductivity in Solids', Elsevier, 1966
- 159 G. Roberts, N. Apsley, R. Munn; Physics Reports, 60, (1980), 59
- 160 A. Von Hippel, R. Breckenridge, F. Chelsea; L. Tisza, Ind. Eng. Chem. 38, (1946), 1097
- 161 H. Kokado, W. Scheider; J. Chem. Phys. 40, (1964), 2937
- 162 S. Agarwal, Phys. Rev. B 10, (1974), 4340
- 163 S. Agarwal, H. Fritzsche; Phys. Rev. B 10, (1974), 4351
- 164 K. Kao, W. Hwang; 'Electrical transport in solids', Pergamon, 1981, p 302
- 165 M. Driver, G. Wright; Proc. Phys. Soc., (London), 81, (1963), 141
- 166 K. Kirov, V. Zhelev; Phys. Stat. Sol., 8, (1965), 431

